

# Materials toward the Upscaling of Perovskite Solar Cells: Progress, Challenges, and Strategies

Fangfang Wang, Yezhou Cao, Cheng Chen, Qing Chen, Xiao Wu, Xinguo Li, Tianshi Qin,\* and Wei Huang\*

Perovskite solar cells (PSCs) are promising candidates for the next generation of photovoltaic technologies due to their constantly improved efficiencies, which gain much attention from both the scientific and industrial communities. Although the performance of PSCs is dramatically enhanced, most certified or reported high-efficiency PSCs are still limited to a relatively small active area. The degradation of efficiency and stability accompanied by upscaling must be solved, being a bottleneck toward industrialization. This review focuses on the research progress, challenges, and strategies on large-area PSCs, especially each functional material in various device architectures, including perovskites, hole transport materials, electron transport materials, and electrodes. Finally, the main issues related to each functional layer of PSCs from laboratory to industry are presented and an outlook on the research direction of large-area PSCs is given.

## 1. Background and Introduction

Organic–inorganic lead halide perovskite solar cells (PSCs) have attracted much attention due to the remarkable progress of their power conversion efficiencies (PCEs) over the past few years.<sup>[1–9]</sup> A record-certified PCE of 23.3% has been achieved in 2018, which is close to the efficiency value of commercial solar cells based on monocrystalline silicon films.<sup>[10]</sup> The superior performance of PSCs is due to the outstanding optoelectronic properties of hybrid perovskite materials, which possesses advantages of both organic and inorganic semiconductor

materials including high absorption coefficient,<sup>[11,12]</sup> high mobility,<sup>[13–16]</sup> long balanced carrier diffusion length,<sup>[15–18]</sup> and small exciton binding energy.<sup>[19]</sup> The lead halide perovskites usually have a cubic structure with formula  $ABX_3$ , where A is a monovalent cation (typically methylammonium (MA,  $CH_3NH_3^+$ ), formamidinium (FA,  $CH_3(NH_2)_2^+$ ),  $K^+$ ,  $Rb^+$ , and  $Cs^+$ ), B is a divalent metallic cation (typically  $Pb^{2+}$ ,  $Sn^{2+}$ , and  $Ge^{2+}$ ), and X is a halogen (typically  $I^-$ ,  $Br^-$ , and  $Cl^-$ ). In such perovskite structure, the corner sharing  $[BX_6]$  octahedra form a 3D inorganic framework, and the A-cation fills the interstitial space created by the eight adjacent octahedra in the structure (Figure 1). In 2009, Kojima


et al. first used the  $MAPbI_3$  perovskite as a sensitizer in liquid dye-sensitized solar cells (DSCs), which exhibited a 3.8% PCE.<sup>[1]</sup> In 2011, Park and co-workers modified the electrolyte solvent from acetonitrile to ethyl acetate and obtained a DSC with a 6.5% efficiency.<sup>[20]</sup> However, the devices possessed a poor stability due to the dissolution of the perovskite in the liquid electrolytes. In 2012, a major breakthrough in the PSC field was achieved by replacing liquid electrolytes with solid state hole transport materials (HTMs), which exhibited a 9.7% PCE.<sup>[21]</sup> Since then, the efficiency records of small-area PSCs have been constantly refreshed. The first certified PSC was reported by Burschka et al. in 2013 with the PCE of  $\approx 15\%$ .<sup>[22]</sup> From 2013 to 2018, the certified PCEs quickly increased to over 22%.<sup>[2–9,22–31]</sup> Although the device efficiency has developed rapidly, so far the certified or reported high-efficiency PSCs generally possess a relatively small active area (typically  $\approx 0.1\text{ cm}^2$ , sometimes even as small as  $0.03\text{ cm}^2$ ). As shown in Figure 2, the efficiency of small-area PSCs (less than  $1\text{ cm}^2$ ) has steadily achieved more than 20% since 2015, and recently realized to a high record of 23.3%. The PSCs with  $1\text{ cm}^2$  active area only achieve  $\approx 20\%$  in the past 2 years. The PCEs of large-area PSCs and perovskite solar modules (PSMs) are still less than 16%, and the device efficiencies show a downward trend with the enlargement of active area. In addition to pursuing an even higher PCE, enormous research efforts are also urgently focused on scaling up PSCs to promote the “lab-to-fab” translation of the perovskite photovoltaic technology.<sup>[32]</sup>

To achieve commercial applications of PSCs, we still need to face two major challenges. The first one is that the efficiency of PSCs decreases along with the enlargement of the device area (Figure 2).<sup>[33,34]</sup> This is because the film of each functional layer

Dr. F. Wang, Y. Cao, C. Chen, Q. Chen, Prof. T. Qin, Prof. W. Huang  
Key Laboratory of Flexible Electronics (KLOFE) and Institute  
of Advanced Materials (IAM)  
Jiangsu National Synergistic Innovation Center  
for Advanced Materials (SICAM)  
Nanjing Tech University (NanjingTech)  
30 South Puzhu Road, Nanjing 211816, P. R. China  
E-mail: iamtsqin@njtech.edu.cn; iamwhuang@njtech.edu.cn,  
iamwhuang@nwpu.edu.cn

Dr. X. Wu, X. Li  
BOE Technology Group Co., Ltd.  
9 Dize Road, Beijing 100176, P. R. China

Prof. W. Huang  
Shaanxi Institute of Flexible Electronics (SIFE)  
Northwestern Polytechnical University (NPU)  
127 West Youyi Road, Xi'an 710072, Shaanxi, China

 The ORCID identification number(s) for the author(s) of this article can be found under <https://doi.org/10.1002/adfm.201803753>.

DOI: 10.1002/adfm.201803753

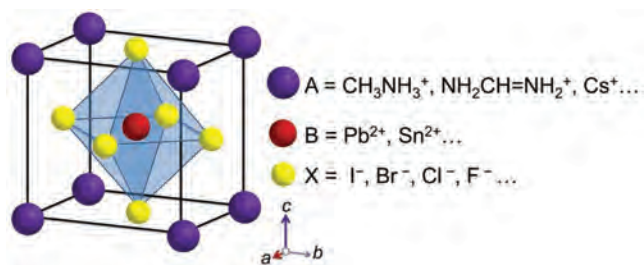


**Figure 1.** Structural features of metal halide perovskite materials.

is not perfect in terms of coverage, uniformity, and flatness due to the use of solution processing method. Even for high efficient PSCs with a small area, the PCE still shows a wide range of distribution.<sup>[5,6,24,29,31]</sup> After the size of the device is enlarged, the defects of the functional layers will have a greater impact on the extraction and transport of photoinduced carriers, leading to a significant decrease in device performance.<sup>[33,34]</sup> Moreover, the credibility of testing results for small-area devices have been questioned because measurement errors increase along with decreasing the active area. The second challenge is the stability issue accompanied by scaling-up.<sup>[35,36]</sup> Stability has been identified as one of the significant problems in PSCs. The external factors affecting stability are mainly temperature and illumination, as well as ambient (moisture, oxygen) exposure. The device degradation can occur by the deterioration of the active layer, charge transport layer, or electrode. Furthermore, the film quality of each functional layer also affects the device stability, which is related to the intrinsic properties of the materials. Besides two challenges mentioned above, cost is also an important factor affecting the commercialization of PSCs. Since the main components of the PSC device can be fabricated with low-cost coating processes using inexpensive and abundant materials, PSCs are often considered to have the potential to achieve low-cost production compared to the conventional photovoltaic technology that need high energy and vacuum to prepare solar cells. However, the champion small-area PSCs with high efficiency of more than 20% usually require relatively expensive materials such as Spiro-OMeTAD (2,2',7,7'-tetrakis[*N,N*-bis(4-methoxyphenyl)amino]-9,9'-spirobifluorene) and Au, and even a vacuum deposition technology. The tradeoff between low cost and high performance of PSCs is an important issue that must be considered in device amplification.

Herein, we review the progresses and issues on large-area perovskite solar cells in terms of each functional layers, such as perovskites, hole transport materials, electron transport materials (ETMs), and electrodes, with the hope of promoting design and optimization of materials toward the upscaling of perovskite solar cells.

## 2. Device Architecture

The architecture of PSCs is multilayered which typically comprise five layers: transparent electrode, electron transport layer (ETL), perovskite layer, hole transport layer (HTL) and metal electrode. Each functional layer plays a significant role in the photovoltaic process. Perovskites act as the active layer



**Fangfang Wang** is an associate professor in the Institute of Advanced Materials of Nanjing Tech University. She received her Ph.D. degree in State Key Laboratory of Supramolecular Structure and Materials from Jilin University in 2009. She pursued her postdoctoral research in Changchun Institute of Applied Chemistry, Chinese

Academy of Sciences. She currently focuses on the research of scalable perovskite solar cells, especially in design and synthesis of low-cost and productive materials for high performance, long lifetime, and large-size perovskite solar cells.



**Tianshi Qin** received his B.Sc. degree from Nanjing University in China, M.Sc. degree from Martin Luther University, and Ph.D. degree from Johannes Gutenberg University in Germany, respectively. From 2006 to 2011, he worked at Max-Planck-Institute for Polymer Research in Mainz. From 2011 to 2016, he worked

at Commonwealth Scientific and Industrial Research Organisation (CSIRO) in Melbourne. He joined Nanjing Tech University in 2017 as a professor. He mainly focuses on the structures and formulae of foremost materials and so far has achieved cutting-edge results in large-area roll-to-roll printed flexible solar cells.



**Wei Huang** received his Ph.D. degree from Peking University. In 1993, he began his postdoctoral research in National University of Singapore. In 2001, he was appointed as a chair professor with Fudan University, where he founded and chaired the Institute of Advanced Materials (IAM). In 2006, he was appointed

vice president of Nanjing University of Posts and Telecommunications. In 2012, he was the president of Nanjing Tech University. Now, he is the vice president of the Northwestern Polytechnical University. He was elected as Academician of Chinese Academy of Sciences in 2011. His research interests include flexible electronic materials and devices, nanomaterials, nanotechnology, etc.

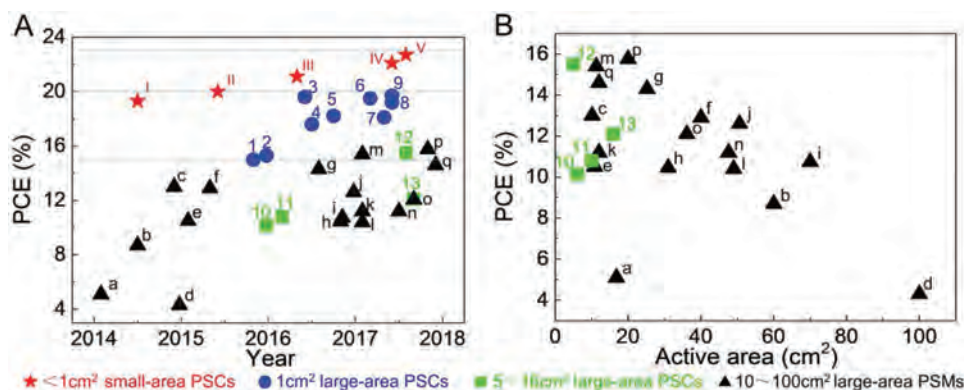


**Figure 2.** A) Efficiency map of PSCs and PSMs over the years. B) Efficiency distribution of large-area PSCs and PSMs related to active area. References: I,<sup>[287]</sup> II,<sup>[6]</sup> III,<sup>[5]</sup> IV,<sup>[30]</sup> V,<sup>[10]</sup> 1,<sup>[51]</sup> 2,<sup>[52]</sup> 3,<sup>[102]</sup> 4,<sup>[58]</sup> 5,<sup>[103]</sup> 6,<sup>[110]</sup> 7,<sup>[54]</sup> 8,<sup>[55]</sup> 9,<sup>[30]</sup> 10,<sup>[87]</sup> 11,<sup>[66]</sup> 12,<sup>[69]</sup> 13,<sup>[108]</sup> a,<sup>[80]</sup> b,<sup>[33]</sup> c,<sup>[61]</sup> d,<sup>[65]</sup> e,<sup>[81]</sup> f,<sup>[34]</sup> g,<sup>[90]</sup> h,<sup>[126]</sup> i,<sup>[126]</sup> j,<sup>[70]</sup> k,<sup>[72]</sup> l,<sup>[127]</sup> m,<sup>[39]</sup> n,<sup>[128]</sup> o,<sup>[59]</sup> p,<sup>[115]</sup> and q.<sup>[114]</sup>

that absorbs sunlight and generates free charges. To prevent charge recombination, the ETL (or HTL) extracts electrons (or holes) from perovskites, followed by transporting them to the cathode (or anode). Moreover, these two intermediate layers should be matched with the perovskite layer to compensate for the energy mismatch between the active layer and electrodes (Figure 3).

### 2.1. Traditional n-i-p Structure

PSCs with the traditional n-i-p-type usually adopt two different architectures. One is mesoporous n-i-p structure (Figure 4A), and the other is planar n-i-p structure (Figure 4B). A typical mesoporous n-i-p architecture consists of a fluorinated tin oxide (FTO) as a transparent substrate, then a very thin and compact titanium oxide (c-TiO<sub>2</sub>, ≈20–50 nm) as a hole blocking layer, a mesoporous TiO<sub>2</sub> or aluminum oxide (m-TiO<sub>2</sub> or m-AlO<sub>3</sub>, typically 100–300 nm) layer filled with perovskite material, followed by an organic or inorganic HTL (≈100–300 nm), and finally a metal anode (typically Au or Ag, ≈50–100 nm). The first mesoporous solid-state PSCs was reported by Grätzel and co-workers in 2012 and exhibited a PCE of 9.7%.<sup>[21]</sup> The device features perovskite MAPbI<sub>3</sub> nanocrystals as the photoabsorber, m-TiO<sub>2</sub> layer as a mesoporous

scaffold, and 2,2',7,7'-tetrakis-(N,N-di-4-methoxyphenylamino)-9,9'-spirobifluorene (Spiro-OMeTAD) as the HTL. After continuous development, the mesoporous n-i-p PSCs have achieved a PCE as high as 22.1%.<sup>[30]</sup> In 2012, Snaith and co-workers first confirmed the feasibility of the planar device configuration in PSCs.<sup>[37]</sup> With the rapid progress on planar PSCs, the PCE of 20.8% has been reached.<sup>[26]</sup>

### 2.2. Inverted p-i-n Structure

An inverted p-i-n perovskite solar cell (Figure 4C) has the opposite arrangement in device structure compared to traditional n-i-p structures. First, the HTL deposited on the surface of FTO or indium tin oxide (ITO) substrate. Then, the perovskite materials are deposited onto the HTL, followed by an ETL, such as fullerene derivatives [6,6]-phenyl-C<sub>61</sub>-butyric acid methyl ester (PC<sub>61</sub>BM). Finally, the device is completed by depositing a back electrode, such as Al, Cu, Ag or Au. In 2013, Jeng et al. first reported p-i-n PSCs with a device structure of glass/ITO/poly(3,4-ethylenedioxythiophene)-poly(styrenesulfonate) (PEDOT:PSS)/MAPbI<sub>3</sub>/C<sub>60</sub>/bathocuproine (BCP)/Al, which exhibited a PCE of 3.9%.<sup>[38]</sup> The efficiency of inverted PSCs has been remarkably improved by various approaches and to date achieved more than 20%.<sup>[39]</sup>

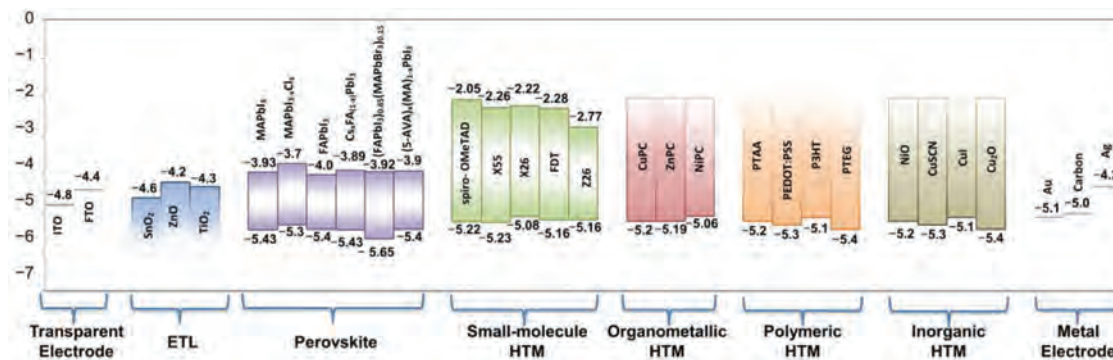


**Figure 3.** Schematic energy-level diagram of the functional layers used in PSCs including transparent electrode, electron transport layer, perovskite layer, hole transport layer and metal electrode.



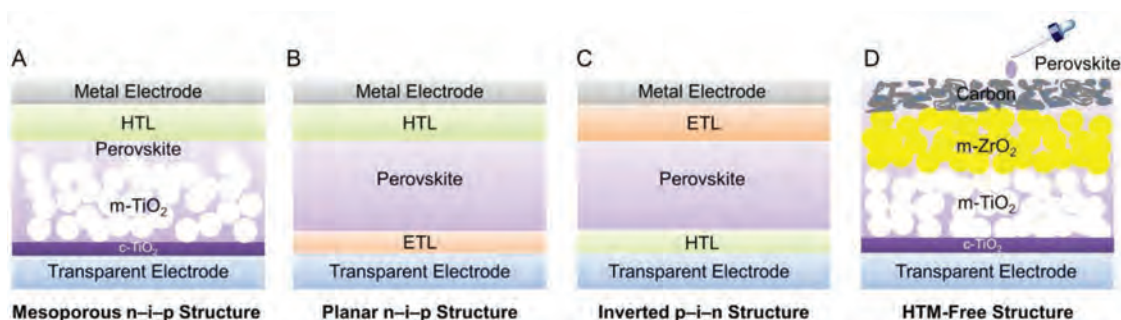


**Figure 4.** Common device structures of perovskite solar cells.

### 2.3. Hole-Transport-Material-Free Structures

The first efficient HTM-free PSC was reported by Han and co-workers in 2013, as shown in Figure 4D.<sup>[40]</sup> A dense  $c\text{-TiO}_2$  layer was firstly coated on a FTO. Then, a screen-printed  $m\text{-TiO}_2$  layer was employed as the electron transport layer. Subsequently, an insulating  $\text{ZrO}_2$  space layer was printed on the top of the  $m\text{-TiO}_2$  layer to prevent short circuit. After that, carbon black composite slurry was printed on the top of  $\text{ZrO}_2$  and subsequently annealed at high temperature to form a carbon black electrode. Finally, perovskite precursor solution was infiltrated into the mesoporous structure and an HTM-free PSC with a PCE of 6.64% was obtained. In 2014, by using the same device structure, a certified PCE of 12.8% was reported by Han and co-workers.<sup>[41]</sup> Moreover, the PSCs showed high stability for more than 1000 h under AM1.5G sunlight illumination in ambient air. In 2018, the efficiency of HTM-free PSCs was improved to 15.6% by the same group.<sup>[42]</sup> To date, many researches have focused on this device architecture owing to the high stability of the carbon electrode.<sup>[43,44]</sup>

### 2.4. Perovskite Solar Module

Module fabrication is a necessary step during the development of photovoltaic technology from the laboratory to industrialization. PSMs can be constructed by connecting subcells in series or parallel. The usual method for fabricating PSMs is series

connection from subcells, which can enhance the photovoltage of the modules but keep a minimum photocurrent among these subcells. A small photocurrent can reduce the effect of increased series resistance mainly from large-area transparent electrode.<sup>[45]</sup> The p-i-n and n-i-p-type PSMs in series connection are depicted in Figure 5A,B, respectively. Figure 5C shows a photograph of the PSMs. It is noted that efficient module fabrication appears to be more dependent on the quality of the device layers than small solar cells. In addition, scaling-up of the device has brought about a relatively low efficiency of the module compared to small size PSCs, which can be clearly seen in Figure 2.

## 3. Perovskite Materials

Perovskite layer as the active layer plays an important role in the device performance, which is significantly affected by the film morphology and crystalline quality.<sup>[38]</sup> Recently, numerous researches have focused on enlarging grain size and improving crystalline quality of perovskite films, which can reduce recombination loss due to decreasing the defect density and achieving rapid charge transport. However, it is still a challenge to control the film morphology and crystalline quality during the perovskite film formation over a large device area. In this section, we summarize the development and evolution of large-area PSCs using different perovskite materials.

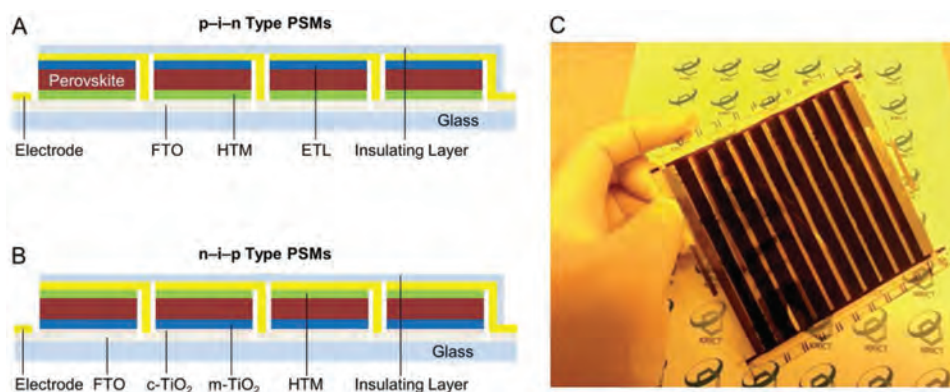


**Figure 5.** Structure diagrams of A) p-i-n-type and B) n-i-p-type modules. C) Photograph of the perovskite solar module (10 cm × 10 cm). C) Reproduced with permission.<sup>[33]</sup> Copyright 2014, Royal Society of Chemistry.

### 3.1. Methylammonium Lead Triiodide ( $\text{ABX}_3 = \text{MAPbI}_3$ )

$\text{MAPbI}_3$  has been the most commonly used and investigated material for large-scale perovskite films owing to the easy preparation and simple components. This perovskite exhibits excellent optoelectronic properties, such as wide absorption spectrum up to 800 nm, high absorption coefficient of  $1.5 \times 10^4 \text{ cm}^{-1}$  at 550 nm,<sup>[1]</sup> high carrier mobility ( $\approx 67 \text{ cm}^2 \text{ V}^{-1} \text{ s}^{-1}$ ),<sup>[46]</sup> low exciton binding energy ( $< 10 \text{ meV}$ ),<sup>[47]</sup> and long electron- and hole-diffusion length (up to 1  $\mu\text{m}$ ).<sup>[15]</sup> To realize the purpose of fabricating large-area  $\text{MAPbI}_3$ -based PSCs, several processing techniques are utilized and developed. Deposition technology can be divided into one-step and two-step methods according to the preparation steps discussed below. The summarized data are listed in **Table 1**.

#### 3.1.1. One-Step Method

For the one-step spin-coating method (**Figure 6A**), both  $\text{PbI}_2$  and  $\text{CH}_3\text{NH}_3\text{I}$  are usually dissolved in a polar solvent (dimethylformamide (DMF),  $\gamma$ -butyrolactone (GBL), or dimethyl sulfoxide (DMSO)) to form the perovskite precursors.<sup>[48]</sup> In the spin-coating process, solvent evaporation induces the crystal perovskite formation onto the substrate. The rate of solvent evaporation and reaction of  $\text{PbI}_2$  with  $\text{CH}_3\text{NH}_3\text{I}$  needs to be carefully controlled to benefit the perovskite crystal growth and prevent pinhole defect formation of the final perovskite film.<sup>[22,49]</sup> In June 2014, Seo and co-workers for the first time demonstrated a solution-processing method for the fabrication of a 10 cm  $\times$  10 cm (active area of 60  $\text{cm}^2$ ) p–i–n PSM (**Figure 5C**), which exhibited a PCE of 8.7%.<sup>[33]</sup> Solvent engineering was employed to create a highly uniform perovskite film with a root-mean-square (RMS) roughness of 10 nm. Generally, perovskite crystalline can easily be formed by a direct reaction between MAI and  $\text{PbI}_2$  dissolved in a polar aprotic solvent. In this solvent-engineering process, a mixed solvent of DMSO and GBL is used and the presence of DMSO in GBL retards the rapid reaction of  $\text{PbI}_2$  with  $\text{CH}_3\text{NH}_3\text{I}$  by forming DMSO– $\text{PbI}_2$  complexes.<sup>[24,50]</sup> This allows a smoother film to be formed upon a consecutive spin-coating process. Also by using spin-coating process, a 10 cm  $\times$  10 cm (active area of 40  $\text{cm}^2$ ) inverted PSM was fabricated by Heo et al. and the PCE was improved to 12.9%.<sup>[34]</sup> In 2015, Chen et al. reported a breakthrough work, in which  $> 1 \text{ cm}^2$  size solution-processed PSCs with a certified PCE of 15% was achieved.<sup>[51]</sup> Heavily doped inorganic materials were employed as the charge extraction layers of the p–i–n-type device, which avoided pinholes and reduced local structural defects in large-area films. The device showed a good stability, retaining  $> 90\%$  of the initial PCE after aging 1000 h of light soaking. At the end of the same year, Yang et al. reported a 1  $\text{cm}^2$  area n–i–p-type PSC with a PCE of 15.3%, which was fabricated by solvent bathing route.<sup>[52]</sup> They found that the excessive MAI played a critical role during the subsequent air annealing to facilitate significant grain growth, development of strong 110 textures, and mitigation of  $\text{MAPbI}_3$  decomposition. In 2016, Leyden et al. fabricated modules using spin-coating process and demonstrated a PCE of 14.6% for 1  $\text{cm}^2$  single cells and 8.5% for 5 cm  $\times$  5 cm modules.<sup>[53]</sup>

In 2017, Lee et al. fabricated low-temperature processing, hysteresis-free, and stable PSCs with 1  $\text{cm}^2$  active area by using a versatile organic nanocomposite that combines an electron acceptor and a surface modifier.<sup>[54]</sup> The PCE of this large-area PSC was over 18% and the PCE of PSC with the printed ETL was over 17%. By using an ionic-liquid additive of methylammonium acetate (MAAc) and a molecular additive of thiosemicarbazide (TSC), Wu et al. reported a 1.025  $\text{cm}^2$  aperture-area PSC with a certified PCE of 19.19%, and the high-performing devices can retain over 80% of its initial PCE after 500 h under thermal stress of 85  $^\circ\text{C}$ .<sup>[55]</sup> The high performance of devices was attributed to the large crystals with high crystalline quality by using the additive engineering strategy.

Besides spin-coating processing, other state-of-the-art deposition techniques are also used to give high-quality crystalline perovskite films. Blade coating, also named doctor blading or knife coating, is usually used to fabricate large-area films on rigid or flexible substrates. Deng et al. fabricated 1-inch<sup>2</sup>-area perovskite films by using the modified doctor-blading method (**Figure 6B**).<sup>[56]</sup> They found that the larger crystalline grains were obtained from doctor blading compared to spin coating, which yielded a PSM with an exciting efficiency of 15.1%. Very recently, in the research of Deng et al., they used the perovskite ink solution combined with surfactant additive for blade-coating process and found that surfactant additive could alter the solution flow dynamics and enhance the adhesion of the perovskite solution to very hydrophobic hole transport materials.<sup>[57]</sup> The additives enable the bladed perovskite films to be uniformly coated over large areas and passivate the charge traps. Fast blading of perovskite films in air results in stabilized module efficiencies of 15.3% and 14.6% measured at aperture areas of 33.0 and 57.2  $\text{cm}^2$ , respectively. The method of adding surfactants to perovskite inks could be a general strategy for improving perovskite film quality in various scalable fabrication.

Novel solution processing methods were also developed to prepare high-quality perovskite films. Ye et al. reported a soft-cover deposition (SCD) method, in which they used a soft cover with high surface wettability to spread perovskite precursor solution on a large-area preheated substrate.<sup>[58]</sup> The perovskite precursor solution was thermally stable at the boiling point because of the additional function of the soft cover blocking the solvent evaporation into air. As a result, a pinhole-free, large-grain-size, and rough-border-free perovskite film with a large-area smooth surface of 51  $\text{cm}^2$  was present, which showed a material utilization ratio of 80%. The 1  $\text{cm}^2$  working-area PSCs with very small hysteresis and high reproducibility were obtained, which exhibited a PCE of up to 17.6%. The major steps of SCD are illustrated in **Figure 6C**. Chen and co-workers reported a new deposition method of perovskite films, which was irrelevant to the use of a common solvent or vacuum.<sup>[59]</sup> The certified efficiency of the PSM with an aperture area of 36.1  $\text{cm}^2$  was 12.1% (**Figure 6Dc**), which was the first record produced by perovskite solar modules in the solar cell efficiency tables (version 49).<sup>[60]</sup> The major processing method is shown in **Figure 6Da**. Scanning electron microscopy (SEM) shown that the pressure-processed perovskite films were pinhole-free and highly uniform. The grain size of the perovskite film deposited by this procedure was 3–4 times larger than that of

**Table 1.** Representative reports of large-area PSCs or PSMs using MAPbI<sub>3</sub> as the active layer.

Perovskite	Module area [cm <sup>2</sup> ] <sup>a)</sup>	Active area [cm <sup>2</sup> ]	Aperture area [cm <sup>2</sup> ]	V <sub>oc</sub> [V]	J <sub>sc</sub> [mA cm <sup>-2</sup> ]	I <sub>sc</sub> [mA]	FF [%]	PCE [%] <sup>b)</sup>	Device structure	Type <sup>c)</sup>	Processing method/steps	Ref.
MAPbI <sub>3</sub>	100 (10 × 10)	60 (10 cell)	–	0.866	20.7	–	78.3	8.7	ITO/PEDOT:PSS/perovskite/PCBM/LiF/Al	I	Spin coating/1	[33]
MAPbI <sub>3</sub>	100 (10 × 10)	40 (10 cell)	–	10.1	–	80.1	63.7	12.9	ITO/PEDOT:PSS/perovskite/PCBM/Au	I	Spin coating/1	[34]
MAPbI <sub>3</sub>	–	1.02	–	1.09	17.35	–	66.8	15/AIST	FTO/NiMgLiO/perovskite/PCBM/Ti(Nb)O <sub>x</sub> /Ag	I	Spin coating/1	[51]
MAPbI <sub>3</sub>	–	1.2	–	1.09	21.3	–	66.1	15.3	FTO/c-TiO <sub>2</sub> /perovskite/Spiro-OMeTAD/Ag	P	Solvent-bathing/1	[52]
MAPbI <sub>3</sub>	–	1	–	1.12	20.5	–	68.0	14.6	FTO/c-TiO <sub>2</sub> /m-TiO <sub>2</sub> /perovskite/Spiro-OMeTAD/Au	M	Spin coating/1	[53]
MAPbI <sub>3</sub>	25 (5 × 5)	15.4 (6 cell)	–	0.98	19	–	46.0	8.5				
MAPbI <sub>3</sub>	–	1	–	1.10	20.73	–	79.0	18.1	ITO/PEI:PCBM/perovskite/PTAA/MoO <sub>3</sub> /Ag	I	Spin coating/1	[54]
MAPbI <sub>3</sub>	–	1.025	–	1.12	23.17	–	75.7	19.2/AIST	FTO/NiO/perovskite/PC <sub>61</sub> BM/BCP/Ag	I	Spin coating/1	[55]
MAPbI <sub>3</sub>	1 in. × 1 in.	–	–	1.05	21.8	–	66.0	15.1	ITO/c-OTPD:TPACA/perovskite/PCBM/C <sub>60</sub> /BCP/Al	I	Blade coating/1	[56]
MAPbI <sub>3</sub>	√	–	33.0	1.07	19.5	–	72.1	15.0	ITO/PTAA/perovskite/C <sub>60</sub> /BCP/Cu	I	Blade coating/1	[57]
MAPbI <sub>3</sub>	110.5 (13.0 × 8.5)	–	57.8	17.24	–	72.5	68.9	14.9	ITO/PTAA/perovskite/C <sub>60</sub> /BCP/Cu	I	Blade coating/1	
MAPbI <sub>3</sub>	–	1	–	1.02	21.8	–	78.7	17.6	FTO/NiO/perovskite/PCBM/Ag	I	Soft-cover deposition/1	[58]
MAPbI <sub>3</sub>	6 × 6	–	36.13 (10 cell)	8.36	–	73	71.5	12.1/AIST	FTO/c-TiO <sub>2</sub> /m-TiO <sub>2</sub> /perovskite/Spiro-OMeTAD/Au	M	Pressure processing /1	[59]
MAPbI <sub>3</sub>	√	10.1 (4 cell)	–	4.21	–	47	66.5	13	FTO/c-TiO <sub>2</sub> /m-TiO <sub>2</sub> /perovskite/Spiro-OMeTAD/Au	M	Sequential deposition/2	[61]
MAPbI <sub>3</sub>	–	1	–	0.99	19.63	–	50.0	9.72	FTO/c-TiO <sub>2</sub> /m-TiO <sub>3</sub> /perovskite/Carbon	M	Sequential deposition/2	[62]
MAPbI <sub>3</sub>	–	1.3	–	0.99	22.51	–	75.0	16.7	ITO/PEDOT:PSS/perovskite/PCBM/Ca/Al	I	Two step spin coating/2	[39]
MAPbI <sub>3</sub>	√	11.25	–	4.69	4.25	–	77.0	15.4				
MAPbI <sub>3</sub>	–	Roll to roll	–	0.96	19.35	–	63.0	11.6	ITO/ZnO/printed perovskite/doped-P3HT/Ag	I	Sequential Slot die/2	[63]
MAPbI <sub>3</sub>	–	Roll to roll	–	0.98	20.38	–	59.9	11.96	ITO/ZnO/Printed Perovskite/doped-P3HT/Ag	I	Sequential Slot die/2	[64]
MAPbI <sub>3</sub>	10 (2.5 × 4)	10.1 (4 cell)	–	4.11	17.17	43.27	58.14	10.26	FTO/c-TiO <sub>2</sub> /m-TiO <sub>2</sub> /perovskite/Spiro-OMeTAD/Au	M	Blade coating deposition/2	[65]
MAPbI <sub>3</sub>	100	100 (9 cell)	–	9.61	7.48	83.09	53.79	4.3	FTO/c-TiO <sub>2</sub> /m-TiO <sub>2</sub> /perovskite/P3HT/Au	M		

**Table 1.** Continued.

Perovskite	Module area [cm <sup>2</sup> ] <sup>a)</sup>	Active area [cm <sup>2</sup> ]	Aperture area [cm <sup>2</sup> ]	V <sub>oc</sub> [V]	J <sub>sc</sub> [mA cm <sup>-2</sup> ]	I <sub>sc</sub> [mA]	FF [%]	PCE [%] <sup>b)</sup>	Device structure	Type <sup>c)</sup>	Processing method/steps	Ref.
MAPbI <sub>3</sub>	–	2.5	–	0.92	19.4	–	72.3	12.9	FTO/PEDOT:PSS/perovskite/PCBM/Au	I	Close space sublimation deposition/2	[66]
MAPbI <sub>3</sub>	–	10	–	0.93	18.9	–	61.7	10.8				
MAPbI <sub>3</sub>	–	1	–	1.032	18.9	–	68.0	13.9	FTO/c-TiO <sub>2</sub> /perovskite/Spiro-OMeTAD/Au	M	Ultrasonic spray deposition/2	[68]
MAPbI <sub>3</sub>	–	–	5	1.03	21.5	–	70.1	15.5	SnO <sub>2</sub> :F(FTO)/NiO/perovskite/PCBM/BCP/Ag	P	Soft cover-deposition/2	[69]
MAPbI <sub>3</sub>	100 (10 × 10)	50.6 (8 cell)	–	8.57	–	114.8	64.6	12.6	FTO/c-TiO <sub>2</sub> /m-TiO <sub>2</sub> +graphene/GO-Li/perovskite/Spiro-OMeTAD/Au	M	Sequential deposition/2	[70]

<sup>a)</sup>√ = not given specific area value; <sup>b)</sup>PCEs are certified by National Institute of Advanced Industrial Science and Technology (AIST); <sup>c)</sup>M = mesoporous n–i–p configuration, P = planar n–i–p configuration, and I = inverted p–i–n configuration.

spin coating–processed film (Figure 6Db). The larger grain size indicated that the pressure process was helpful to the growth of perovskite crystals, which could reduce trap states and enhance the photovoltaic performance. Importantly, the new processing method can be carried out in air at low temperatures, which is advantageous to fabricating large-area perovskite devices.

### 3.1.2. Two-Step Method

The most commonly used two step method is the sequential deposition process developed by Grätzel and co-workers.<sup>[22]</sup> A mesoporous TiO<sub>2</sub> film is firstly spin-coated by PbI<sub>2</sub> solution and subsequently immersed into a CH<sub>3</sub>NH<sub>3</sub>I solution to form

a perovskite crystal (Figure 6Ab). This method is applicable to PSCs using a mesoporous metal-oxide film rather than the planar ones without the scaffold structure. In the latter, MAI molecules could be much difficult to penetrate into the dense PbI<sub>2</sub> film, resulting in the incomplete reaction of PbI<sub>2</sub>.<sup>[49]</sup> By using two-step deposition of MAPbI<sub>3</sub>, Matteocci et al. reported a 10.08 cm<sup>2</sup> active-area PSM with a maximum PCE of 13.0% under AM1.5G illumination conditions.<sup>[61]</sup> In another work, two-step sequential method was exploited to prepare a high-quality perovskite layer for the paintable carbon-based PSCs, in which the solvent of MAI solution used at the second step was changed from isopropanol (IPA) to a mixed solvent of IPA/cyclohexane.<sup>[62]</sup> This mixed solvent not only accelerated the conversion of PbI<sub>2</sub> to CH<sub>3</sub>NH<sub>3</sub>PbI<sub>3</sub> but also suppressed the Ost-

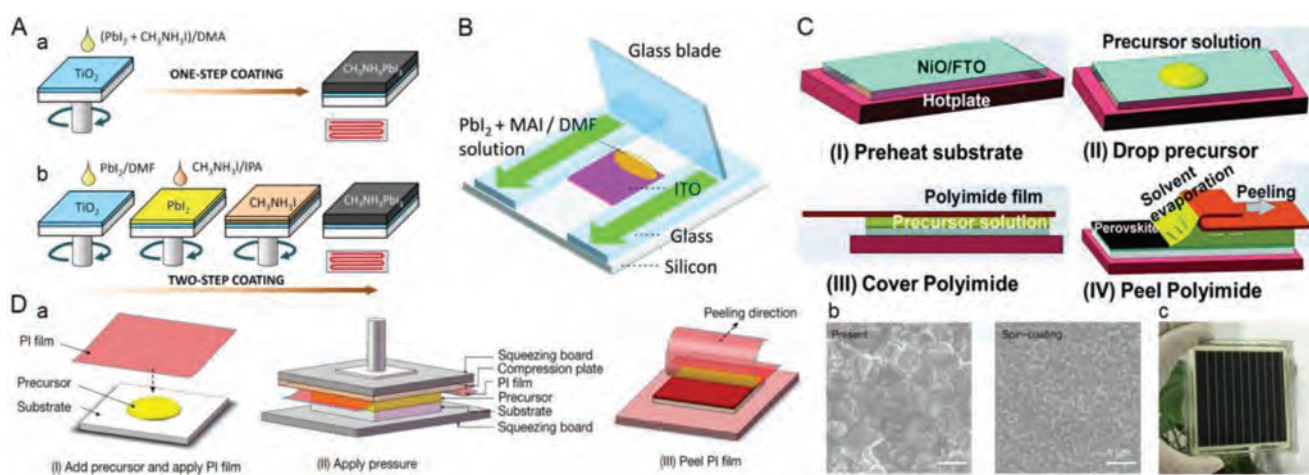


**Figure 6.** A) One-step a) and two-step b) spin-coating procedures for MAPbI<sub>3</sub> formation. Reproduced with permission.<sup>[48]</sup> Copyright 2014, American Institute of Physics. B) Illustration of the experimental setup for perovskite film deposition via doctor blading. Reproduced with permission.<sup>[56]</sup> Copyright 2015, Royal Society of Chemistry. C) Illustration of soft-cover deposition method. Reproduced with permission.<sup>[58]</sup> Copyright 2016, Royal Society of Chemistry. D) Diagram of the pressure processing method for the deposition of perovskite film a). Processing method: (I) add amine complex precursors and cover with polyimide (PI) film; (II) apply pressure; (III) heat and peel off the PI film. b) SEM images, and c) photograph of the module with an aperture area of 36.1 cm<sup>2</sup>. Reproduced with permission.<sup>[59]</sup> Copyright 2017, Nature Publishing Group.



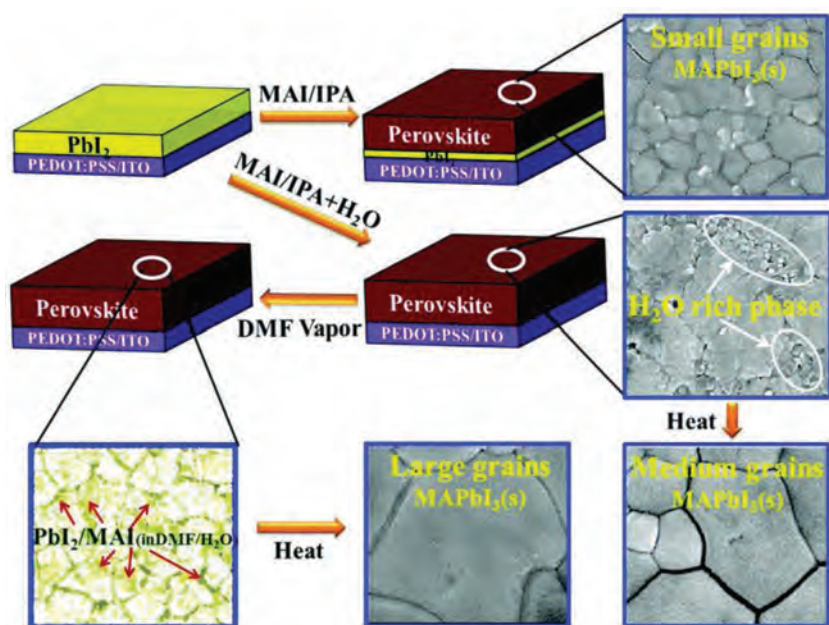


**Figure 7.** Schematic illustration of the synergistic effect for preparing the high-quality thick MAPbI<sub>3</sub> film using a H<sub>2</sub>O additive in MAI/IPA and DMF vapor post treatment. Reproduced with permission.<sup>[39]</sup> Copyright 2017, Royal Society of Chemistry.

wald ripening process, resulting in a high-quality perovskite layer, e.g., pure phase, even surface, and compact capping layer. A PCE of 10% was achieved for 1 cm<sup>2</sup> area device, which was a record for carbon-based HTM-free PSCs at the time of publication. For improving the morphology of the perovskite film, Chiang et al. used H<sub>2</sub>O as an additive in PbI<sub>2</sub>/DMF precursor solution and prepared a full coverage, good quality, and thick MAPbI<sub>3</sub> film via a two-step spin-coating method.<sup>[39]</sup> They found that H<sub>2</sub>O could not only help MAI to penetrate into the thick PbI<sub>2</sub> to form a pure MAPbI<sub>3</sub> film but also produce larger grains by slowing down the perovskite crystallization rate. Moreover, H<sub>2</sub>O could also cooperate with DMF to control the dissolution of perovskite grains during DMF vapor post treatment (Figure 7). The minimodule with an active area of 11.25 cm<sup>2</sup> realized a PCE of over 15%.

Among the solution-processing methods for the large-scale production of PSCs, slot-die coating shows many advantages. With this process, film thickness can easily be controlled by tuning the solution feed. In addition, this process would cause no material loss, and all injected solutions can be transferred to the substrate. In late 2014, Vak et al. reported fully printed PSCs with a PCE of 11.6% via 3D printer-based slot-die compatible process (Figure 8A) and a 47.3 cm<sup>2</sup> area module with a PCE of 4.57%.<sup>[63]</sup> Shortly afterward, Vak and co-workers reported a fully printed PSCs via roll-to-roll compatible process, and the best PCE of 11.9% was obtained (Figure 8B).<sup>[64]</sup> The results of the two works verify the possibility of the low-cost and full-automatic production of solution-processed PSCs by this technology. In another work, Razza et al. reported a sequential step method to deposit perovskite layers.<sup>[65]</sup> PbI<sub>2</sub> was blade-coated on a substrate, followed by treatment with air flow to control the crystallization. Subsequently, the highly compact PbI<sub>2</sub> film was dipped into a methylammonium iodide solution

to obtain the final perovskite layer. The large-scale PSMs with module active areas of 10.1 and 100 cm<sup>2</sup> showed the PCEs of 10.4% and 4.3%, respectively.

Besides the traditional sequential deposition method, many investigative efforts have been invested into the design of more stable PSCs by implementing new two-step deposition techniques. Guo et al. employed a new deposition method, named close space sublimation (CSS), to grow a high-quality MAPbI<sub>3</sub> thin film in a low-vacuum and even nonvacuum oven.<sup>[66]</sup> With this approach, the PCEs of 12.9% and 10.8% were achieved for active areas of 2.5 and 10 cm<sup>2</sup>, respectively. In this method, PbI<sub>2</sub> was spin-coated on a modified FTO substrate, and CH<sub>3</sub>NH<sub>3</sub>I was also spin-coated on a cleaned glass substrate. The two substrates were put facing each other with a thin hollow aluminum foil gasket to form the close space, followed by transferring to an isothermal vacuum or nonvacuum oven, as shown in Figure 8C. Along with increase of the temperature, the MAI film will sublimate to generate uniform MAI vapor, which can react with the predeposited PbI<sub>2</sub> layer to

form MAPbI<sub>3</sub> perovskite on the FTO substrate. A similar preparation process was reported by Chen et al. over the same period (Figure 8D).<sup>[67]</sup> They prepared high-quality perovskite thin films with an area of 8 × 8 cm<sup>2</sup> and employed an in situ resistance measurement method to monitor the evolution of perovskite thin films. Huang et al. reported a two-step ultrasonic spray method to fabricate 1 cm<sup>2</sup> area PSCs with a PCE of 13.09%.<sup>[68]</sup> The deposition process is shown in Figure 8E. The perovskite films deposited by this method showed better crystallinity, lower nonradiative recombination rate, and more efficient interfacial charge extraction property. A scalable low-temperature soft-cover deposition (LT-SCD) method was applied by Ye et al. to fabricate 12 cm<sup>2</sup> area, smooth and compact perovskite films.<sup>[69]</sup> Due to eliminating thermal convection-induced defects in the perovskite films, a PCE of 15.5% was achieved on a solar cell with an aperture area of 5 cm<sup>2</sup>. By low-temperature processing, the flexible PSCs based on a polyethylene terephthalate substrate achieved a PCE of 15.3%. As shown in Figure 8F, Agresti et al. showed the concept of graphene interface engineering as a viable route to tuning the interface properties and obtained a 50.6 cm<sup>2</sup> active-area PSM with a high PCE of 12.6%.<sup>[70]</sup>

Based on the above discussion of the one-step and two-step methods, many efforts have been made toward scaling-up production of PSCs. However, there is still a long way to go to get a better process for large-area device performance. Spin coating is widely used in small-area PSCs to prepare thin and uniform films owing to its simplicity and programming process and usually achieves exciting device performance. However, in the process of fabricating the large-area PSCs, the film may be inhomogeneous due to two factors. One is difference in the linear velocity of the spin-coating method, and the other is the fast drying leaving no enough time for perovskite crystallization completely. Generally, tuning solvent components



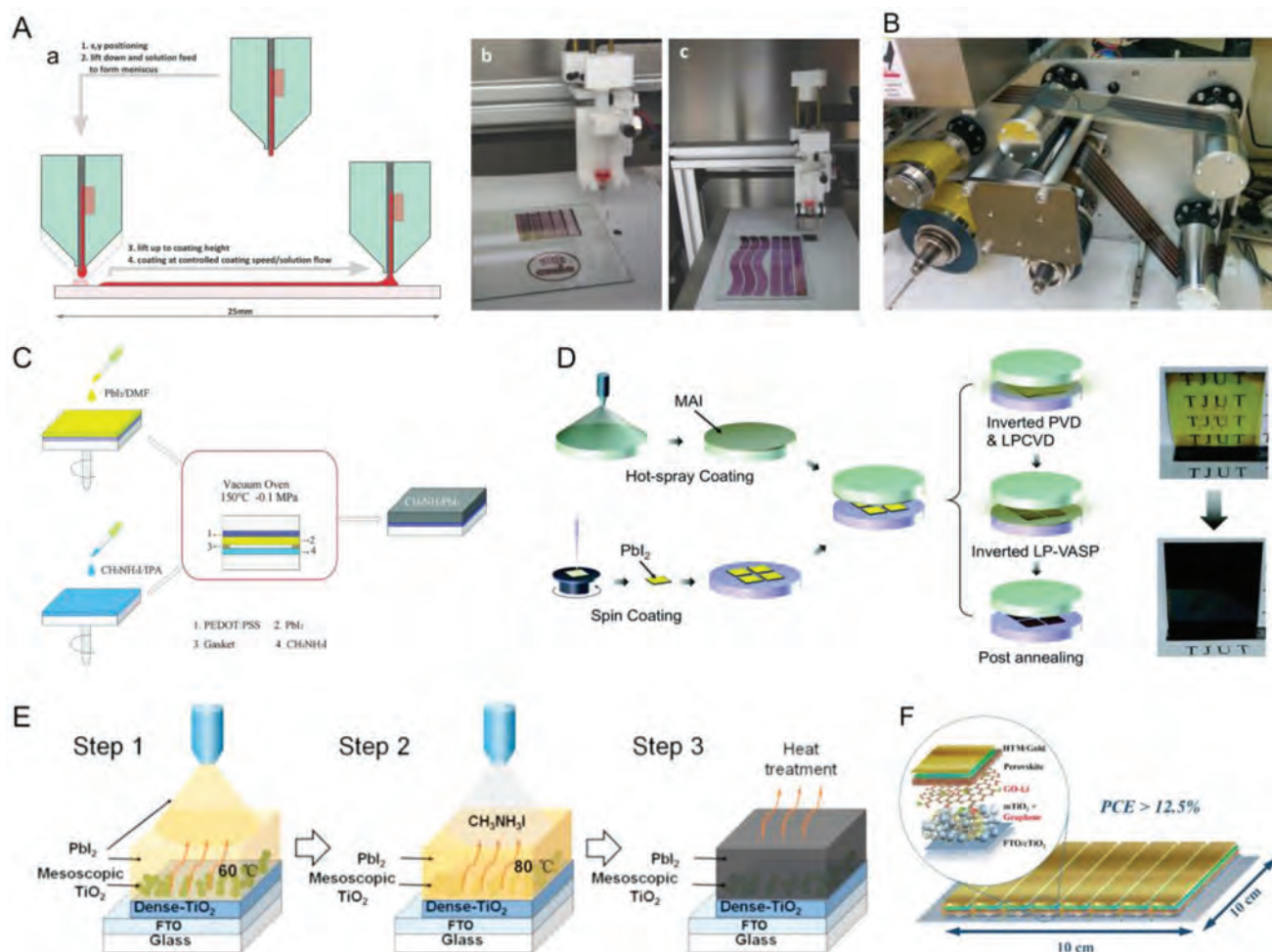


**Figure 8.** A) Schematic illustration of coating process of the 3D printer on a small size substrate a). Demonstration of capabilities of the modified 3D printer b) in printing mode with a point nozzle and c) in coating mode with a slot nozzle. A) Reproduced with permission.<sup>[63]</sup> Copyright 2015, Wiley-VCH. B) Roll-to-roll production of perovskite solar cells. Reproduced with permission.<sup>[64]</sup> Copyright 2015, Wiley-VCH. C) The procedures of perovskite thin film deposition using CSS deposition method. Reproduced with permission.<sup>[66]</sup> Copyright 2016, Royal Society of Chemistry. D) Schematic illustration of perovskite film formation, as well as photographs of the Pbl<sub>2</sub> and perovskite films (8 cm × 8 cm). Reproduced with permission.<sup>[67]</sup> Copyright 2016, Royal Society of Chemistry. E) Schematic diagram of the two-step spray method for the deposition of perovskite film. Reproduced with permission.<sup>[68]</sup> Copyright 2016, Elsevier. F) The structures of graphene interface engineering PSMs. Reproduced with permission.<sup>[70]</sup> Copyright 2017, American Chemical Society.

or using additives can optimize the quality of perovskite films, thus improving the photovoltaic performance. Nevertheless, the large-area PSCs by spin coating are still difficult to achieve the efficiency as high as the small-area devices. Moreover, the waste of materials in the spin-coating method is very serious, and the utilization rate is less than 10%, which is clearly disadvantage for the device enlargement. Blade coating and slot-die coating waste less ink than spin coating, and the process can be adapted for roll-to-roll manufacturing, which has a relatively high throughput compared to spin coating. These two techniques can be used to prepare larger size uniform film than spin coating, but the device performance is also relatively low. It is noted that the film quality is controlled by several factors, including the viscosity of the precursor ink and the coating speed. The device efficiency should be increased by optimizing the ink compositions and processing parameters. The new type preparation methods for perovskite film exhibit the potential to produce efficient large-area devices, such as soft-cover

deposition and pressure processing. However, the popularity of the new technology that relies on the preparation instruments still needs to take time.

### 3.2. Modification of X Position in ABX<sub>3</sub> Perovskite (X = I, Br, and Cl)

Anion substitution is an effective method to tune the optoelectronic properties of metal halide perovskites, such as the replacement of the iodine in MAPbI<sub>3</sub> with both chlorine and bromine. The bandgap of perovskites increases along with the decrease of the halide ionic size. Halide substitutions are typically I<sup>-</sup>,<sup>[18]</sup> Br<sup>-</sup>,<sup>[71]</sup> Cl<sup>-</sup>,<sup>[72]</sup> BF<sub>4</sub><sup>-</sup>,<sup>[73]</sup> and SCN<sup>-</sup>.<sup>[74]</sup> It was known that the halide in the MAPbX<sub>3</sub> perovskite is a vital parameter in determining the photoelectric properties and film morphology, as well as the photovoltaic performance of the perovskite. Theoretical calculation data<sup>[75]</sup> indicated that introducing Cl in MAPbI<sub>3</sub> will improve the film morphology<sup>[37]</sup> without changing

the absorption onset (800 nm) of the perovskite. MAPbI<sub>3-x</sub>Cl<sub>x</sub> has the long carrier lifetime and fast carrier transport compared to MAPbI<sub>3</sub> and also is more stable than MAPbCl<sub>3</sub>.<sup>[31,76,77]</sup> Study reveals that by introducing Br ion into the perovskite structure, ordered cubic phase MAPbI<sub>3-x</sub>Br<sub>x</sub> exhibits a good device stability in comparison with the distorted tetragonal phase MAPbI<sub>3</sub>.<sup>[78]</sup> Furthermore, solar cells based on MAPbI<sub>3-x</sub>Br<sub>x</sub> exhibit higher open-circuit voltages because MAPbBr<sub>3</sub> has a higher lowest unoccupied molecular orbital (LUMO) and a lower highest occupied molecular orbital (HOMO) energy level than MAPbI<sub>3</sub>.<sup>[79]</sup> The summarized data are listed in **Table 2**.

### 3.2.1. MAPbI<sub>3-x</sub>Cl<sub>x</sub>

In 2014, the first solid-state n-i-p PSM by using MAPbI<sub>3-x</sub>Cl<sub>x</sub> as absorber layer was reported exhibiting a PCE of ≈5.1% with an active area of 16.8 cm<sup>2</sup>.<sup>[80]</sup> The PCE was further improved to 8.2% by minimizing the contact resistance at the series interconnections via precise laser patterning by the same group.<sup>[61]</sup> Fakharuddin et al. fabricated MAPbI<sub>3-x</sub>Cl<sub>x</sub>-based solar modules (area: 10.8 cm<sup>2</sup>; PCE: 10.5%; av. 8.1%) employing vertically aligned TiO<sub>2</sub> nanorods as an ETL via precise laser patterning and interfacial engineering.<sup>[81]</sup> Qiu et al. reported a PSM by one-step spin-coating process with an aperture area of 4 cm<sup>2</sup>.<sup>[82]</sup> The PCE of 13.6% was achieved due to the pinhole-free and high-crystallinity perovskite films made with a precursor combination of Pb(CH<sub>3</sub>CO<sub>2</sub>)<sub>2</sub>·3H<sub>2</sub>O, PbCl<sub>2</sub>, and MAI. The results revealed that the PbCl<sub>2</sub> as one of the lead sources played an important role on impacting the crystal grain size and pinhole area of the perovskite film. The average grain size of the perovskite crystalline increased along with the PbCl<sub>2</sub> content in the mixture. Moreover, the optimal PbCl<sub>2</sub> content in the lead source composition was around 20–30%. The larger grains resulted in less grain boundaries, which could increase the performance of PSCs. Recently, considering the role of excess halide in the precursor in film formation and the state-of-the-art antisolvent-extraction approaches, Yang et al. demonstrated a general precursor formulation of Cl-containing methylammonium lead iodide along with solvent engineering, which could give a wide precursor-processing window and increase the growth rate of perovskite grains for the planar PSCs.<sup>[83]</sup> SEM images exhibited that excess MAI in the ink not only enhanced perovskite grain size and film crystallinity but also increased the perovskite grain growth rate, which significantly reduced the thermal annealing requirements. By using this ink, the blade-coating method showed almost the same film morphology and device performance as the spin coating (**Figure 9A**). The blade-coated devices with the active areas of 1.2 and 12.6 cm<sup>2</sup> yielded average efficiencies of 17.33% and 13.3%, respectively.

Flexible perovskite photovoltaic modules based on MAPbI<sub>3-x</sub>Cl<sub>x</sub> have also been investigated. Giacomo et al. fabricated flexible Perovskite PSMs (active area: 7.92 cm<sup>2</sup>) with an efficiency of 3.1%. **Figure 9B** shows the module fabrication procedures.<sup>[84]</sup> Yang et al. adopted the one-step processing method to simplify the blade-coating process, in which the precursor solution was composed of CH<sub>3</sub>NH<sub>3</sub>I and PbCl<sub>2</sub> in DMF.<sup>[85]</sup> A uniform 10 cm × 10 cm perovskite film was easily prepared by this process without wasting perovskite precursor compared

to spin-coating process. A flexible device with a PCE of 7.14% was also fabricated. Schmidt et al. reported around 50% loss in PSC performance when using a fully scalable fabrication process.<sup>[86]</sup> The PCE of devices based on the spin-coating method yields a PCE of 9.4%. The flexible devices based on ITO–polyethylene terephthalate (PET) substrates and printed back electrodes, as well as slot die-coated perovskite layers, exhibited a PCE of 4.9%. Back et al. reported a large-area (1.5 cm × 4.0 cm) MAPbI<sub>3-x</sub>Cl<sub>x</sub> perovskite film with excellent uniformity via blade coating and a printed solar cell with a PCE of 10.15%.<sup>[87]</sup> A 5 cm × 5 cm area device with a PCE of 11.2% was obtained by introducing bidentate halogenated additives into the MAPbI<sub>3-x</sub>Cl<sub>x</sub> precursor solution.<sup>[72]</sup> The temporary chelation between additives and Pb<sup>2+</sup> could affect the dynamic equilibrium during the heating and annealing processes of the spin-coated perovskite film, and slow down the crystallization of perovskite film, which contributed to a more uniform and nondefective growth of perovskite crystal nucleation.

### 3.2.2. MAPbI<sub>3-x</sub>Br<sub>x</sub>

Tait et al. demonstrated the generality of concurrently pumped ultrasonic spray coating for accurately and rapidly optimizing precursor ratios based on PbCl<sub>2</sub>, Pb(CH<sub>3</sub>CO<sub>2</sub>)<sub>2</sub>·3H<sub>2</sub>O, PbBr<sub>2</sub>, MABr, and MAI to achieve pinhole-free perovskite films with high crystallinity.<sup>[88]</sup> Initial PCE of 11.7% for 3.8 cm<sup>2</sup> area modules were achieved. The schematic of concurrently pumped ultrasonic spray coating for perovskite precursor deposition is shown in **Figure 10Aa**. Perovskite layers was spray-coated from DMF inks of PbCl<sub>2</sub>:MAI and PbAc<sub>2</sub>:MAI. Then, a full coverage and negligible-pinhole perovskite film was obtained, which could be confirmed by SEM image (**Figure 10Ab–d**). This concurrently pumped ultrasonic spray-coating technique offers a strategy to rapidly and precisely optimize PSCs.

### 3.2.3. MAPbI<sub>3-x-y</sub>Br<sub>x</sub>Cl<sub>y</sub>

Heat treatment is very important for nucleation of perovskite crystals. In the common program, the solution-containing PbI<sub>2</sub> and MAI is spin-coated on a substrate at room temperature and then postheated on a hot plate. Nie et al. reported a hot-casting technique to prepare a perovskite film with millimeter-scale crystalline grains, which achieved an ≈18% solar cell efficiency.<sup>[89]</sup> Study revealed that hot-casting technique was helpful to the grown of crystalline grains of the perovskite film. In hot-casting processing, excess solvent was present while the substrate was held at above the crystallization temperature for forming the perovskite phase. Excess solvent prolonged the growth of the perovskite crystals, resulting in large-size crystalline grains. Therefore, high-boiling point solvents would be helpful in growing large crystalline grains because the excess solvent could provide more time for perovskite crystal growth. In Chiang et al.'s work, solar modules (active area of 25.2 cm<sup>2</sup>) based on three types halide (Cl/Br/I) mixed perovskites with the highest efficiency of 14.3% was achieved by one-step hot solution spin-coating (HSS) method combined with solvent annealing (SA).<sup>[90]</sup> SEM images (**Figure 10B**) revealed that the

**Table 2.** Representative reports of large-area PSCs or PSMs using perovskite materials with halide substitution, monovalent organic cation substitution and mixed cation substitution as the active layer.

Perovskite	Module area [cm <sup>2</sup> <sup>a</sup> ]	Active area [cm <sup>2</sup> ]	Aperture area [cm <sup>2</sup> ]	V <sub>oc</sub> [V]	J <sub>sc</sub> [mA cm <sup>-2</sup> ]	I <sub>sc</sub> [mA]	FF [%]	PCE [%] <sup>b</sup>	Device structure	Type <sup>c</sup>	Processing method/steps	Ref.
MAPbI <sub>3-x</sub> Cl <sub>x</sub>	√	16.8 (3.36 × 5)	25	4.31	–	–32.9	60.3	5.081	FTO/c-TiO <sub>2</sub> /m-TiO <sub>2</sub> /perovskite/Spiro-OMeTAD/Au	M	Spin coating/1	[80]
				4.45	–	–36.8	52.6	5.1	FTO/c-TiO <sub>2</sub> /m-TiO <sub>2</sub> /perovskite/P3HT/Au	M		
MAPbI <sub>3-x</sub> Cl <sub>x</sub>	√	10.08	–	3.36	–13.4	–33.8	77.8	8.2	FTO/c-TiO <sub>2</sub> /m-TiO <sub>2</sub> /perovskite/P3HT/Au	M	Spin coating/1	[61]
MAPbI <sub>3-x</sub> Cl <sub>x</sub>	√	10.8 (2.7 × 4)	–	3.37	22.2	57.1	56.0	10.5	FTO/TiO <sub>2</sub> nanorods/perovskite/Spiro-OMeTAD/Au	P	Spin coating/1	[81]
MAPbI <sub>3-x</sub> Cl <sub>x</sub>	4 (1 × 4)	–	4	0.91	19.9	–	75.0	13.6	FTO/c-TiO <sub>2</sub> /perovskite/Spiro-OMeTAD/Au	p	Spin coating/1	[82]
MAPbI <sub>3-x</sub> Cl <sub>x</sub>	–	1.2	–	1.11	21.4	–	72.9	17.3	FTO/Au busbar/c-TiO <sub>2</sub> -PCBM/perovskite/Spiro-OMeTAD/Au	P	Blade coating/1	[83]
MAPbI <sub>3-x</sub> Cl <sub>x</sub>	5.6 × 5.6	7.92/flexible	–	3.39	–5.2	–	71	3.1	PET/ITO/c-TiO <sub>2</sub> /m-TiO <sub>2</sub> /perovskite/Spiro-OMeTAD/Au	M	Spin coating/1	[84]
MAPbI <sub>3-x</sub> Cl <sub>x</sub>	–	Flexible	–	0.87	13.91	–	59.0	7.14	ITO/PEDOT:PSS/perovskite/PC <sub>61</sub> BM/Bis-C <sub>60</sub> /Ag	I	Blade coating/1	[85]
MAPbI <sub>3-x</sub> Cl <sub>x</sub>	–	–	–	0.94	15.6	–	64.0	9.4	ITO/PEDOT:PSS/perovskite/PCBM/ZnO/Ag	I	Spin coating/1	[86]
MAPbI <sub>3-x</sub> Cl <sub>x</sub>	–	6	–	0.87	16.91	–	69.0	10.15	ITO/PEDOT:PSS/perovskite/PC <sub>60</sub> BM/Ca/Al	I	Blade coating/1	[87]
MAPbI <sub>3-x</sub> Cl <sub>x</sub>	25 (5 × 5)	12 (4 × 3)	–	2.71	6.48	–	63.8	11.2	ITO/PEDOT:PSS/perovskite/PC <sub>61</sub> BM/TIPD/Al	I	Spin coating/1	[72]
MAPbI <sub>3-x</sub> Br <sub>x</sub>	–	–	3.8	3.31	–	19.4	70.0	11.7	FTO/TiO <sub>2</sub> /perovskite/Spiro-OMeTAD/Au	I	Spray coating/1	[88]
MAPbI <sub>3-x-y</sub> Br <sub>x</sub> Cl <sub>y</sub>	–	25.2 (2.8 × 9)	–	9.05	–	53.5	74.4	14.3	ITO/PEDOT:PSS/perovskite/PC <sub>60</sub> BM/Ca/Al	I	Hot spin coating/1	[90]
FAPbI <sub>3</sub>	25 (5 × 5)	8.8 (5 cell)	–	0.98	16.9	–	57.0	9.5	FTO/c-TiO <sub>2</sub> /m-TiO <sub>2</sub> /perovskite/Spiro-OMeTAD/Au	M	CVD/2	[53]
				0.94	17.8	–	54.0	9				
FAPbI <sub>3</sub>	–	1.2	–	1.03	20.70	–	72.34	15.42	ITO/PEDOT:PSS/perovskite/n-doped PC <sub>61</sub> BM/Ag	I	Sequential deposition/2	[99]
FAPbI <sub>3</sub>	–	1.2	–	1.05	22.35	–	64.9	15.23	ITO/PEDOT:PSS/perovskite/n-doped PC <sub>61</sub> BM/Ag	I	Blade coating /2	[100]



**Table 2.** Continued.

Perovskite	Module area [cm <sup>2</sup> ] <sup>a)</sup>	Active area [cm <sup>2</sup> ]	Aperture area [cm <sup>2</sup> ]	V <sub>oc</sub> [V]	J <sub>sc</sub> [mA cm <sup>-2</sup> ]	I <sub>sc</sub> [mA]	FF [%]	PCE [%] <sup>b)</sup>	Device structure	Type <sup>c)</sup>	Processing method/steps	Ref.
FA <sub>0.81</sub> MA <sub>0.15</sub> PbI <sub>2.51</sub> Br <sub>0.45</sub>	–	1	–	1.143	22.6	–	76.0	19.6/ Newport	FTO/c-TiO <sub>2</sub> / m-TiO <sub>2</sub> /perovskite/ Spiro-OMeTAD/Au	M	Vacuum flash/1	[102]
FA <sub>0.85</sub> MA <sub>0.15</sub> Pb(I <sub>0.85</sub> Br <sub>0.15</sub> ) <sub>3</sub>	–	1.022	–	1.081	21.95	–	78.4	18.21/AIST	FTO/NiO <sub>2</sub> /perovskite/ PCBM/Ti(Nb)O <sub>x</sub> /Ag	I	Spin coating/1	[103]
PbI <sub>2</sub> /PbBr <sub>2</sub> /FAI/ MABr/I <sup>-</sup>	–	1	–	1.1	24.7	–	72.3	19.7/ Newport	FTO/c-TiO <sub>2</sub> / m-TiO <sub>2</sub> ;perovskite/ perovskite/PTAA/Au	M	Spin coating/2	[30]
FA <sub>0.85</sub> MA <sub>0.15</sub> Pb(I <sub>0.85</sub> Br <sub>0.15</sub> ) <sub>3</sub>	–	–	16	1.13	17.3	–	61.9	12.1	FTO/metal grid/ c-TiO <sub>2</sub> / m-TiO <sub>2</sub> /perovskite/ Spiro-OMeTAD/Au	M	Spray antisolvent method/1	[108]
Cs <sub>0.05</sub> FA <sub>0.81</sub> MA <sub>0.14</sub> PbI <sub>2.55</sub> Br <sub>0.45</sub>	–	1.1	–	1.195	21.5	–	75.7	19.5/ Newpot	FTO/TiO <sub>2</sub> -Cl/ perovskite/ Spiro-OMeTAD/Au	P	Spin coating/1	[110]
Cs <sub>0.05</sub> FA <sub>0.79</sub> MA <sub>0.16</sub> PbI <sub>2.49</sub> Br <sub>0.51</sub>	–	–	1.0	1.11	23.8	–	74.0	19.6	FTO/ m-TiO <sub>2</sub> / perovskite/interlayer/ Spiro-OMeTAD/Au	M	Spin coating/1	[111]
Cs <sub>0.07</sub> FA <sub>0.93</sub> PbI <sub>3</sub>	25 (5 × 5)	12 (2 × 6)	–	5.84	3.67	–	68.1	14.6	FTO/c-TiO <sub>2</sub> /perovskite/ Spiro-OMeTAD/Au	P	CVD/cation exchange/2	[114]
K <sub>x</sub> Cs <sub>0.05</sub> (FA <sub>0.85</sub> MA <sub>0.15</sub> ) <sub>0.95</sub> Pb(I <sub>0.85</sub> Br <sub>0.15</sub> ) <sub>3</sub>	36 (6 × 6)	20 (6 cell)	–	6.794	3.57	–	65.0	15.76	FTO/c-SnO <sub>2</sub> / perovskite/ Spiro-OMeTAD/Au	P	Spin coating/1	[115]

<sup>a)</sup>√ = not given specific area value; <sup>b)</sup>PCEs are certified by Newport Corp. or AIST; <sup>c)</sup>M = mesoporous n-i-p configuration, P = planar n-i-p configuration, and I = inverted p-i-n configuration.

mixed halide perovskite film prepared with the HSS method was very smooth and the grain size was larger than that prepared from the cold precursor solution. In addition, the solvent annealing process further enlarged the grain size of the perovskite thin film. They found that in the precursor solution Cl could improve the film morphology by slowing down the crystallization of the perovskite crystals, while Br could increase the open-circuit voltage (V<sub>oc</sub>) of the corresponding devices and stabilize the perovskite lattices.

### 3.3. Modification on A Position in ABX<sub>3</sub> Perovskite

#### 3.3.1. Modify A by Small Organic Cations (A = FA, MA)

In the ABX<sub>3</sub> perovskites, another strategy of tuning structure is to replace the cations. For MAPbI<sub>3</sub>, much unfavorable instnct factors limit its application, such as a low reversible phase transition temperature (54–57 °C),<sup>[91]</sup> easy degradation against moisture, and low thermal stability, which is believed to cause reduced performance and stability.<sup>[92,93]</sup> In addition, much concern has been focused on the light-induced trap-state formation and halide segregation in mixed-halide perovskites MAPbBr<sub>x</sub>I<sub>3-x</sub>.<sup>[94]</sup> However, formamidinium lead triiodide (CH(NH<sub>2</sub>)<sub>2</sub>PbI<sub>3</sub> or FAPbI<sub>3</sub>) exhibited better temperature stability than MAPbI<sub>3</sub>.<sup>[95]</sup> In addition, FAPbI<sub>3</sub> has a bandgap of 1.48 eV, which is closer to the “ideal” bandgap (≈1.1–1.4 eV) of single-junction solar cells, thus enabling efficient solar photon harvesting.<sup>[96]</sup>

In 2015, Leyden et al. used a chemical vapor deposition (CVD) method to fabricate FAPbI<sub>3</sub>-based solar cells with 1 cm<sup>2</sup> active area, which achieved a PCE of 7.7%.<sup>[97]</sup> After 1 year, by using the same deposition process, FAPbI<sub>3</sub>-based PSMs on 5 cm × 5 cm substrates with PCEs of 9.5% (active area 8.8 cm<sup>2</sup>) and 9.0% (active area 12 cm<sup>2</sup>) were obtained by the same group.<sup>[53]</sup> Perovskite films were prepared by a two-step process where PbI<sub>2</sub> was firstly deposited onto TiO<sub>2</sub>/FTO substrates, followed by CVD deposition of FAI to convert films to perovskites (Figure 11A). Moreover, solar modules using FAPbI<sub>3</sub> perovskite films grown by CVD show much better thermal stability. At the end of 2017, Borchert et al. used a coevaporation process to deposit a homogeneous FAPbI<sub>3</sub> thin films with a large area of 8 cm × 8 cm.<sup>[98]</sup> The FAPbI<sub>3</sub> film exhibited a high carrier mobility of 26 cm<sup>2</sup> V<sup>-1</sup> s<sup>-1</sup> and a very low surface roughness with an RMS of only 6.2 nm. This method could precisely control the film thickness and achieve highly uniform, pinhole-free layers (Figure 11B). CVD and coevaporation processes offer a strategy for smooth and uniform perovskite films over large areas, as well as semitransparent solar cells. However, the disadvantage of these high-vacuum processing technologies is time and energy consuming. Chang et al. reported FAPbI<sub>3</sub>-based PSCs with an active area of 1.2 cm<sup>2</sup> by solution-sequential deposition and doctor-blade coating, respectively. Both of two PSCs exhibited remarkable PCEs of more than 15%.<sup>[99,100]</sup> Nevertheless, pure FAPbI<sub>3</sub> phase at room temperature is structurally unstable due to its crystallization to either a photoinactive, non-perovskite hexagonal δ-phase (“yellow phase”) or a photoactive perovskite α-phase (“black phase”).<sup>[91,96]</sup> The latter is sensitive

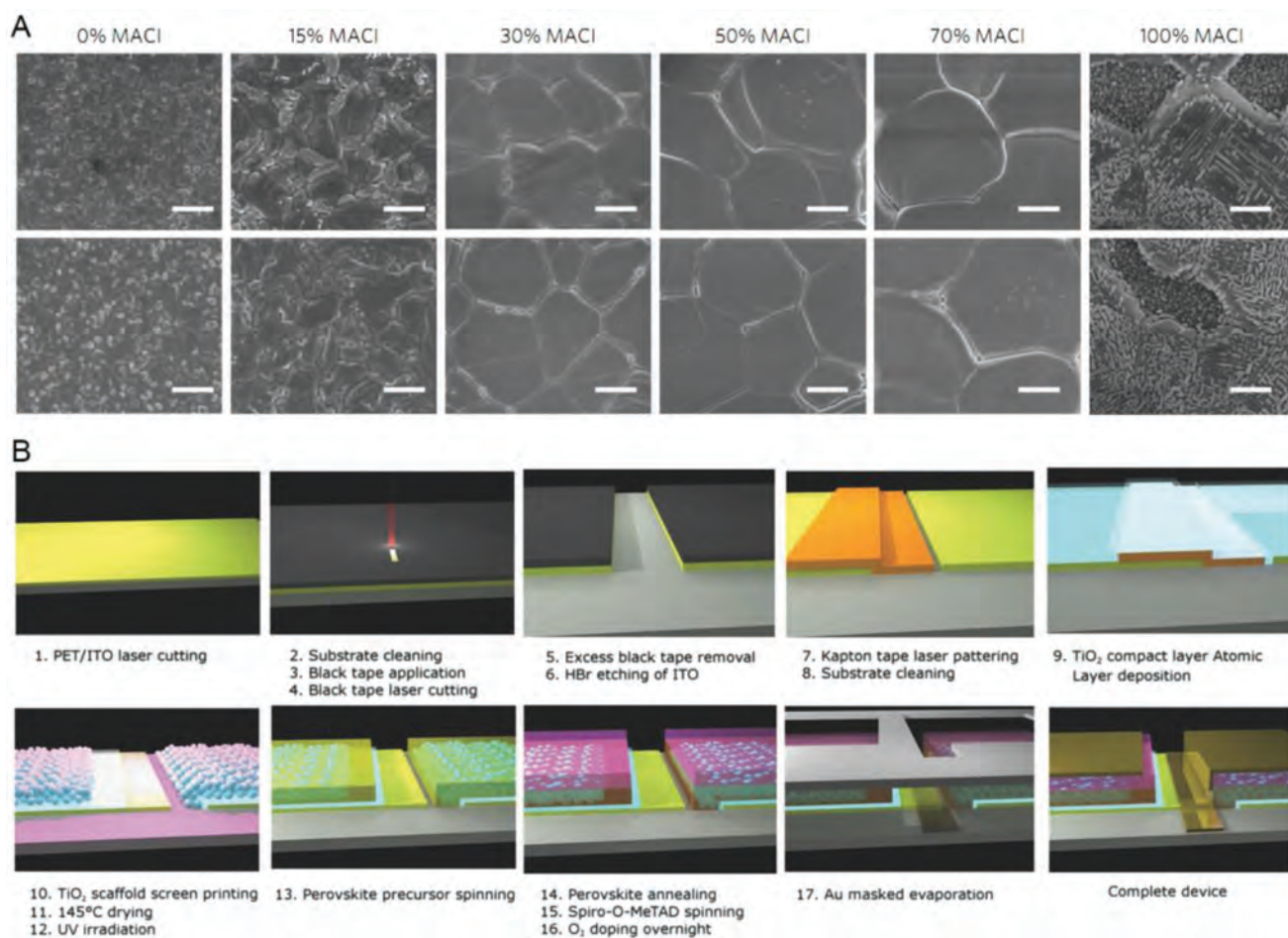


**Figure 9.** A) Top-view SEM images of perovskite films prepared with different excess amounts of MACl using blade-coating (top row) and spin-coating (bottom row) methods. Scale bars are 1  $\mu\text{m}$ . Reproduced with permission.<sup>[83]</sup> Copyright 2017, Nature Publishing Group. B) Schematics of the module fabrication procedures. Reproduced with permission.<sup>[84]</sup> Copyright 2015, Wiley-VCH.

to polar solvents or humidity.<sup>[101]</sup> The summarized data of this part are listed in Table 2.

The perovskite can be further tuned by appropriately selecting different organic cations. The perovskites containing mixed FA/MA organic cations have shown the better performance and stability than the pure perovskite compounds. In spite of more advantages of FA, MA can make the perovskite structure stable and avoid its transformation into the yellow polymorph as known for the FA perovskites.<sup>[2]</sup> Li et al. fabricated FA<sub>0.81</sub>MA<sub>0.15</sub>PbI<sub>2.51</sub>Br<sub>0.45</sub>-based PSCs with a square aperture area of more than 1 cm<sup>2</sup> by using a simple vacuum-flash solution processing (VASP) method, achieving a maximum PCE of 20.5% and a certified PCE of 19.6%.<sup>[102]</sup> In this method (Figure 12Aa), an m-TiO<sub>2</sub> film was firstly spin-coated with the perovskite precursor solution, subsequently being placed into a vacuum chamber for a few seconds to accelerate the crystallization of the perovskite mesophase by removal of most of the residual GBL and DMF solvents. SEM images (Figure 12Ab) revealed that the VASP method yielded homogeneous films without pinholes compared to conventional process. Hence, very few grain boundaries could be seen on the surface of the perovskite layer, which retarded nonradiative recombination of

charge carriers, thus enhancing the device photovoltage. Wu et al. reported a 1.022 cm<sup>2</sup> aperture-area inverted PSC based on mixed-cation/halide perovskite of FA<sub>0.85</sub>MA<sub>0.15</sub>Pb(I<sub>0.85</sub>Br<sub>0.15</sub>)<sub>3</sub>, which exhibited a remarkable PCE of 18.21%.<sup>[103]</sup> The high PCE was owing to the perovskite-fullerene graded heterojunction (GHJ) structure, which significantly improved the photovoltaic performance of PSCs. In mid-2017, Yang et al. reported the certified PCEs of 22.1% in small PSCs and 19.7% in 1 cm<sup>2</sup> devices by the defect engineering of perovskite films.<sup>[30]</sup> This is the highest certified efficiency for 1 cm<sup>2</sup> PSCs. Additional iodide ions were introduced into the organic cation solution to form the perovskite films by an intramolecular exchanging process, which reduced the concentration of deep-level defects. Antisolvent method (Figure 12B) is popularly used in preparing perovskite film, which was first reported in 2014.<sup>[24,104]</sup> During the spin-coating process of a perovskite precursors, an antisolvent, such as chlorobenzene or toluene, is poured on top of the spinning film, which will boost crystallization and form a good film morphology.<sup>[105–107]</sup> Although antisolvent process can produce a high-quality perovskite film, the dropping of antisolvent during spinning over a large area is difficult to control. In the recent work of Kim et al., a spray antisolvent



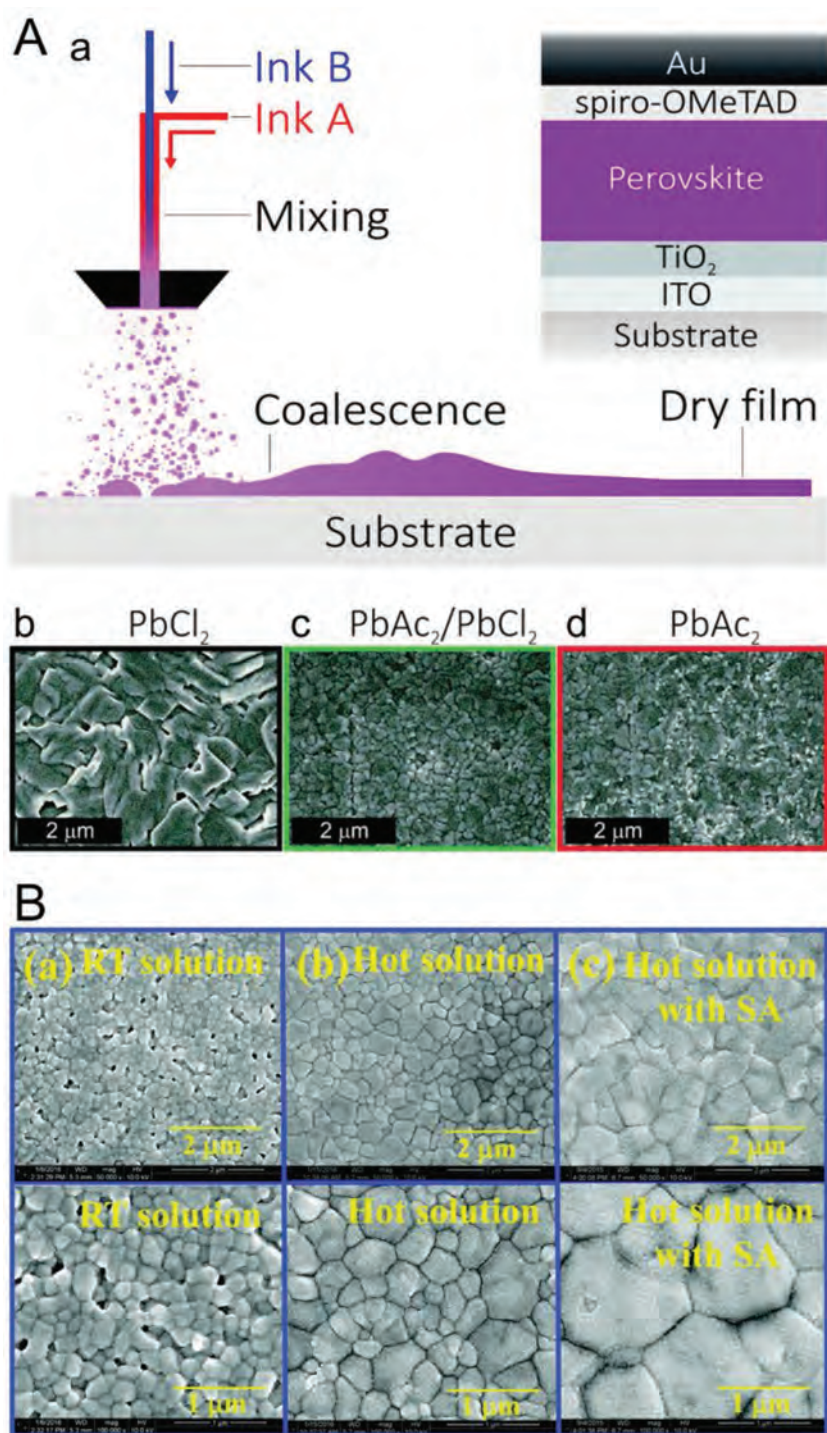


**Figure 10.** A) Schematic of concurrently pumped ultrasonic spray coating for perovskite precursor deposition a). The inks ultrasonically mix inside the nozzle, prior to aerosolization. The inset shows the basic device architecture with  $\text{CH}_3\text{NH}_3(\text{I}_x\text{Br}_{1-x})_3$  perovskite. SEM images of perovskite films sprayed from inks of b)  $\text{PbCl}_2/\text{MAI}$ , c) concurrently pumped  $\text{PbAc}_2/\text{MAI}$  with  $\text{PbCl}_2/\text{MAI}$  at 75 mol%  $\text{PbAc}_2$ , and d)  $\text{PbAc}_2/\text{MAI}$ . A) Reproduced with permission.<sup>[88]</sup> Copyright 2016, Royal Society of Chemistry. B) SEM images of the mixed-halide perovskite film prepared by the a) cold solution spin-coating method and b) hot solution spin-coating method, c) combining the HSS and solvent annealing methods (top: low magnification; bottom: high magnification). B) Reproduced with permission.<sup>[90]</sup> Copyright 2016, Royal Society of Chemistry.

(SAS) method was developed to facilitate rapid nucleation and uniform crystallization of a large-area perovskite film with densely packed grains.<sup>[108]</sup> Compared to the conventional antisolvent dropping process, the SAS method showed many advantages such as less antisolvent usage, rapid delivery of the antisolvent, faster rate of supersaturation, denser nucleation, and greater uniformity over a large area. By incorporating a metal grid designed in PSCs, a large-area  $16 \text{ cm}^2$  cell with a certified efficiency of 12.1% was obtained.

### 3.3.2. Modify A by Inorganic Cations (A = Cs, K)

Although the mixed FA/MA perovskites show a good performance, it is still a challenge to obtain perovskite films without trace amounts of yellow phase even for high-efficiency PSCs.<sup>[25,109]</sup> The small amounts of yellow phase impurities in perovskites will remarkably affect the crystal growth and film morphology, which can depress efficient charge collection and thus decrease the device performance. In 2016, Saliba et al. first introduced Cs into MA/FA perovskite mixtures to restrain yellow phase impurities and form high-uniform perovskite grains growing from the electron transport layer to the hole collecting layer.<sup>[5]</sup> The small-area perovskite solar cells based on the mixture of triple Cs/MA/FA cations exhibited a steady PCE of 21.1%, which retained an output of 18% after 250 h under operational conditions. The triple-cation perovskite films possessed a good thermal stability and were not easy to be affected by temperature, solvent vapors, or heating protocols during the fabrication process. Tan et al. used an antisolvent process to fabricate a  $1.1 \text{ cm}^2$  active-area planar perovskite solar cells based on the mixed cation-halide perovskite  $\text{Cs}_{0.05}\text{FA}_{0.81}\text{MA}_{0.14}\text{PbI}_{2.55}\text{Br}_{0.45}$ , which was certified with a PCE of 19.5%.<sup>[110]</sup> Very recently, Lu et al. achieved an efficient and stable PSC by the interface modification of the  $\text{Cs}_{0.05}\text{FA}_{0.79}\text{MA}_{0.16}\text{PbI}_{2.49}\text{Br}_{0.51}$  perovskite.<sup>[111]</sup> The perovskite film was fabricated by a one-step antisolvent procedure, and  $1 \text{ cm}^2$  area PSCs exhibited a remarkable PCE of 19.6% and remained high stability. Although the superior Cs-containing PSCs can be prepared by using the antisolvent method,<sup>[112,113]</sup> the crystallization dynamics in this process heavily depend on the precise artisanship conditions, which blocks the device scaling-up.



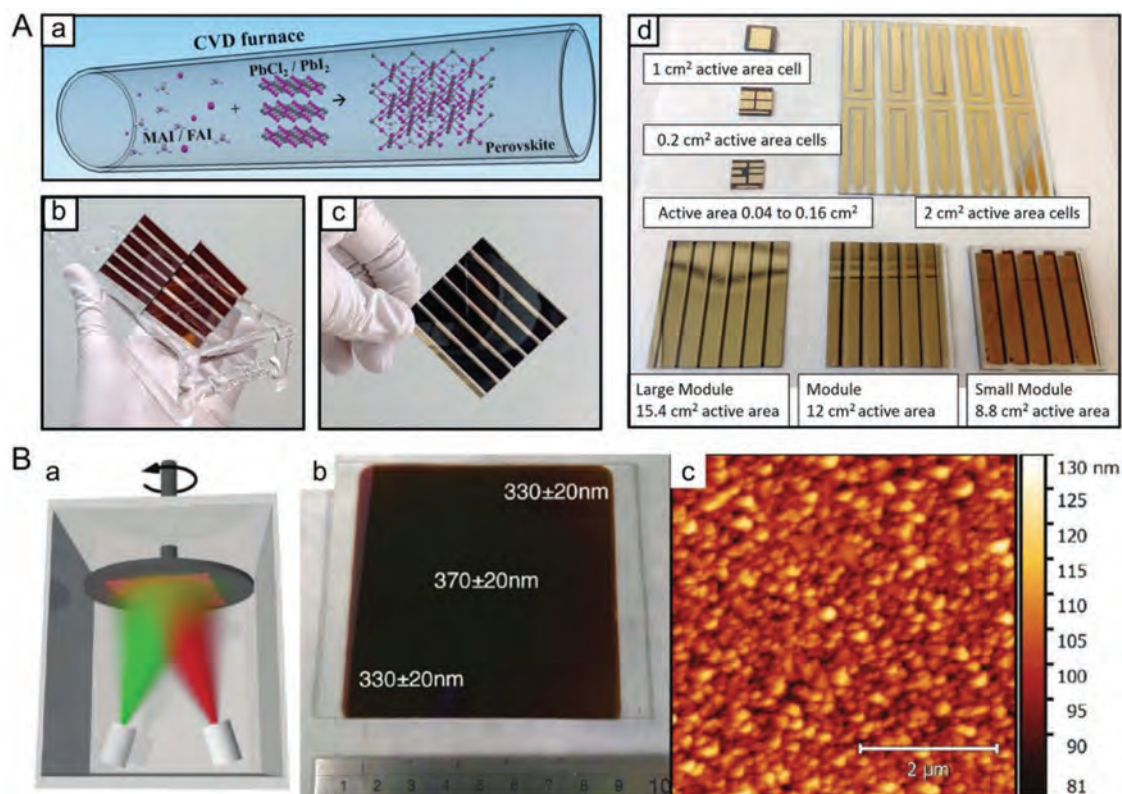


**Figure 11.** A) Schematic of perovskite growth by CVD a). b) Photograph of patterned perovskite films grown by CVD. c) Complete perovskite solar cell module grown by the CVD process, shown from the rear side. d) Photographs of cells and modules. A) Reproduced with permission.<sup>[53]</sup> Copyright 2016, Royal Society of Chemistry. B) Schematic diagram of the dual-source coevaporation system a). b) Photograph of 8 cm × 8 cm thin film of FAPbI<sub>3</sub> deposited on a glass substrate. The image shows the substrate after thermal annealing at 170 °C for 1 min. The results of thickness measurements at three positions are superimposed on the image, and a metal ruler with a centimeter scale is shown as a size reference. c) Atomic force micrograph of a 5 μm × 5 μm region of the sample. The surface was found to be very smooth with a root-mean-square roughness  $R_{\text{RMS}} = 6.2$  nm. B) Reproduced with permission.<sup>[98]</sup> Copyright 2017, American Chemical Society.

Jiang et al. reported a method to fabricate  $\text{Cs}_x\text{FA}_{1-x}\text{PbI}_3$  film with the adjustable Cs content from 0 to 24%.<sup>[114]</sup> As shown in Figure 12C, a FAPbI<sub>3</sub> film was firstly grown by hybrid chemical vapor deposition (HCVD), followed by immersion into Cs<sup>+</sup> solution for cation exchange. The champion PSM based on  $\text{Cs}_{0.07}\text{FA}_{0.93}\text{PbI}_3$  with an active area of 12.0 cm<sup>2</sup> exhibited an initial PCE of 14.6%, and still had a 14.0% efficiency after 1200 min steady-state measurement in a glove box with 5% RH. The good stability probably resulting from the Cs-rich perovskite surface improving the phase stability of the bulk film against moisture.

Bu et al. reported a novel quadruple-cation (K/Cs/FA/MA) perovskite. High PCEs of 15.76% (forward scan) and 15.56% (reverse scan) were achieved for 6 × 6 cm<sup>2</sup> modules with an active area of 20 cm<sup>2</sup>.<sup>[115]</sup> The eliminated hysteresis was ascribed to the enhanced conductivity and the reduced carrier recombination as well as the decreased trap density in the perovskite film. Besides, the quadruple-cation perovskite formed highly crystallized films with the double grain size (over 1 μm) compared to the K-free counterparts (Figure 12D). The unencapsulated PSMs exhibited an outstanding stability with no decrease in PCE over 1000 h under ambient air (10 ± 5 RH%). The detailed data are listed in Table 2.

### 3.3.3. Modify A by Large Organic Cations (A = Small Organic Cations, A' = Large Organic Cations)

In the above section, we reviewed 3D halide perovskite materials for large-scale devices. Although these compounds can accomplish high-efficiency PSCs, their ambient stability is still one of the bottleneck of commercialization. In conventional 3D perovskites, water intercalation,<sup>[116,117]</sup> ion migration,<sup>[94]</sup> and thermal instabilities<sup>[91]</sup> are still important factors in inducing the device degradation. 2D perovskites have good stability and film-forming properties, but their photovoltaic devices are not efficient mainly due to short exciton lifetime,<sup>[118]</sup> large exciton binding energy,<sup>[119,120]</sup> and narrow absorption spectrum. Recently, multidimensional perovskites have attracted a substantial interest due to their superior stability against heat and water.<sup>[121–123]</sup> Multidimensional perovskites usually have a structural formula of  $\text{A}'_2\text{An}_{-1}\text{BnX}_{3n+1}$ , where B is a divalent metal, X is a halide anion, as well as A and A' are the small organic cations and large organic cations, respectively. Layered perovskite structures can be formed by inserting the organic cation layers into the inorganic semiconductor sheets of corner-sharing  $[\text{BX}_6]$  octahedral, where  $n$  is the number of inorganic semiconductor  $[\text{BX}_6]$  sheets between the two large organic insulating layers

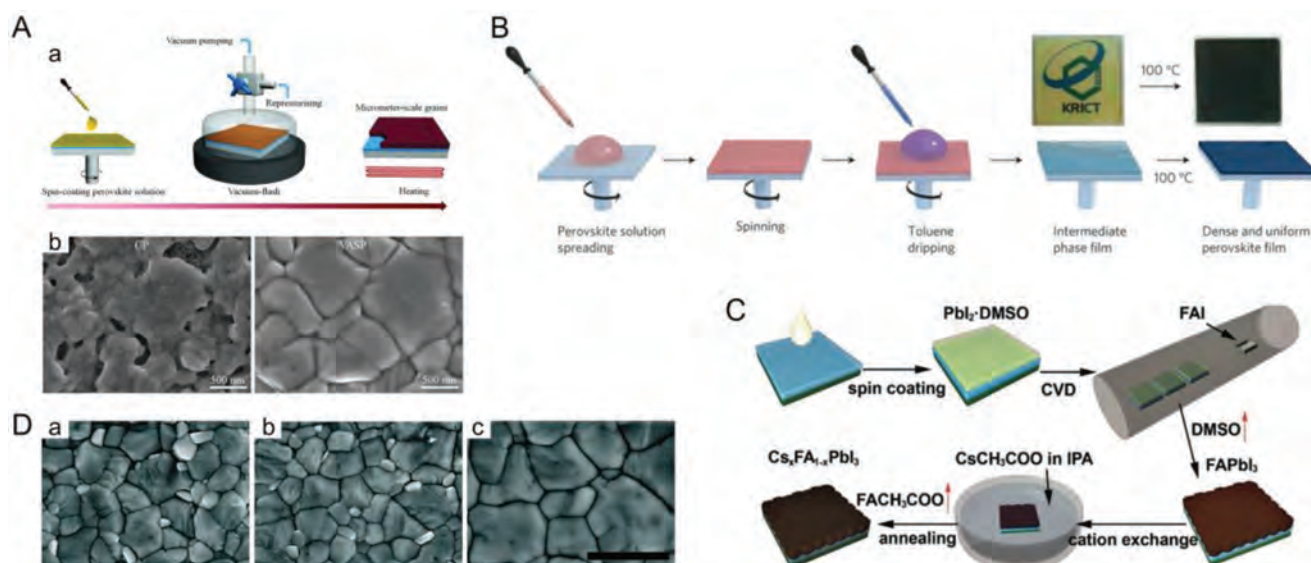


**Figure 12.** A) Schematic illustration of nucleation and crystallization procedures during the formation of perovskite film via vacuum flash-assisted solution processing a). Surface SEM images of the perovskite films fabricated by the conventional process and VASP b). A) Reproduced with permission.<sup>[102]</sup> Copyright 2016, American Association for the Advancement of Science. B) Solvent engineering procedure for preparing the uniform and dense perovskite film. Reproduced with permission.<sup>[24]</sup> Copyright 2014, Nature Publishing Group. C) Schematic drawing for the preparation of the mixed  $\text{Cs}_x\text{FA}_{1-x}\text{PbI}_3$  perovskite films by the HCVD-CE method and  $\text{Cs}^+$  bulk ratio in the mixed  $\text{Cs}_x\text{FA}_{1-x}\text{PbI}_3$  films. Reproduced with permission.<sup>[114]</sup> Copyright 2018, Wiley-VCH. D) SEM images of a) FA/MA, b) Cs/FA/MA, and c) K/Cs/FA/MA perovskite films. The scale bar is 1  $\mu\text{m}$ . D) Reproduced with permission.<sup>[115]</sup> Copyright 2017, Royal Society of Chemistry.

(cation  $\text{A}'$ ). In the extreme case, the multilayered perovskites form a 2D structure of  $\text{A}'_2\text{BX}_4$  for  $n = 1$  or a 3D counterpart of  $\text{ABX}_3$  for  $n = \infty$ , as shown in **Figure 13**. It has been revealed that the intercalation of large organic ammonium between the inorganic semiconductor layers could increase the formation energy of perovskites, therefore improving material stability.<sup>[124]</sup>

In the early work, large-size ammonium ions were used as additives to passivate the surface of 3D perovskites. In fact, the modified perovskites can be considered to be close to the limit of multidimensional analogs ( $n = \infty$ ). In 2014, Mei et al. reported perovskite solar cells based on the precursor solution containing 5-ammoniumvaleric acid (5-AVA) iodide,  $\text{PbI}_2$ , and MAI.<sup>[41]</sup> The mixed-cation  $(5\text{-AVA})_x(\text{MA})_{1-x}\text{PbI}_3$  perovskites showed low defect density and good pore-filling as well as

complete contact with the  $\text{m-TiO}_2$  scaffold. This was because the end  $-\text{NH}_3^+$  groups of 5-AVA can act as nucleation sites for the perovskite growth when the COOH groups were anchored on the surface of the mesoporous  $\text{TiO}_2$  and  $\text{ZrO}_2$  film by coordinate bonds to the exposed Ti(IV) or Zr(IV) ions. The small device achieved a certified PCE of 12.8% and was stable for more than 1000 h in ambient air under AM1.5G sunlight illumination. The presence of 5AVA promoted the formation of passivated 3D perovskite, which was more conducive to the device stability. Li and co-workers found that the phosphonic acid ammonium (4-ABPA) additive could cross-link the neighboring grains of the perovskite film by strong hydrogen bonding of the  $-\text{PO}(\text{OH})_2$  and  $-\text{NH}_3^+$  end groups with the perovskite surface (**Figure 14**).<sup>[125]</sup> The bifunctional 4-ABPA cations improved the

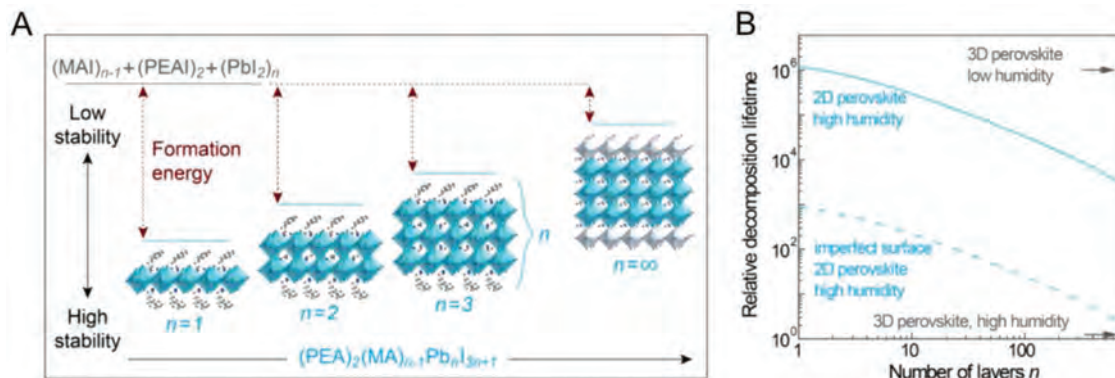


**Figure 13.** Energetics of perovskite formation and stability. A) Unit cell structure of perovskites with different  $n$  values, showing the evolution of dimensionality from 2D ( $n = 1$ ) to 3D ( $n = \infty$ ). B) DFT simulation of the formation energy of perovskite with different  $n$  values in different atmospheres. A, B) Reproduced with permission.<sup>[124]</sup> Copyright 2016, American Chemical Society.



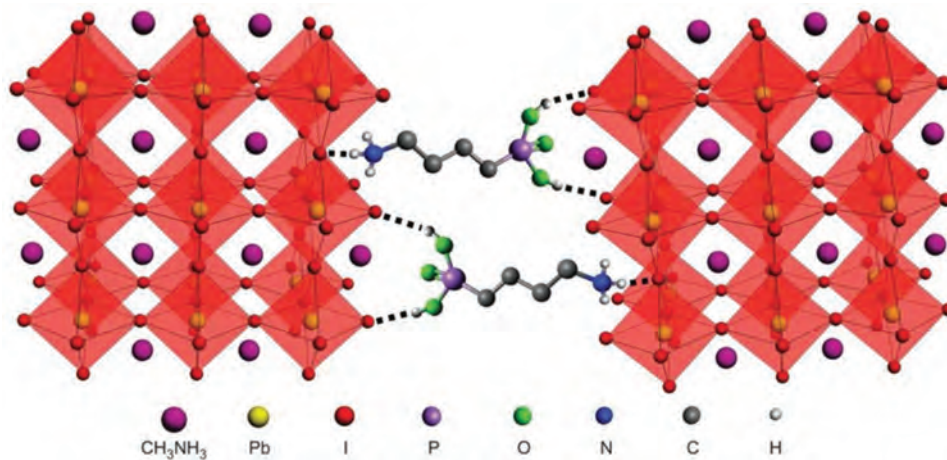


**Figure 14.** Schematic illustration of two neighboring grain structures in which the methyl ammonium groups are shown as one sphere for clarity, and the  $\text{PbI}_6^{4-}$  octahedra are shown in red, crosslinked by butylphosphonic acid 4-ammonium chloride (4-ABPACl) hydrogen-bonding interactions ( $\text{O}-\text{H}\cdots\text{I}$  and  $\text{N}-\text{H}\cdots\text{I}$ ) of the iodide from the iodoplumbate complex with the phosphonic acid ( $-\text{PO}(\text{OH})_2$ ) and the ammonium ( $-\text{NH}_3^+$ ) end groups of the 4-ABPACl species. Reproduced with permission.<sup>[125]</sup> Copyright 2015, Nature Publishing Group.

growth of perovskite crystals in the mesoporous network and created smooth capping layers. Such bifunctional additives act as surface-passivating, growth-controlling, and crosslinking agents, which offers a novel and effective method toward engineering metal halide perovskites for large-scale applications.

Priyadarshi et al. reported  $(5\text{-AVA})_x(\text{MA})_{1-x}\text{PbI}_3$  perovskite modules with the PCEs of 10.46% and 10.74% for the active areas of 31 and 70  $\text{cm}^2$ , respectively. The module retained more than 95% of its initial efficiency after aging 2000 h under an ambient condition.<sup>[126]</sup> Hu et al. reported a perovskite solar module employing a mixed-cation lead halide perovskite  $(5\text{-AVA})_x(\text{MA})_{1-x}\text{PbI}_3$  as the light harvester and a mesoporous  $\text{TiO}_2/\text{ZrO}_2$ /carbon layer as the scaffold.<sup>[127]</sup> The module ( $10 \times 10 \text{ cm}^2$ ) had an active area of 49  $\text{cm}^2$  and showed a 10.4% PCE. Light-stress stability of 1000 h and local outdoor stability of 1 month, as well as shelf-life stability of over 1 year have also been demonstrated. The 5AVA molecules were considered to act as a template to form perovskite crystals with low defect density and good contact with the m- $\text{TiO}_2$  scaffold.

Grancini et al. showed 1 year stable perovskite devices based on an ultrastable 2D/3D perovskite junction by using the aminovaleric acid iodide (AVAI).<sup>[128]</sup> The  $(\text{AVA})_2\text{PbI}_4/\text{CH}_3\text{NH}_3\text{PbI}_3$  formed an exceptional gradually organized multidimensional interface, which yielded up to 11.2% efficiency in  $10 \times 10 \text{ cm}^2$  solar modules by a fully printable industrial-scale process. The module that was measured showed no loss in efficiency after aging more than 10 000 h under light-soaking (AM1.5G,  $100 \text{ mW cm}^{-2}$ ) and thermal ( $55 \text{ }^\circ\text{C}$ ) dual stress at a short-circuit condition (**Figure 15**). Lu et al. introduced ethane-1,2-diammonium ( $^+\text{NH}_3(\text{CH}_2)_2\text{NH}_3^+$ ,  $\text{EDA}^{2+}$ ) cations into  $\text{MAPbI}_3$  perovskite and demonstrated a 2D/3D perovskite solar cell (aperture area of  $1.04 \text{ cm}^2$ ) with a certified PCE of  $15.2\% \pm 0.5\%$  when 0.8 mol%  $\text{EDA}^{2+}$  was used.<sup>[129]</sup> Furthermore, the mixed-cation perovskite films showed greatly improved structure stability under the environmental stimuli. Under a simulated operating condition (AM1.5G illumination, 50% RH,  $50 \text{ }^\circ\text{C}$  device temperature), the mixed-cation perovskite solar cell retained 75% of its initial PCE after aging 72 h. On the

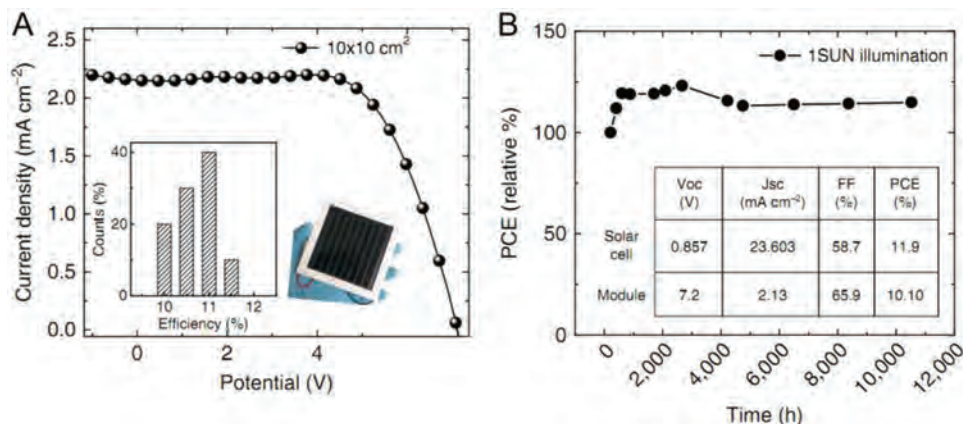


**Figure 15.** A)  $J$ - $V$  curve using the 2D/3D perovskite with 3% AVAI in an HTM-free  $10 \times 10 \text{ cm}^2$  module (device statistics and picture in the inset). B) Typical module stability test under 1 sun AM1.5G conditions at stabilized temperature of  $55 \text{ }^\circ\text{C}$  and at short circuit conditions. Stability measurements done according to the standard aging conditions. A,B) Reproduced with permission.<sup>[128]</sup> Copyright 2017, Nature Publishing Group.



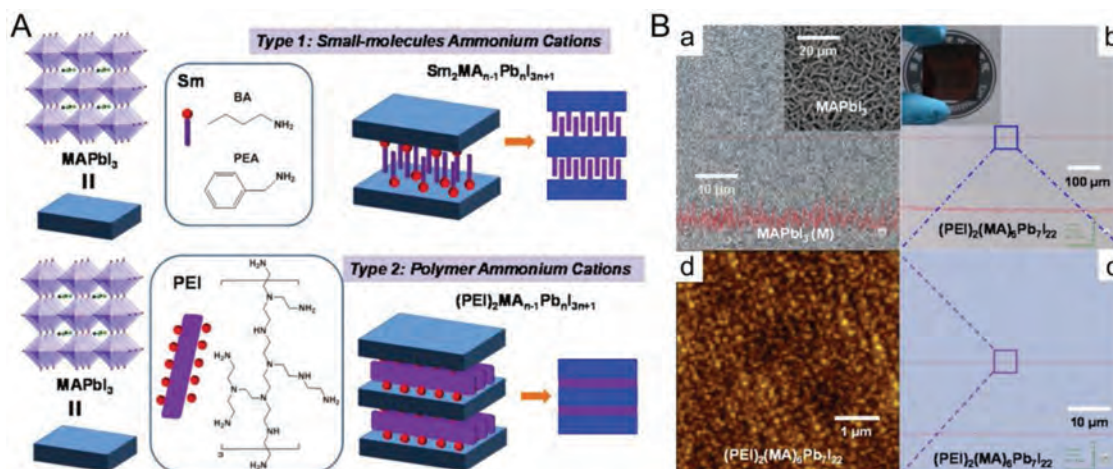


**Figure 16.** A) Schematic representation of the stacking structures of multilayered perovskite based on different ammonium cations. B) Optical image of MAPbI<sub>3</sub> a). Optical images of (PEI)<sub>2</sub>(MA)<sub>6</sub>Pb<sub>7</sub>I<sub>22</sub> in b) large scale and c) small scale. (d) top-surface AFM image of (PEI)<sub>2</sub>(MA)<sub>6</sub>Pb<sub>7</sub>I<sub>22</sub>. A, B) Reproduced with permission.<sup>[130]</sup> Copyright 2016, American Chemical Society.

contrary, the MAPbI<sub>3</sub>-based reference has almost completely degraded in only 15 h.

Besides small-molecule organic cations, polymeric organic cations have applications in fabricating multidimensional perovskites with high ambient stability. Yao et al. have successfully fabricated large-size (aperture area of 2.32 cm<sup>2</sup>) solar cells with a maximum efficiency of 8.77%.<sup>[130]</sup> Polyethylenimine hydrochloride (PEI·HI) was utilized to form stable multidimensional perovskite films of (PEI)<sub>2</sub>(MA)<sub>6</sub>Pb<sub>7</sub>I<sub>22</sub>. The introduced polymeric ammonium induced the close stacking of the inorganic unit layers, which improved the charge transfer (Figure 16A). Moreover, the multilayered perovskites can easily form ultrasmooth, pinhole-free, and highly dense thin films, which showed good stability against moisture compared to their 3D MAPbI<sub>3</sub> analog (Figure 16B). The summarized data of the multidimensional perovskites are listed in Table 3.

As discussed in the above sections, multidimensional perovskites have opened a door to enhance both efficiency and stability for large-scale PSCs. The rational design and selection of organic cations for multidimensional perovskites is a key strategy for improving ambient stability of the PSCs (or PSMs) while maintaining their high efficiencies.

#### 4. Hole Transport Materials

Hole transport materials in PSCs play an important role in efficient hole extraction at the perovskite/HTM interface and rapid charge transport to the anode, as well as influencing  $V_{oc}$  by determining the splitting of quasi-Fermi levels of the PSC.<sup>[131–133]</sup> Moreover, HTMs can also prevent the perovskite degradation originated from metal electrode and humidity.<sup>[134]</sup> As an ideal HTM candidate for large-area PSCs, the following features are required. 1) Well-aligned energy levels with perovskites: HOMO level must be less negative than that of perovskites for efficient hole extraction, while the high-lying LUMO level will ensure low electron affinity to enable a beneficial electron blocking property. 2) High hole mobility: For reducing losses

during hole transport to the contact, the mobility of HTMs is usually required to be more than 10<sup>-3</sup> cm<sup>2</sup> V<sup>-1</sup> s<sup>-1</sup>. 3) Well solubility: HTMs should be easy to dissolve in nonpolar and aprotic solvents for facilitating film formation and avoiding perovskite dissolution. 4) High thermal and photochemical stability as well as high hydrophobicity: The intrinsic stability of HTMs and their protection of perovskites from water are an efficient strategy for retarding the degradation of PSCs in a long-term durable photovoltaic operation. 5) Low cost: To ensure low-cost large-scale PSC manufacturing, ideal HTMs should be easily affordable by simple synthetic schemes, including minimum steps and easy purification procedures for cost-effective upscale.

Since Spiro-OMeTAD was first reported as the HTM in solid-state dye-sensitized solar cells two decades ago,<sup>[135]</sup> it has still become a dominant HTM in the PSC field, achieving a benchmark PCE of 20.8% in small-scale n-i-p PSCs (Figure 19).<sup>[4]</sup> Spiro-OMeTAD exhibits a compatible HOMO level of -5.22 eV with the perovskites and high solubility in nonpolar solvents such as chlorobenzene or toluene, as well as almost no absorption in the visible region. For the large-area PSCs, Spiro-OMeTAD was also the most common p-type material used in n-i-p device structure.<sup>[52,53,59,61,65,68,70,81,82,88,102,110,114,115,129]</sup> However, two drawbacks have restricted the development of its industrialization. 1) High cost: The synthesis steps are complex, and the sublimation purification is required to obtain high-purity products, resulting in the high cost of ~500 \$ g<sup>-1</sup> (high purity, Merck).<sup>[4,8]</sup> 2) Low hole mobility and poor long-term stability: The hole mobility of Spiro-OMeTAD is about 5.3 × 10<sup>-5</sup> cm<sup>2</sup> V<sup>-1</sup> s<sup>-1</sup>, which needs to be improved by doping lithium trifluoromethanesulfonimide (Li-TFSI), 4-*tert*-butylpyridine (TBP), and cobalt(III) complex (FK209) (Figure 17).<sup>[4]</sup> However, the use of dopants not only increase the manufacturing cost of PSCs but also seriously reduce the device lifetime, mainly stemming from the hygroscopic nature of the lithium salt and the chemical degradation of the Co(III) complex.<sup>[136]</sup> In the past few years, a lot of organic small-molecule and polymeric HTMs have been developed as alternatives to Spiro-OMeTAD, but only a few materials can achieve the efficiency of more than 20% in small area

**Table 3.** Representative reports of large-area PSCs or PSMs using multidimensional perovskites as the active layers.

Perovskite	Module area [cm <sup>2</sup> ]	Active area [cm <sup>2</sup> ]	Aperture area [cm <sup>2</sup> ]	V <sub>oc</sub> [V]	J <sub>sc</sub> [mA cm <sup>-2</sup> ]	FF [%]	PCE [%] <sup>a)</sup>	Device structure	Type <sup>b)</sup>	Processing method/steps	Ref.
(5-AVA) <sub>x</sub> (MA) <sub>1-x</sub> PbI <sub>3</sub>	50(5 × 10)	31 (4 cell)	–	3.72	19.6/strip	57.5	10.46	FTO/c-TiO <sub>2</sub> /m-TiO <sub>2</sub> /perovskite/ZrO <sub>2</sub> /Carbon	M	Screen printing and drop casting/1	[126]
	50(5 × 10)	31.7 (4 cell)	–	3.766	20.96/strip	47	9.11/Newport				
	100(10 × 10)	70 (10 cell)	–	9.63	17.72/strip	62.9	10.74				
(5-AVA) <sub>x</sub> (MA) <sub>1-x</sub> PbI <sub>3</sub>	100(10 × 10)	49 (10 cell)	–	9.1	2	53	10.4	FTO/c-TiO <sub>2</sub> /(m-TiO <sub>2</sub> /m-ZrO <sub>2</sub> /m-Carbon)/perovskite	M	Screen printing and drop casting/1	[127]
(5-AVA) <sub>2</sub> PbI <sub>4</sub> /MAPbI <sub>3</sub>	100(10 × 10)	47.6 (5.95 × 8)	–	7.05	2.247	70.4	11.2	FTO/c-TiO <sub>2</sub> /m-TiO <sub>2</sub> /perovskite/ZrO <sub>2</sub> /Carbon	M	Screen printing and drop casting/1	[128]
MA <sub>0.984</sub> EDA <sub>0.008</sub> PbI <sub>3</sub>	–	1.96 (1.4 × 1.4)	1.04	1.01	20.44	73.4	15.2/CSIRO	FTO/c-TiO <sub>2</sub> /Perovskite/Spiro-OMeTAD/Au	P	Spin coating/1	[129]
(PEI) <sub>2</sub> (MA) <sub>6</sub> Pb <sub>7</sub> I <sub>22</sub>	–	–	2.32	1.08	11.74	63	8.77	ITO/PEDOT:PSS/Perovskite/PC <sub>61</sub> BM/liF/Ag	p	Spin coating/1	[130]

<sup>a)</sup>PCEs are certified by Newport Corp. or Commonwealth Scientific and Industrial Research Organization (CSIRO); <sup>b)</sup>M = mesoporous n-i-p configuration and P = planar n-i-p configuration.

devices.<sup>[6,8,137–139]</sup> To date, only a few new HTMs are successfully applied in large-area PSCs due to their low mobility, poor film morphology, and high cost during the scaling-up process. In this section, we summarize HTMs used in large-area PSCs and further seek inspiration from high-efficiency, nondoped, and low-cost ones applied in small-scale devices in order to realize the rational design of HTMs for scaling-up perovskite photovoltaics.

#### 4.1. Organic Small-Molecule HTMs

Organic small-molecule HTMs are the most widely developed in PSCs owing to their synthetic variety, tunable properties, high purity, and simple solution processing. In this part, we focus on the high-efficiency, low-cost, and dopant-free

small-molecule HTMs, which may be promising for device scaling-up.

##### 4.1.1. High Efficiency and Low-Cost Small-Molecule HTMs

It would be meaningless to list all the small-molecule HTMs because new compounds are reported every month, but only a small fraction shows the promising PCE of above 18%. By now, various small-molecule HTMs with the structural core of benzotrithiophene (BTT),<sup>[140,141]</sup> anthra-tetrathiothiophene (ATT),<sup>[142]</sup> truxene (Trux),<sup>[143–145]</sup> phenylpyrazole (PPyra),<sup>[146]</sup> bipyridine,<sup>[147]</sup> indolo[3,2-b]indole (IDID),<sup>[148]</sup> and paracyclophane<sup>[149]</sup> have successfully achieved high PCE of over 18% in small area PSCs. However complicated synthesis steps increase the

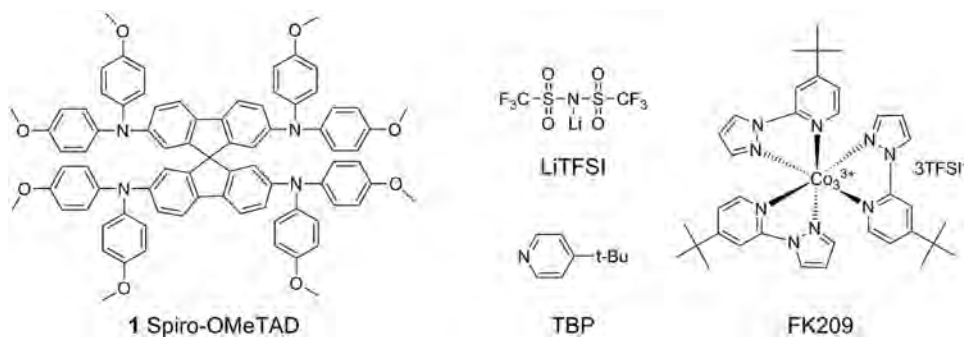


**Figure 17.** Chemical structures of Spiro-OMeTAD and common dopants employed in PSCs.

**Table 4.** High-efficiency and low-cost small-molecule HTMs for PSCs.

No.	HTM	HOMO [eV]	Hole mobility [cm <sup>2</sup> V <sup>-1</sup> s <sup>-1</sup> ]	Conductivity [S cm <sup>-1</sup> ] <sup>a)</sup>	Perovskite	Type <sup>b)</sup>	Dopant <sup>c)</sup>	V <sub>oc</sub> [V]	J <sub>sc</sub> [mA cm <sup>-2</sup> ]	FF [%]	PCE [%] <sup>d)</sup>	Ref. PCE [%] <sup>e)</sup>	Cost [g <sup>-1</sup> ]	Ref.
1	Sprio-OMeTAD	-5.22	5.31 × 10 <sup>-5</sup>	–	(FAPbI <sub>3</sub> ) <sub>x</sub> (MAPbBr <sub>3</sub> ) <sub>1-x</sub>	M	L, T, F	1.16	24.6	73	20.8	–	500\$	[4]
2	X59	-5.15	5.5 × 10 <sup>-5</sup>	1.9 × 10 <sup>-4 a)</sup>	(FAPbI <sub>3</sub> ) <sub>0.85</sub> (MAPbBr <sub>3</sub> ) <sub>0.15</sub>	M	L, T, F	1.13	23.4	73	19.8	20.8	–	[150]
3	X60	–	1.9 × 10 <sup>-4</sup>	1.1 × 10 <sup>-4</sup>	(FAPbI <sub>3</sub> ) <sub>0.85</sub> (MAPbBr <sub>3</sub> ) <sub>0.15</sub>	M	L, T, F	1.14	24.2	71	19.84	–	–	[151]
4	X55	-5.23	6.81 × 10 <sup>-4</sup>	8.43 × 10 <sup>-4</sup>	(FAPbI <sub>3</sub> ) <sub>0.85</sub> (MAPbBr <sub>3</sub> ) <sub>0.15</sub>	M	L, T, F	1.15	23.4	77	20.8	18.8	–	[137]
5	X26	-5.08	4.31 × 10 <sup>-4</sup>	2.79 × 10 <sup>-4</sup>	(FAPbI <sub>3</sub> ) <sub>0.85</sub> (MAPbBr <sub>3</sub> ) <sub>0.15</sub>	M	L, T, F	1.11	24.3	75	20.2	–	–	[138]
6	X36	-5.12	1.97 × 10 <sup>-4</sup>	5.05 × 10 <sup>-4</sup>	(FAPbI <sub>3</sub> ) <sub>0.85</sub> (MAPbBr <sub>3</sub> ) <sub>0.15</sub>	M	L, T, F	1.06	23.7	76	18.9	–	–	[138]
7	XPP	-5.15	1.6 × 10 <sup>-4</sup>	–	MAPbI <sub>3</sub>	P	L	1.12	23.2	75	19.5	5.5	–	[152]
8	KR216	-5.09	7 × 10 <sup>-4</sup>	3.4 × 10 <sup>-5 a)</sup>	(FAPbI <sub>3</sub> ) <sub>0.85</sub> (MAPbBr <sub>3</sub> ) <sub>0.15</sub>	M	L, T, F	1.02	22.3	77	17.8	18.4	11.8\$	[153]
	Biflulo-OMeTAD	-5.2	–	1.6 × 10 <sup>-5</sup>	MAPbI <sub>3</sub>	Slot-die	L, T	1.1	19.7	68	11.7	14.7	–	[154]
9	KR374	-5.06	1.2 × 10 <sup>-6</sup>	–	Cs <sub>0.1</sub> (MA <sub>0.15</sub> FA <sub>0.85</sub> ) <sub>0.9</sub> Pb(I <sub>0.85</sub> Br <sub>0.15</sub> ) <sub>3</sub>	M	L, T, F	1.09	23.2	76	19.26	19.5	–	[155]
10	H11	-5.00	1.58 × 10 <sup>-4</sup>	8.65 × 10 <sup>-5 a)</sup>	(FAPbI <sub>3</sub> ) <sub>0.85</sub> (MAPbBr <sub>3</sub> ) <sub>0.15</sub>	M	L, T, F	1.15	24.2	71	19.8	18.9	–	[156]
11	DM	-5.27	–	–	(FAPbI <sub>3</sub> ) <sub>0.95</sub> (MAPbBr <sub>3</sub> ) <sub>0.05</sub>	M	L, T	1.127	24.92	80.5	22.6/ Newport	21.3	–	[157]
						M/1 cm <sup>2</sup>	L, T	1.125	24.92	74.5	20.9/ Newport	–	–	
12	FDT	-5.16	–	–	(FAPbI <sub>3</sub> ) <sub>0.85</sub> (MAPbBr <sub>3</sub> ) <sub>0.15</sub>	M	L, T, F	1.15	22.7	76	20.2	19.7	60\$	[8]
13	V852	–	4 × 10 <sup>-4</sup>	1.6 × 10 <sup>-5</sup>	(FAPbI <sub>3</sub> ) <sub>0.85</sub> (MAPbBr <sub>3</sub> ) <sub>0.15</sub>	M	L, T, F	1.14	21.7	71	17.77	18.3	–	[164]
14	V859	–	1.3 × 10 <sup>-3</sup>	4.2 × 10 <sup>-5</sup>	(FAPbI <sub>3</sub> ) <sub>0.85</sub> (MAPbBr <sub>3</sub> ) <sub>0.15</sub>	M	L, T, F	1.12	23.3	75	19.47	18.3	15.65\$	[164]
15	V862	–	1 × 10 <sup>-3</sup>	4.9 × 10 <sup>-5</sup>	(FAPbI <sub>3</sub> ) <sub>0.85</sub> (MAPbBr <sub>3</sub> ) <sub>0.15</sub>	M	L, T, F	1.14	22.5	77	19.96	18.3	23.11\$	[164]
16	DDOF	-5.07	–	2.5 × 10 <sup>-5</sup>	(FAPbI <sub>3</sub> ) <sub>0.85</sub> (MAPbBr <sub>3</sub> ) <sub>0.15</sub>	M	L, T, F	1.1	22.4	79	19.4	18.8	–	[160]
17	Z26	-5.16	1.34 × 10 <sup>-4</sup>	3.5 × 10 <sup>-4</sup>	(FAPbI <sub>3</sub> ) <sub>0.85</sub> (MAPbBr <sub>3</sub> ) <sub>0.15</sub>	M	L, T, F	1.13	23.6	75	20.1	20.6	35.57\$	[139]
18	V950	–	5.2 × 10 <sup>-4</sup>	–	(FAPbI <sub>3</sub> ) <sub>0.85</sub> (MAPbBr <sub>3</sub> ) <sub>0.15</sub>	M	L, T, F	1.07	22.5	74	17.8	18.6	5.58\$	[166]
19	HL-2	-5.27	2.26 × 10 <sup>-4</sup>	–	(FAPbI <sub>3</sub> ) <sub>0.85</sub> (MAPbBr <sub>3</sub> ) <sub>0.15</sub>	M	L, T, F	1.09	21.3	79	18.34	–	–	[167]
20	SGT-405	-5.26	1.8 × 10 <sup>-4</sup>	–	MAPbCl <sub>3-x</sub> I <sub>x</sub>	M	L, T, F	1.05	22.9	79	18.87	17.7	29.65€	[168]

<sup>a)</sup>Conductivity with dopant; <sup>b)</sup>M = mesoporous n-i-p configuration and P = planar n-i-p configuration; <sup>c)</sup>L = LiTFSI, T = t-BP, F = FK209; <sup>d)</sup>PCEs are certified by Newport Corp.; <sup>e)</sup>Ref. PCE represents efficiency of reference device.

product cost and hamper the scaling-up of perovskite photovoltaics. Therefore, numerous research efforts have been made in molecular design and synthesis route selection to pursue both high efficiency and low cost. The summarized data are listed in **Table 4**.

**HTMs with Spiro-Type Core:** Using Spiro-OMeTAD (1) as a reference, many research groups have focused on spiro-type core compounds to pursue high PCE through slight structural modification and reduce costs by changing the synthetic route. A low-cost spiro[fluorene-9,9'-xanthene] (SFX)-based X59 (*N',N',N'',N''*-tetrakis(4-methoxyphenyl) spiro[fluorene-9,9'-xanthene]2,7-diamine (2) and X60 (*N2,N2,N2',N2',N7,N7,N7',N7'*-octakis(4-methoxyphenyl) spiro[fluorene-9,9'-xanthene]-2,2',7,7'-tetraamine (3) were designed and synthesized with only two synthetic steps.<sup>[150,151]</sup> The SFX core was constructed by a one-pot approach with commercially available raw materials. PSCs based on the two HTMs exhibited a high efficiency of 19.8%. X55 (*N2,N7*-bis(4-methoxyphenyl)-*N2,N7*-di(spiro[fluorene-9,9'-xanthene]-2-yl) spiro[fluorene-9,9'-xanthene]-2,7-diamine (4) constructed of three SFX units had a 3D structure and achieved a PCE of 20.8%.<sup>[137]</sup> This material showed a much deeper HOMO level

and higher hole mobility, as well as better thermal stability than those of Spiro-OMeTAD. More importantly, the estimated synthetic cost of the SFX unit was around 30 times lower than that of spirobifluorene (SBF), which makes SFX-based molecules suitable for large-scale industrial production. Very recently, X26 (*N2*-(2-(bis(4-methoxyphenyl)amino)spiro[fluorene-9,9'-xanthene]-7-yl)-*N2,N7,N7'*-tris(4-methoxyphenyl)spiro[fluorene-9,9'-xanthene]-2,7-diamine (5) and X36 (6) were reported by the same group,<sup>[138]</sup> which could be seen as triphenylamine-linked dimers of X59. These two HTMs achieved the remarkable PCEs of 20.2% and 18.9%, respectively. XPP (*N2,N2,N7,N7'*-tetrakis(4-methoxyphenyl)-3',6'-bis(pyridin-4-ylmethoxy) spiro[fluorene-9,9'-xanthene]-2,7-diamine (7) was obtained by connecting two *para*-position substituted pyridines on the SFX core unit, which showed a high PCE of 19.5% in mix ion-based planer PSCs without TBP as additive.<sup>[152]</sup> Due to the steric hindrance effect of the molecular geometry, both nitrogen atoms in the pyridine units of XPP could easily form a strong chemical bonding with the Pb atoms of perovskites. The good device performance was attributed to the strong binding correlation and enhanced coupling between the XPP/perovskite interface, which passivated surface traps through the pyridine



substitution and further reduced the charge recombination. HTM **8** (2,2',7,7'-tetrakis(*N,N*-di-*p*-methoxyphenylamine)-9,9'-bifluorenylidene, coded as KR216,<sup>[153]</sup> and Bifluo-OMeTAD<sup>[154]</sup>) with bifluorenylidene core was synthesized by two simple steps with inexpensive precursor. Though the small-area devices by spin-coating process showed an unsatisfactory efficiency of 17.8%, this molecule exhibited an excellent film-forming property and outperformed Spiro-OMeTAD in the slot die-coated devices due to suppressed crystallization during the fabrication process. The fully slot die-coated devices achieved a PCE of over 14%, which was one of the highest efficiencies reported for a printed PSC. The family of bifluorenylidene-based HTMs was extended by introducing six-membered O/S bridged rings into the core with a simple synthesis route. O/S bridged rings were selected to enhance the intramolecularly overcrowded dipolar aromatic "push-pull" system for achieving high charge-carrier mobility. The S-bridged KR374 (9-{2,7-bis[bis(4-methoxyphenyl)amino]-9H-fluorenylidene}-*N*<sub>2</sub>,*N*<sub>2</sub>,*N*<sub>7</sub>,*N*<sub>7</sub>-tetrakis(4-methoxyphenyl)-9H-thioxanthene-2,7-diamine, **9**)<sup>[155]</sup> obtained a 19.2% efficiency PSC. By replacing the C=C linkage of bifluorenylidene by C–C linkage, H11 (*N*<sub>2</sub>,*N*<sub>2</sub>,*N*<sub>2</sub>,*N*<sub>2</sub>,*N*<sub>7</sub>,*N*<sub>7</sub>,*N*<sub>7</sub>,*N*<sub>7</sub>-octakis(4-methoxyphenyl)-9H,9'H-[9,9'-bifluorene]-2,2',7,7'-tetraamine (**10**)<sup>[156]</sup> was synthesized with a facile two-step synthesis process and exhibited a promising PCE of 19.8%. The good performance of devices originated from an efficient hole extraction at the perovskite/H11 interface and an effective hole transport in the H11 film. The above research results demonstrate a simple strategy by using SFX and bifluorenylidene cores to design HTMs for high-efficiency and low-cost PSCs, which is urgent for the scaling-up

and manufacturing of PSCs. Very recently, a fluorene-terminated HTM DM ((*N*<sub>2</sub>,*N*<sub>2</sub>',*N*<sub>7</sub>,*N*<sub>7</sub>'-tetrakis(9,9-dimethyl-9H-fluorene-2-yl)-*N*<sub>2</sub>,*N*<sub>2</sub>',*N*<sub>7</sub>,*N*<sub>7</sub>'-tetrakis(4-methoxyphenyl)-9,9'-spirobifluorene]-2,2',7,7'-tetraamine) (**11**) with spiro-core was successfully synthesized.<sup>[157]</sup> The champion small-area PSC with DM as an HTM showed a certified PCE of 22.6% and the large device with an aperture area of ≈1 cm<sup>2</sup> reached a certified PCE of 20.9%. Moreover, the PSC with DM exhibited good long-term stability for 500 h under heat stress of 60 °C, whereas the control device with Spiro-OMeTAD degraded rapidly after only 50 h. High efficiency and good long-term stability of the PSCs based on DM enabled the material to have commercial potential. However, for Spiro-cored HTMs, another main issue to realizing large-area commercial devices is how to reduce material cost. The chemical structure and simple synthesis route of molecules discussed above are shown in **Figures 18** and **19**.

*HTMs with Other Central Cores:* Small-molecule HTMs based on other central cores have been facilely synthesized and used in the state-of-art PSCs, such as acridine (ACR),<sup>[158]</sup> phenothiazine,<sup>[159]</sup> thiophene,<sup>[139]</sup> bithiophene,<sup>[160]</sup> biphenyl,<sup>[161]</sup> fluorine,<sup>[162–164]</sup> fluorine-dithiophene,<sup>[8]</sup> and carbazole.<sup>[165–168]</sup> The flagship molecules and their synthesis routes are summarized in **Figures 20** and **21**. PSCs based on fluorine-dithiophene cored FDT (2',7'-bis(bis(4-methoxyphenyl)amino)spiro[cyclopenta[2,1-b:3,4-b']dithiophene-4,9'-fluorene] (**12**) achieved a remarkable PCE of 20.2%, which compared favorably with control devices with Spiro-OMeTAD.<sup>[8]</sup> Furthermore, the lab-synthesis cost of FDT was estimated about 60 \$ g<sup>-1</sup>, which was much lower than that of Spiro-OMeTAD. V852 (9,9',9''-(benzene-1,3,5-triyltrimethylidene)

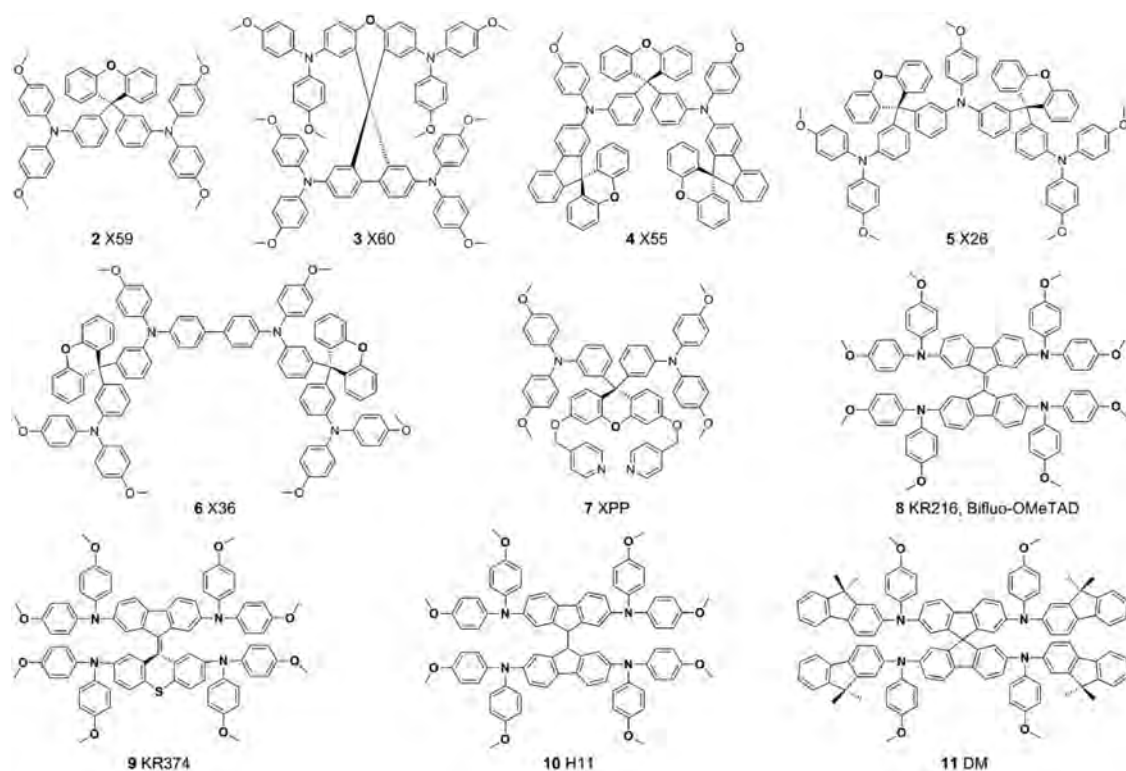


**Figure 18.** Chemical structures of high-efficiency and low-cost small-molecule HTMs based on Spiro-type core.

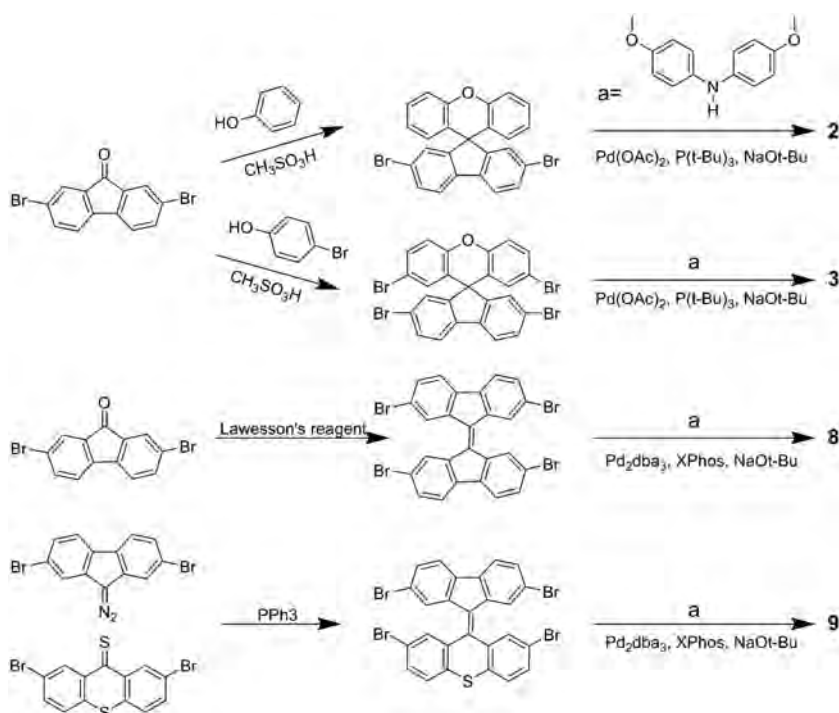


Figure 19. Low-cost synthesis routes of HTMs based on Spiro-type core.

tris[*N,N,N',N'*-tetrakis(4-methoxyphenyl)-9H-fluorene-2,7-diamine], (13)), V859 (9,9'-(benzene-1,2-diylidimethylidene) bis[*N,N,N',N'*-tetrakis(4-methoxyphenyl)-9H-fluorene-2,7-diamine] (14)) and V862 (9,9'-(thiene-2,5-diylidimethylidene)

bis[*N,N,N',N'*-tetrakis(4-methoxyphenyl)-9H-fluorene-2,7-diamine] (15)) based on methoxydiphenylamine-substituted fluorene fragments were obtained by two-step synthesis and the PSCs showed a PCE of up to 19.96%.<sup>[164]</sup> The facile synthesis route and relatively inexpensive raw materials achieved up to fivefold cost reduction of the final product compared to Spiro-OMeTAD, which enabled these materials to be potential candidates. Dimethoxydiphenylamine-substituted dispiro-oxepine derivative of DDOF (2,2',7,7'-tetrakis(*N,N'*-di-4-methoxyphenylamine)dispiro[fluorene-9,4'-dithieno[3,2-c:2',3'-e]oxepine-6',9''-fluorene] (16)) was obtained with a facile synthetic route and the PSCs exhibited a high PCE of 19.4%.<sup>[160]</sup> Very recently, the thiophene cored Z26 (4,4'-((1*E*,1'*E*)-(3,4-dimethoxythiophene-2,5-diyl)bis(ethene-2,1-diyl))bis(*N,N*-bis(4-methoxyphenyl)aniline) (17)) was facile synthesized by introducing double bonds into the molecule and exhibited an impressive PCE of 20.1%.<sup>[139]</sup> Z26 could form a film with the homogeneous surface and high hole mobility compared to the control molecule without double bonds. Carbazole as a commercial-

ized raw reagent is widely employed as the electron donor or core fragment of HTMs.<sup>[166,169–177]</sup> A simple carbazole-based conjugated enamine V950 (9-ethyl-3-{*N,N*-bis[2,2-bis(4-methoxyphenyl)vinyl]amino}-9H-carbazole (18)) was synthesized

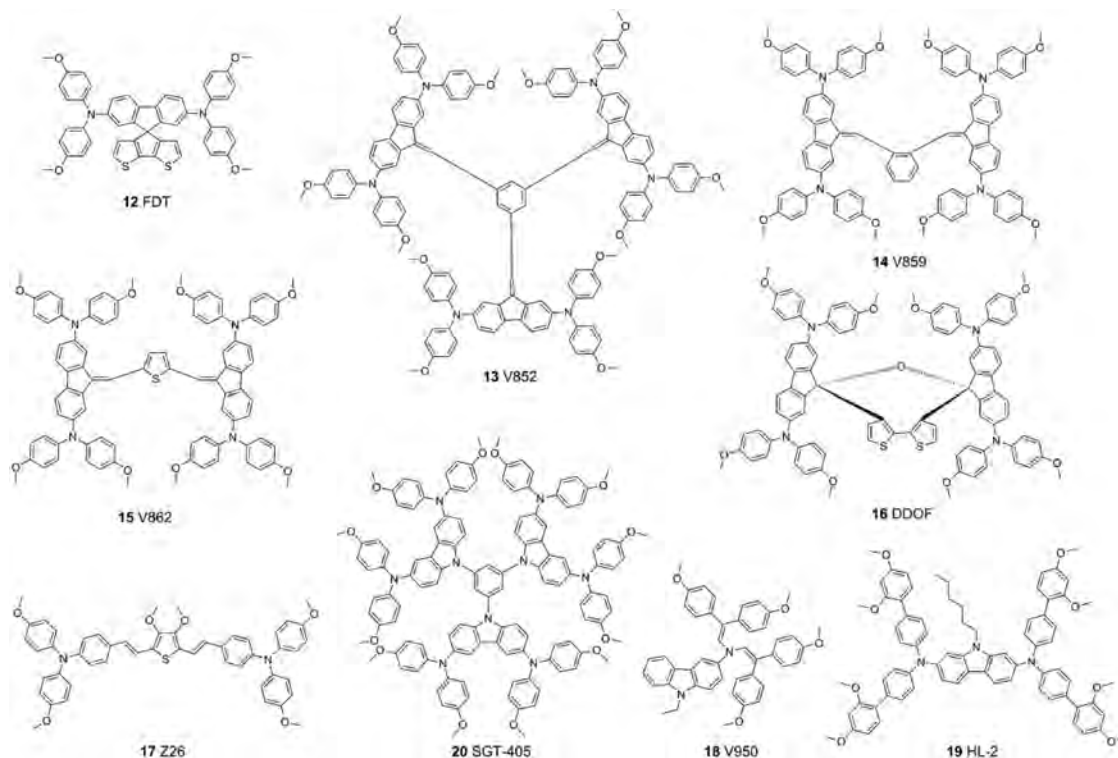
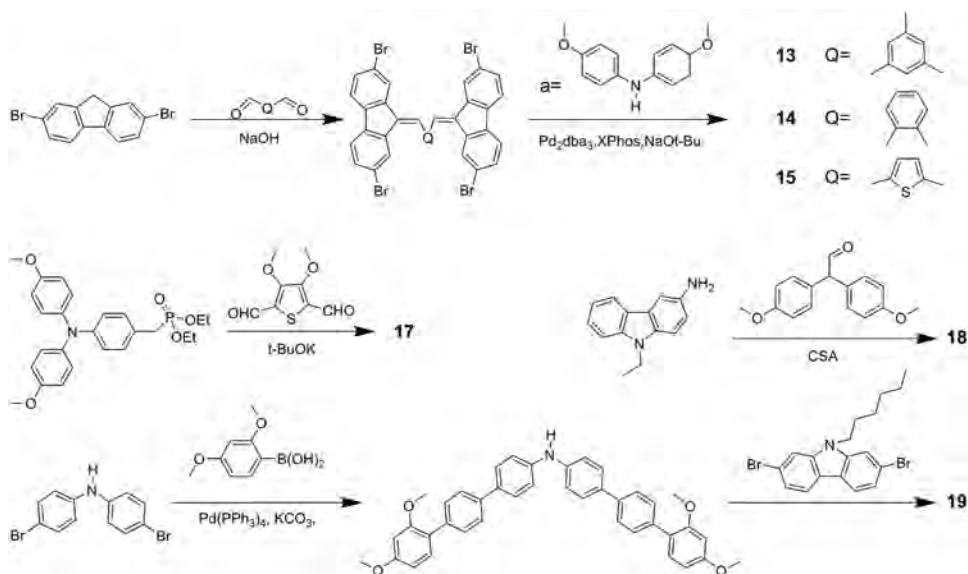


Figure 20. Chemical structures of high-efficiency and low-cost small-molecule HTMs based on other central core.



**Figure 21.** Low-cost synthesis routes of HTMs based on other central core.

from relatively cheap starting reagents via one extremely simple route without expensive catalysts, column chromatography and sublimation purification.<sup>[166]</sup> The cost of the final product was reduced by more than an order of magnitude compared to that of Spiro-OMeTAD. The V950 based PSCs showed a PCE close to 18%. HL-2 (**19**) employing 9-hexyl-9H-carbazole as the conjugation core was easily synthesized.<sup>[167]</sup> This material could form a compact film without pin-holes, and obtained PSCs exhibiting a PCE of 18.34%. Carbazole-based SGT-405 (**20**) with a starburst structure was obtained from commercialized reagents via three-step synthesis,<sup>[168]</sup> and achieved high-efficiency PSCs with a PCE of 18.87%. This star-shaped SGT-450 exhibited significantly increased glass transition temperature ( $T_g$ ) of 192.7 °C, improved film-forming property, reduced hole reorganization energy and enhanced hole mobility compared to Spiro-OMeTAD. Due to the facile synthesis route and the attracting efficiency, the above HTMs show the potential to replace Spiro-OMeTAD, but dopants are used, which is considered to be one of the factors affecting the stability of perovskite devices.

#### 4.1.2. Dopant-Free Small-Molecule HTMs

Small-molecule materials generally suffer from low hole mobility due to the weak intermolecular interactions. Chemical doping is an important method to enhance device efficiency by tuning the energy levels and increasing the conductivity, as well as reducing Ohmic losses in HTM layers and injection barriers at the interface with the anode.<sup>[178,179]</sup> Traditionally, HTMs are heavily doped with p-type dopants, such as LiTFSI, FK209,<sup>[4,8,150,151]</sup> and 2,3,5,6-tetrafluoro-7,7,8,8-tetracyanoquinodimethane ( $F_4$ TCNQ),<sup>[180]</sup> to provide the necessary conductivity when used in PSCs. However, chemical dopants can deteriorate the device efficiency and increase the fabrication cost. Recently, developing dopant-free HTMs with high hole mobility has attracted wide interest of many researchers. Nevertheless, only a few PSCs based on dopant-free HTM show

the PCEs of over 16%. In this part, we summarize the dopant-free HTMs with high PCEs (>16%) and discuss the molecular design strategy to find a better understanding in relationship between the molecular structure and device performance. The summarized data are listed in **Table 5**.

*Dopant-Free Small-Molecule HTMs with Donor–Acceptor (D–A) Type Structure:* Organic D–A HTMs, also widely known as push–pull systems, always generate a molecular dipole between donor and acceptor parts. Due to strong intramolecular charge transfer, these molecules show high hole mobility, which make them promising candidates as dopant-free HTMs. Most of the electron acceptors involve substituents featuring –CN groups as well as electron deficient heterocyclic compounds, e.g., triazines, benzoxadiazole or benzothiadiazoles, while the donors are most commonly constructed by aromatic units. D–A molecules may adopt several arrangements including linear structure (D–A) and tripodal structure ((D)<sub>3</sub>–A or D–(A)<sub>3</sub>). The properties of D–A molecules can be engineered by changing the donor or acceptor moieties. **Figure 22** shows the dopant-free small-molecule HTMs with D–A type structure.

A linear D–A small-molecule HTM DERDTS-TBDT (**21**) was designed by using the coplanar and strong electron-donating 4,4-bis(2-ethylhexyl)-4H-silolo[3,2-b:4,5-b']dithiophene (DTS) unit, which showed the matched energy level with perovskite and high hole mobility.<sup>[181]</sup> The PCE of PSCs based on this D–A HTMs was 16.2% without any dopant. A dopant-free DFBT(DTS-FBTTh<sub>2</sub>)<sub>2</sub> (7,7'-((5,6-difluorobenzo[c][1,2,5]thiadiazole-4,7-diyl)bis(4,4-bis(2-ethylhexyl)-4H-silolo[3,2-b:4,5-b']bithiophene-6,2-diyl))bis(6-fluoro-4-(5'-hexyl-[2,2-bithiophen]-5-yl)benzo[c][1,2,5]thiadiazole) (**22**)) based on a D'–A–D–A–D' conjugated structure by using fluorobenzothiadiazole (FBT) and DTS blocks was obtained, achieving a good PCE of 17.3%.<sup>[182]</sup> FBT pairing with DTS effectively stabilized the quinoidal character of the molecule and enhanced its planar conformation, which were desirable properties for charge transport. BTPA-TCNE (**23**) was synthesized via a simple reaction between a triphenylamine-based Michler's base and



**Table 5.** Dopant-free small-molecule HTMs for high-efficiency PSCs.

No.	HTM	HOMO [eV]	Hole mobility [cm <sup>2</sup> V <sup>-1</sup> s <sup>-1</sup> ]	Perovskite	Type <sup>a)</sup>	V <sub>oc</sub> [V]	J <sub>sc</sub> [mA cm <sup>-2</sup> ]	FF [%]	PCE [%]	Ref. PCE [%] <sup>b)</sup>	Cost [\$ g <sup>-1</sup> ]	Ref.
21	DERDTS-TBDT	-5.20	1.0 × 10 <sup>-4</sup>	MAPbCl <sub>3-x</sub> I <sub>x</sub>	P	1.05	21.20	72.8	16.20	5.40	-	[181]
22	DFBT(DTS-FBTTTh <sub>2</sub> ) <sub>2</sub>	-5.27	1.78 × 10 <sup>-4</sup>	MAPbI <sub>3</sub>	P	1.10	20.70	76.0	17.30	17.40	-	[182]
23	BTPA-TCNE	-5.35	3.14 × 10 <sup>-5</sup>	MAPbI <sub>3</sub>	P	1.04	20.84	78.2	16.94	4.96	-	[183]
24	BTF3	-5.19	6.36 × 10 <sup>-5</sup>	(FAPbI <sub>3</sub> ) <sub>0.85</sub> (MAPbBr <sub>3</sub> ) <sub>0.15</sub>	P	1.08	20.40	74.3	16.34	9.33	53.1	[184]
25	BTF4	-5.02	1.17 × 10 <sup>-4</sup>	(FAPbI <sub>3</sub> ) <sub>0.85</sub> (MAPbBr <sub>3</sub> ) <sub>0.15</sub>	I	1.06	22.50	75.6	18.03	9.33		
					P	1.03	19.30	75.9	15.09	16.42	62.8	[184]
26	KR321	-5.24	2.6 × 10 <sup>-4</sup>	(FAPbI <sub>3</sub> ) <sub>0.85</sub> (MAPbBr <sub>3</sub> ) <sub>0.15</sub>	M	1.13	21.70	78.0	19.03	19.01	-	[145]
27	FA-CN	-5.30	1.2 × 10 <sup>-4</sup>	(FAPbI <sub>3</sub> ) <sub>0.85</sub> (MAPbBr <sub>3</sub> ) <sub>0.15</sub>	M	1.13	21.71	77	18.9	7.5	-	[185]
28	CMO	-4.78	1.4 × 10 <sup>-4</sup>	MAPbI <sub>3</sub>	P	0.93	25.19	67.9	15.92	16.7	-	[186]
29	TPAC3M	-4.96	1.1 × 10 <sup>-5</sup>	MAPbI <sub>3</sub>	I	1.00	22.79	78.0	17.54	12.60	-	[187]
30	IDTT-TPA	-5.00	6.46 × 10 <sup>-4</sup>	MAPbI <sub>3</sub>	P	1.05	21.25	70.5	15.70	7.80	-	[188]
31	mDPA-DBTP	-5.31	6.34 × 10 <sup>-4</sup>	MAPbI <sub>3</sub>	P	1.12	21.13	76.0	18.09	15.45	-	[189]
32	Z34	-5.14	7.46 × 10 <sup>-4</sup>	MAPbI <sub>3</sub>	M	1.06	21.25	70.0	16.10	16.70	66	[190]
33	Z1011	-5.21	8.49 × 10 <sup>-4</sup>	MAPbI <sub>3</sub>	M	1.10	20.52	70.0	16.30	9.60	-	[191]
34	Trux-OMeTAD	-5.28	3.6 × 10 <sup>-3</sup>	MAPbI <sub>3</sub>	I	1.02	23.4	79.0	18.6	16.0	-	[144]
35	TCP-OH	-5.47	5.85 × 10 <sup>-6</sup>	(FAPbI <sub>3</sub> ) <sub>0.85</sub> (MAPbBr <sub>3</sub> ) <sub>0.15</sub>	M	1.07	23.15	66.7	16.97	13.26	-	[192]
36	TPP-SMeTAD	-5.18	-	MAPbI <sub>3</sub>	I	1.07	20.15	77.0	16.60	-	-	[193]
37	3,6 BCz-OMeTAD	-5.11	1.13 × 10 <sup>-4</sup>	Cs <sub>0.05</sub> FA <sub>0.79</sub> MA <sub>0.16</sub> PbI <sub>2.49</sub> Br <sub>0.51</sub>	M	1.121	21.34	70.0	17.00	11.20	8.55	[194]
38	2,7 BCz-OMeTAD	-5.15	0.95 × 10 <sup>-4</sup>	Cs <sub>0.05</sub> FA <sub>0.79</sub> MA <sub>0.16</sub> PbI <sub>2.49</sub> Br <sub>0.51</sub>	M	1.09	22.38	72.5	17.60	11.20	14	

<sup>a)</sup>M = mesoporous n-i-p configuration, P = planar n-i-p configuration, and I = inverted p-i-n configuration; <sup>b)</sup>Ref. PCE represents efficiency of reference device.

tetracyanoethylene, and showed an antiparallel molecular packing in its crystalline state, which compensated its overall molecular dipole moment to facilitate charge transport.<sup>[183]</sup> BTPA-TCNE was employed as a dopant-free HTM in the n-i-p PSCs to realize a PCE of about 17%. Very recently, two D-A HTMs BTF3 (3,8-bis(di-*p*-tolylamino)fluoranthene-4,5-dicarbonitrile, **24**) and BTF4 (3,8-bis(bis(4-methoxyphenyl)amino)fluoranthene-4,5-dicarbonitrile (**25**)) were obtained.<sup>[184]</sup> The 2,3-dicyano-fluoranthene was prepared through a simple Die-Alder reaction between dibenzofulvene and tetracyanoethylene. This building block not only endowed the resulting molecules with suitable energy levels, but also enabled highly ordered molecule packing in solid state, both of which could facilitate hole extraction and transport. With the dopant-free BTF 4, impressive efficiencies of 18.03% and 17.01% were achieved for conventional n-i-p and inverted p-i-n PSCs, respectively. Star-shaped HTMs combine the advantages of both small molecules, i.e., well-defined structure, and polymers, e.g., good thermal and photochemical stability. Dopant-free D- $\pi$ -(A)<sub>3</sub> HTM KR321 (2,2',2''-((5,10,15-trihexyl-10,15-dihydro-5H-diindolo[3,2-a:3',2'-c]carbazole-3,8,13-triyl)tris(3,3''-dihexyl-[2,2':5',2''-terthiophene]-5'',5'-diyl))tris(metha-nylylidene))trimalonitrile, **26**) featured a planar triazatruxene central core as donor, inducing thiophene-based multiple conjugated arms as  $\pi$  linker and malononitrile as acceptor.<sup>[145]</sup> Due to strong intermolecular interaction, these molecules showed high hole mobility, minimizing Ohmic losses of charge transport in HTM layer. The particular molecule-stacking feature resulted in an exciting

PCE over 19% without any dopant, which outperformed most of the other dopant-free HTMs reported to date. Another star-shaped D- $\pi$ -(A)<sub>3</sub> molecule FA-CN (**27**) was reported by the same group, which incorporated a rigid quinolizino acridine as the central donor unit, alkyl-substituted terthiophene as a conjugated bridge, and malononitrile as an electron-acceptor part.<sup>[185]</sup> The quinolizino acridine enhanced the  $\pi$ - $\pi$  stacking of the molecules and thereby facilitated the hole transport, exhibiting a high PCE of about 19%. Although D-A type dopant-free HTMs achieved high-efficiency PSCs, the most of them still required multistep synthesis and purification, which have significantly raised production costs and limited potential large-scale applications.

*Dopant-Free Small-Molecule HTMs with Donor-Donor (D-D)-Type Structure:* Generally, D-D-type HTMs are designed by connecting electron donor moieties with  $\pi$  linkers, leading to the suitable HOMO level to perovskites. D-D molecules may adopt several arrangements including linear (D- $\pi$ -D) type, tripodal ((D)<sub>3</sub>- $\pi$ ) type, and quadrupolar ((D)<sub>4</sub>- $\pi$ ) type. **Figure 23** shows the dopant-free small molecular HTMs with D-D-type structure.

A linear structure HTM CMO (**28**) with carbazole core was synthesized by one simple step and the PSCs showed a PCE almost 16%.<sup>[186]</sup> By tuning the number of methoxy groups in the arylamine moiety, the device efficiency for TPAC3M (**29**) with three methoxy groups was increased from 13.9% to 17.54% compared to the molecular without methoxy unit.<sup>[187]</sup> Methoxy groups could serve as a Lewis base to passivate the defect sites, which improved the charge extraction and

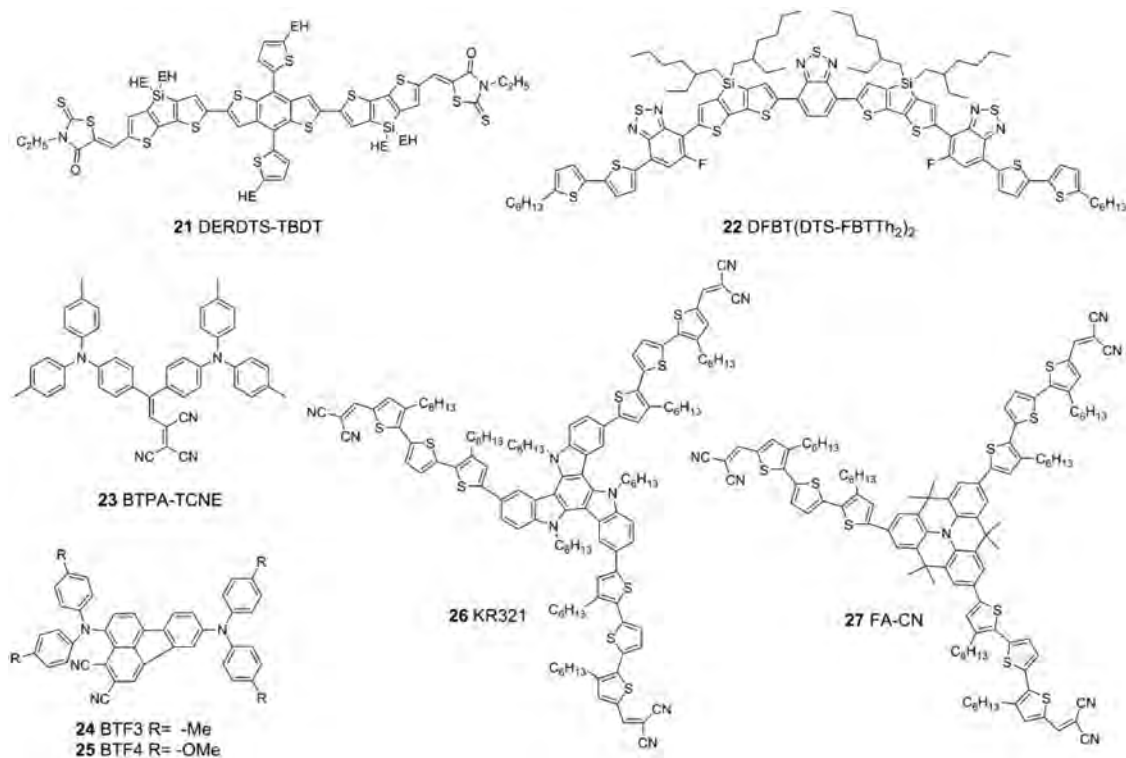


**Figure 22.** Dopant-free small-molecule HTMs with D–A type structure.

recombination of PSCs. A dopant-free, planar PSC with IDTT-TPA (**30**) was fabricated and exhibited a PCE of about 16%.<sup>[188]</sup> The molecular contained an extended fused-ring indacenodithienothiophene (IDTT) core, resulting in strong  $\pi$ – $\pi$  interactions and a high hole mobility. mDPA–DBTP (**31**) containing strong electron-donating moieties, e.g., di(1-benzothieno)[3,2-b:2',3'-d]pyrrole (DBTP) and triphenylamine, was synthesized.<sup>[189]</sup> The fused ring of DBTP enhanced the backbone planarity and intermolecular  $\pi$ – $\pi$  stacking, which endowed mDPA–DBTP an excellent hole-transport characteristic. PSCs based on dopant-free mDPA–DBTP displayed a PCE of 18.09% with negligible hysteresis. D– $\pi$ –D– $\pi$ –D type Z34 (4-((*E*)-4-(bis(4-methoxyphenyl)amino)styryl)-*N*-(4-((*E*)-4-(bis(4-methoxyphenyl)amino)styryl)phenyl)-*N*-(4-methoxyphenyl)aniline (**32**)) was synthesized with Wittig reaction from cheap starting materials, and the estimated synthesis cost of Z34 was 66\$ g<sup>-1</sup>.<sup>[190]</sup> The PSCs based on dopant-free Z34 achieved a PCE of 16.1%. The good performance of this material was attributed to the introduction of symmetrical donor units linked with double bonds, which increased the hole mobility and matched its energy levels with perovskites. A similar structure of Z1011 (4-((*E*)-4-(bis(4-(*E*)-4-(dibutylamino)styryl)phenyl)amino)styryl)-*N*-(4-((*E*)-4-(bis(4-(*E*)-4-(dibutylamino)styryl)phenyl)amino)styryl)phenyl)-*N*-phenylaniline (**33**)) was reported by the same group,<sup>[191]</sup> which exhibited a high hole mobility owing to the larger  $\pi$  conjugated units. A PCE of 16.3% was obtained without doping chemical additives. Star-shaped Trux-OMeTAD (3,8,13-tri(di-4-methoxyphenylamino)-5,5,10,10,15,15-Hex(1-hexyl)10,15-dihydro-5H-diindeno[1,2- $\alpha$ :1',2'- $\zeta$ ]fluorene (**34**)) consisting of C<sub>3h</sub> Truxene core with three arylamine groups adapted a planar,

rigid and fully conjugated molecular geometry,<sup>[144]</sup> which gave this HTM high hole mobility and suitable energy-level matched with perovskites. The PSCs showed a high PCE of 18.6% with minimal hysteresis employing dopant-free HTMs. C3-symmetric TCP-OH (**35**) with phenol core was synthesized and a PCE about 17% was obtained. used in PSCs.<sup>[192]</sup> TPP-SMeTAD (4',5'-bis(4-(bis(4-(methylthio)phenyl)amino)phenyl)-3',6'-dimethyl-*N*4,*N*4,*N*4'' (**36**)) containing a tetraphenyl core and arylamine groups with the terminal substituents of methyl-sulfanyl group was designed and synthesized.<sup>[193]</sup> TPP-SMeTAD exhibited a deep HOMO and strong interaction with perovskites, leading to efficient charge extraction and surface traps passivation. PSCs based on TPP-SMeTAD without any dopants exhibited a good PCE of 16.6%. Very recently, two novel 3,6 BCz-OMeTAD (**37**) and 2,7 BCz-OMeTAD (**38**) based on two connected carbazole units were prepared by a simple synthetic route from very cheap starting materials (**Figure 24**), which brought out the lab costs of only 8.55\$ g<sup>-1</sup> and 14.00\$ g<sup>-1</sup>, respectively.<sup>[194]</sup> Due to their good film-forming property and matched energy level, HTM **37** and HTM **38** were successfully applied in 1 cm<sup>2</sup> area PSCs and achieved the PCEs of up to 17.0% and 17.6%, respectively. Furthermore, the unencapsulated PSCs based on the latter retained 90% of its initial PCE after aging 2000 h stored in an ambient condition.

## 4.2. Polymeric HTMs

Conjugated polymers have garnered particular interest for realizing of low-cost, large-area PSCs owing to their fusibility,

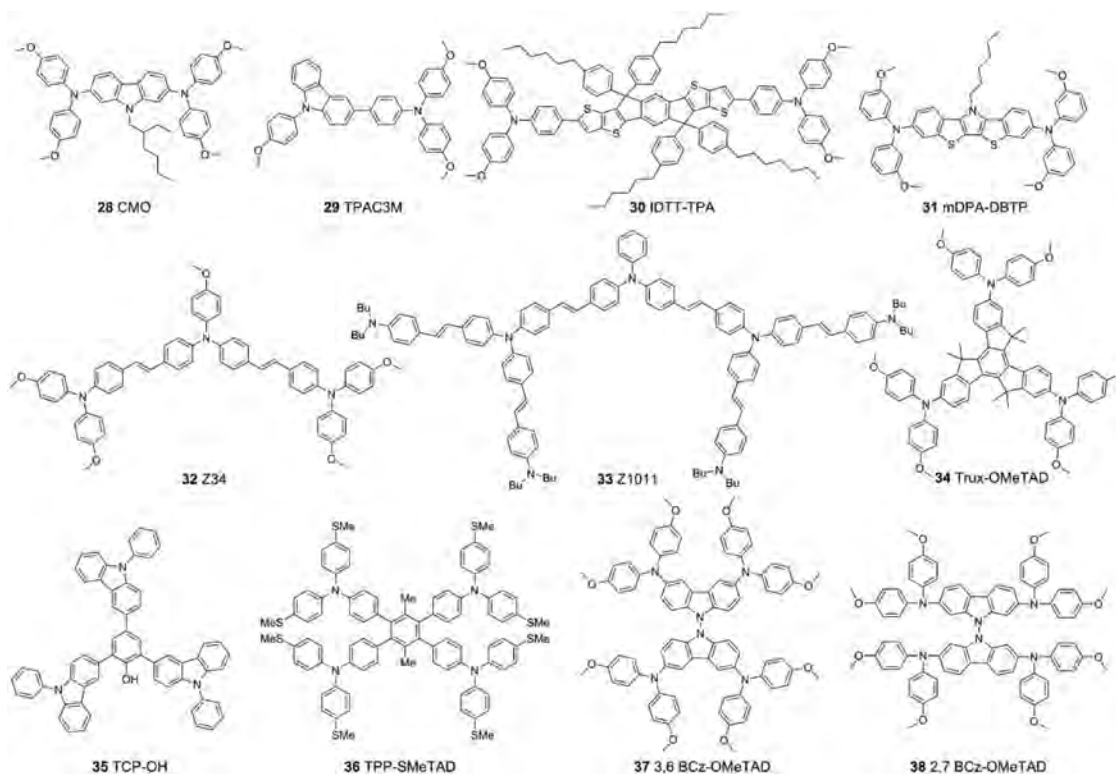


Figure 23. Dopant-free small-molecule HTMs with D–D-type structure.

good solubility, processability and high hole mobility. Poly-[bis(4-phenyl)(2,4,6-trimethylphenyl)amine] (PTAA (39)) was the first polymer applied in PSCs,<sup>[195]</sup> and to date the device efficiency has achieved above 22.1% due to its high hole mobility of  $1 \times 10^{-2}$  to  $1 \times 10^{-3} \text{ cm}^2 \text{ V}^{-1} \text{ s}^{-1}$ .<sup>[30]</sup> Nevertheless, the product cost of PTAA is extremely expensive (about 2000 \$  $\text{g}^{-1}$ ), making it impossible to produce in large-area PSCs. In this section, we concentrated on the cost-effective (Figure 25) or

dopant-free polymers (Figure 27) as the HTMs in large-area PSCs.

PEDOT:PSS (40) was one of the commercial polymeric HTMs widely used in PSCs due to its good film-forming property, no absorption in visible region and high work function (WF).<sup>[196]</sup> By now, numerous reports have focused on large-area p–i–n-type PSCs using PEDOT:PSS as the HTL.<sup>[33,34,39,66,72,85–87,90,99,100,130]</sup> The specific data of some PEDOT:PSS-based large-area PSCs can be found in Tables 13. In 2015, Back et al. found that perovskite films showed a low surface coverage on PEDOT:PSS substrate via blade-coating technique.<sup>[87]</sup> For achieving high-quality perovskite films, the PEDOT:PSS layer was modified by adding poly(4-styrenesulfonic acid) (PSSH), which could form the electrostatic interaction of the sulfonyl functional groups in PEDOT:PSS with perovskite precursor ions. The 15 mm  $\times$  40 mm area perovskite film on the modified PEDOT:PSS showed good uniformity and surface coverage with high crystallinity (Figure 26A). Finally, a printed PSC with a PCE of 10.15% was obtained via blade coating. In another work, a nanocellular PEDOT:PSS (NC-PEDOT:PSS) film doped with polystyrene was prepared by a low-temperature process.<sup>[197]</sup> The NC-PEDOT:PSS remarkably increased the light harvesting of the device, while also acting as a scaffold to afford a bendable perovskite

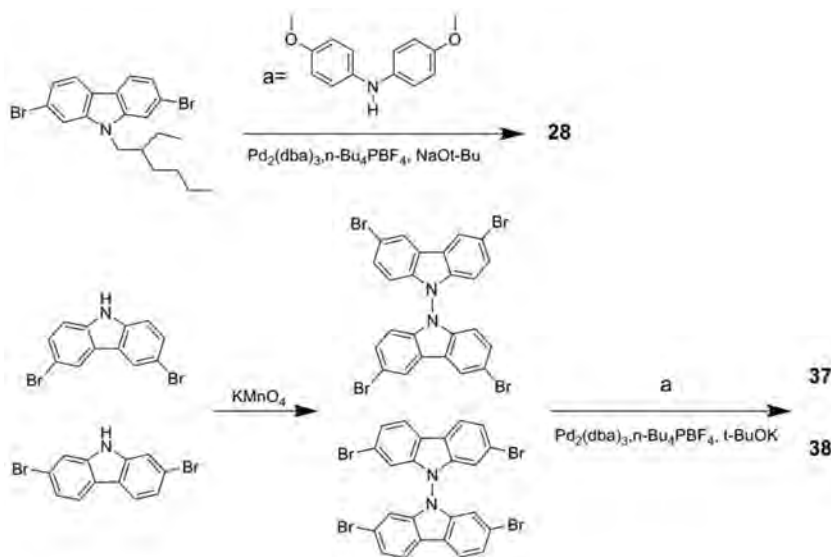
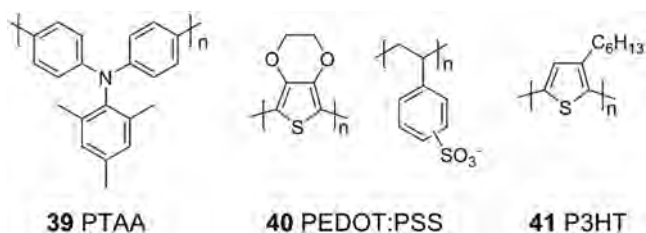


Figure 24. Simple synthesis routes of HTMs 28, 37 and 38.





**Figure 25.** Traditional commercial polymeric HTMs for PSCs.

film with high crystallinity. In addition, polystyrene doping and nanocellular structure were helpful to the balance of charge-carrier transport in planar PSCs. Flexible PSCs with 1 cm<sup>2</sup> area achieved an average efficiency up to 12.32%, which could be assembled into a wearable solar-power source (Figure 26B). Poly(3-hexylthiophene) (P3HT (41)) is another commercial conducting polymer and has been successfully applied in organic photovoltaics due to its low synthesis cost.<sup>[198]</sup> Although P3HT exhibits the highest hole mobility of 0.1 cm<sup>2</sup> V<sup>-1</sup> s<sup>-1</sup> among the conjugated polymers,<sup>[199]</sup> it still needs to be doped with chemical additives to get better device efficiency.<sup>[200–202]</sup> By using Li-doped P3HT nanofibrils as the HTL, flexible PSCs with an active area of 1 cm<sup>2</sup> showed a PCE of 13%.

Besides the commercial conducting polymers mentioned above, various polymeric HTMs facing on PSCs have been developed by researchers (Figure 27). However, most doped<sup>[203–207]</sup> and nondoped<sup>[208–213]</sup> polymers exhibit low device efficiencies in PSC devices, which are below 16% and even lower than 10%, respectively.<sup>[79,214–220]</sup> A series of dopant-free polymeric HTMs with high efficiency in state-of-the-art PSC devices were reported by Park's group. RCP (42) based on benzodithiophene (BDT) and benzothiadiazole (BT) units showed high-efficiency and stable PSCs (17.3% for over 1400 h at 75% relative humidity).<sup>[221]</sup> This polymer showed a high hole mobility of  $3.09 \times 10^{-3}$  cm<sup>2</sup> V<sup>-1</sup> s<sup>-1</sup>. A asymmetric D–A polymer asy-PBTBDT (43) was synthesized.<sup>[222]</sup> The hole mobility of this dopant-free polymer was  $1.13 \times 10^{-3}$  cm<sup>2</sup> V<sup>-1</sup> s<sup>-1</sup>,

which is nearly identical to that of doped Sprio-OMeTAD ( $1.8 \times 10^{-3}$  cm<sup>2</sup> V<sup>-1</sup> s<sup>-1</sup>). Moreover, asy-PBTBDT could be processed with a green solvent and the PSCs based on this dopant-free material exhibited a good photovoltaic performance with a PCE of 18.3% and a high long-term stability. By introducing tetraethylene glycol, the BDT–BT-based D–π–A polymer PTEG (44) showed good solubility and well contact with perovskites.<sup>[223]</sup> The PSCs based on this nondoped polymer showed an impressive PCE of 19.8%. Recently, a series of D–A copolymers based on carbazole and BT units, e.g., PCDTBT (poly[*N*-9'-heptadecanyl-2,7-carbazole-alt-5,5-(4',7'-di-2-thienyl-2',1',3'-benzothiadiazole)] (45)), PCDTBT1 (poly[9-(heptadecan-9-yl)-9H-carbazole-2,7-diyl-alt-(5,6-bis(methoxy)-4,7-di(thiophen-2-yl)benzo[c][1,2,5]thiadiazole-5,5-diyl)] (46)) and PCDTBT8 (poly[9-(heptadecan-9-yl)-9H-carbazole-2,7-diyl-alt-(5,6-bis(octyloxy)-4,7-di(thiophen-2-yl)benzo[c][1,2,5]thiadiazole-5,5-diyl)] (47)), were synthesized as dopant-free HTMs, which exhibited high device performance in PSCs.<sup>[224]</sup> The synergistic passivation effect of thiophene units and methoxy side chains in PCDTBT1 could effectively reduce trap sites of the perovskite film, achieving a maximum PCE of 19.1%. In late 2017, Hou et al. reported a common strategy for scalable polymer HTMs to increase the device performance by adding tantalum-doped tungsten oxide (Ta-WO<sub>x</sub>) in conjugated polymers.<sup>[225]</sup> Ta-WO<sub>x</sub>/conjugated polymer bilayers could reduce the charge-transport barrier between the electrode and hole transport layer. PSCs based on the Ta-WO<sub>x</sub> interface layer achieved a PCE of up to 21.2% and retained 95% of its initial efficiency after light-soaking for 1000 h. Further research highlighted the importance of energy level alignment between the HOMO level of HTMs and the valence band (VB) of perovskites, which not only reduced the hysteresis originated from charge accumulation at the interfaces, but also prevented the degradation of HTM resulted from ion migration.<sup>[226]</sup> PVCz-OMeDAD (48) featuring a nonconjugated polyvinyl main chain and carbazole-based side chains could be easily obtained by the free-radical polymerization of vinyl monomers without

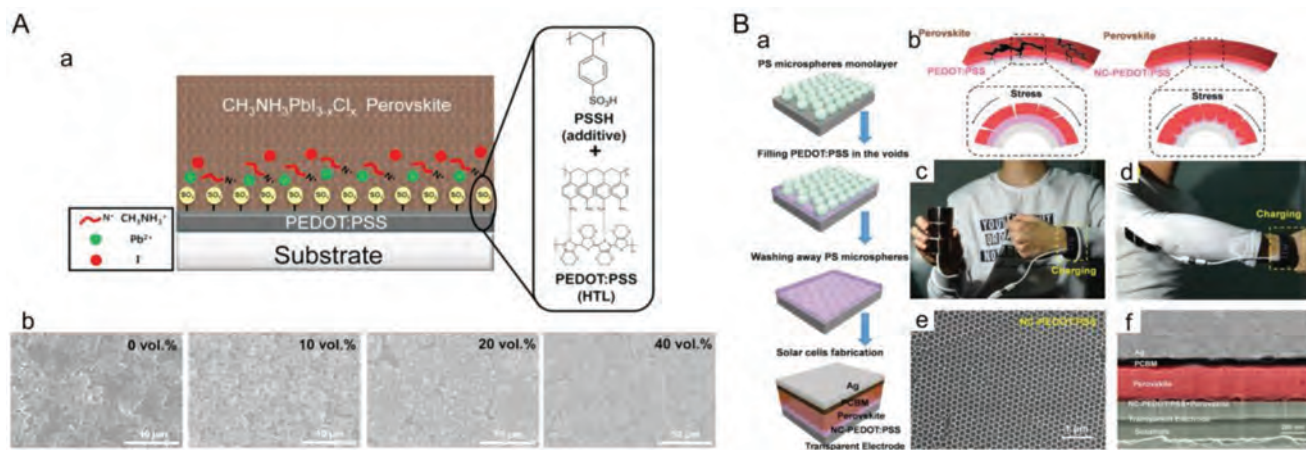


**Figure 26.** A) Schematic of the perovskite layer on the ITO/modified PEDOT:PSS substrate and chemical structures of PEDOT:PSS and PSSH a). b) SEM images of the blade-coated perovskite layer on PEDOT:PSS and modified PEDOT:PSS (10, 20, and 40 vol%) substrates. A) Reproduced with permission.<sup>[87]</sup> Copyright 2016, Elsevier. B) Fabrication procedure for the nanocellular PEDOT:PSS scaffold and perovskite solar cells a). b) Scheme of stresses release by the NC-PEDOT:PSS structure. c, d) Photographs of flexible solar cell modules as a wearable power source. e) SEM image of the NC-PEDOT:PSS layer. f) SEM cross-sectional image of perovskite solar cells with NC-PEDOT:PSS layer. B) Reproduced with permission.<sup>[197]</sup> Copyright 2017, Wiley-VCH.

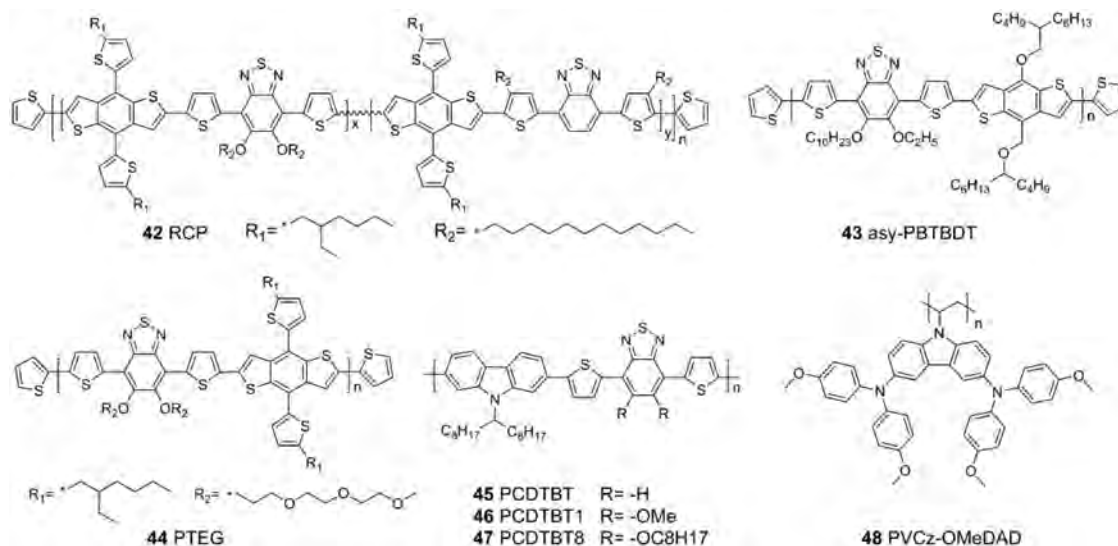


**Figure 27.** High-efficiency dopant-free polymeric HTMs for PSCs.

noble-metal catalysts.<sup>[227]</sup> The PSCs based on this dopant-free polymer showed a PCE up to 16%. This work provide a design idea of nonconjugated polymer HTMs for future low-cost large-scale PSCs application. The summarized data of polymeric HTMs are listed in **Table 6**.

Conjugated polymers have also been used in some researches to improve the property of perovskite films. Bi et al. reported a polymer-templated nucleation and crystal growth of perovskite film and the PSCs certified a PCE of 21.02% by using poly(methyl methacrylate) (PMMA) in antisolvent.<sup>[7]</sup>

However, the insulated PMMA could block carrier transfer. By using the same antisolvent processing, p-type polymer PBDB-T (poly[(2,6-(4,8-bis(5-(2-ethylhexyl)thiophen-2-yl)-benzo[1,2-b:4,5-b']dithiophene))-alt-(5,5-(1',3'-di-2-thienyl-5',7'-bis(2-ethylhexyl)benzo[1',2'-c:4',5'-c'] dithiophene-4,8-dione))]) instead of PMMA was applied in PSCs, leading to a high efficiency close to 20% and an excellent device stability.<sup>[228]</sup> This hydrophobic p-type polymer not only passivated the trap states of perovskite films due to forming Lewis adducts between lead and oxygen atom of PBDB-T, but also infiltrated into the grain boundaries

**Table 6.** Polymeric and organometallic HTMs for high-efficiency PSCs.

No.	HTM <sup>a)</sup>	HOMO [eV]	Hole mobility [cm <sup>2</sup> V <sup>-1</sup> s <sup>-1</sup> ]	Conductivity [S cm <sup>-1</sup> ]	Perovskite	Type <sup>b)</sup>	Dopant <sup>c)</sup>	V <sub>oc</sub> [V]	J <sub>sc</sub> [mA cm <sup>-2</sup> ]	FF [%]	PCE [%]	Ref. PCE [%] <sup>d)</sup>	Cost [\$ g <sup>-1</sup> ]	Ref.
39	PTAA	-5.2	10 <sup>-3</sup> to 10 <sup>-2</sup>	-	MAPbI <sub>3</sub>	M	L, T	1.1	25	80.3	22.1	-	2500-3000	[30]
40	NC-PEDOT:PSS	-5.3	8.3 × 10 <sup>-5</sup>	-	MAPbI <sub>3</sub>	I	-	1.08	22.47	81	19.66	-	-	[197]
					MAPbI <sub>3</sub>	I/1 cm <sup>2</sup>	-	1.04	15.79	75	12.32	-	-	
41	P3HT	-5.05	0.1	2.04 × 10 <sup>-4</sup>	MAPbI <sub>3</sub>	P/1 cm <sup>2</sup> Flexible	L, T	0.904	22.25	66.9	13.45	-	700-850	[201]
42	RCP	-5.41	3.09 × 10 <sup>-3</sup>	-	MAPbI <sub>3</sub>	P	-	1.08	21.9	75.0	17.3	3.8	-	[221]
43	asy-PBTBDT	-5.36	1.13 × 10 <sup>-3</sup>	-	cs-perovskite	M	-	1.11	22.4	73.2	18.3	9.9	-	[222]
44	PTEG	-5.4	1.64 × 10 <sup>-3</sup>	-	cs-perovskite	P	-	1.14	22.5	77.0	19.8	-	-	[223]
45	PCDTBT	-5.35	-	-	MAPbI <sub>3</sub>	P	-	1.05	21.6	72.34	17.1	19.4	-	[224]
46	PCDTBT1	-5.38	-	-	MAPbI <sub>4</sub>	P	-	1.1	21.8	77.63	19.1	19.4	-	[224]
47	PCDTBT8	-5.4	-	-	MAPbI <sub>5</sub>	P	-	1.02	21.3	67.31	15.4	19.4	-	[224]
48	PVCz-OMeDAD	-5.24	3.44 × 10 <sup>-4</sup>	-	FA <sub>0.85</sub> MA <sub>0.15</sub> Pb(I <sub>0.85</sub> Br <sub>0.15</sub> ) <sub>3</sub>	M	-	1.085	21.96	67.5	16.09	9.62	-	[227]
49	CuPc	-5.20	10 <sup>-3</sup> to 10 <sup>-2</sup>	-	(FAPbI <sub>3</sub> ) <sub>0.85</sub> (MAPbBr <sub>3</sub> ) <sub>0.15</sub>	M	-	1.07	22.6	77.5	18.8	-	-	[235]
50	HT-ZnPc	-5.19	-	8 × 10 <sup>-5</sup>	(FAPbI <sub>3</sub> ) <sub>0.85</sub> (MAPbBr <sub>3</sub> ) <sub>0.15</sub>	M	-	1.05	20.28	80.3	17.1	19.1 <sup>d)</sup>	-	[236]
51	NiPc-(OBU) <sub>8</sub> /V <sub>2</sub> O <sub>5</sub>	-5.06	1.9 × 10 <sup>-4</sup>	1.18 × 10 <sup>-4</sup>	(FAPbI <sub>3</sub> ) <sub>0.85</sub> (MAPbBr <sub>3</sub> ) <sub>0.15</sub>	M	-	1.08	23.1	73.4	18.3	18.2 <sup>d)</sup>	-	[237]

<sup>a)</sup>The specific data of some PEDOT:PSS-based large-area PSCs are displayed in Tables 13<sup>[33,34,39,66,72,85-87,90,99,100,130]</sup>; <sup>b)</sup>M = mesoporous n-i-p configuration, P = planar n-i-p configuration, and I = inverted p-i-n configuration; <sup>c)</sup>L = LiTFSI, T = t-BP; <sup>d)</sup>Ref. PCE represents efficiency of reference device.

of perovskites to enhance charge transfer and keep the perovskite films from moisture. In another work, series of conjugated polymers were chosen to dope into MAPbI<sub>3</sub> and PSCs based on p-type J71 polymer exhibited a PCE of 19.19%.<sup>[229]</sup> The polymer existed among perovskite grains, which could improve charge transport and passivate the traps of perovskite crystals. In Lee et al.'s work, an amphiphatic conjugated polyelectrolyte layer was applied as an interfacial layer to modify the surface polarity of HTM poly[(2,6-(4,8-bis(5-(2-ethylhexyl)thiophene-2-yl)-benzo[1,2-b:4,5-b']dithiophene))-alt-(5,5-(1',3'-di-2-thienyl-5',7'-bis(2-ethylhexyl)benzo[1',2'-c:4',5'-c']dithiophene-4,8-dione))] (PTPD), and a uniform perovskite film on large-area of about 18.4 cm<sup>2</sup> was fabricated.<sup>[230]</sup> Planar PSCs with an active area of 1 cm<sup>2</sup> achieved a PCE of up to 17%.

### 4.3. Organometallic HTMs

Copper phthalocyanine (CuPc (**49**)) has already been used as a p-type semiconductor and attracted attention because of its high hole mobility (10<sup>-3</sup> to 10<sup>-2</sup> cm<sup>2</sup> V<sup>-1</sup> s<sup>-1</sup>), thermal and chemical stability, and low cost, which make the CuPc a promising HTM candidate for PSCs.<sup>[231,232]</sup> The first PSC based on CuPc suffered very low fill factor (0.40) and showed a PCE of only 5%.<sup>[233]</sup> By using nanorod-liked CuPc as the dopant-free HTM and printed carbon as the cathode, the device efficiency increased to 16.1%.<sup>[234]</sup> In late 2017, a breakthrough work of doped CuPc was reported, in which the PSCs achieved a high PCE of 18.8% and maintained 97% of their initial efficiency after thermal annealing at 85 °C for more than 1000 h.<sup>[235]</sup> The short nanorod-liked CuPc formed an intimate contact with both the MAPbI<sub>3</sub> crystal grains and the carbon counter electrode, thereby inducing a dramatically enhancement in hole extraction and charge recombination suppression. An easily accessible zinc phthalocyanines (HT-ZnPc (**50**)) was employed as HTMs in mixed-ion PSCs, reaching a PCE up to 17.5%.<sup>[236]</sup> An organic-inorganic integrated HTL composed of the solution-processable nickel phthalocyanine (NiPc) abbreviated NiPc-(OBu)<sub>8</sub> (**51**) and vanadium(V) oxide (V<sub>2</sub>O<sub>5</sub>) was successfully incorporated into PSCs and showed an impressive average PCE of 17.6%.<sup>[237]</sup> The chemical structures of the organometallic HTMs are shown in **Figure 28** and the summarized data are listed in Table 6.

### 4.4. Inorganic HTMs

In contrast to organic HTMs, inorganic p-type semiconductors represent a promising but less explored alternative for large-scale industrial applications due to their intrinsically high stability, high hole mobility, and low-cost fabrication. However, to date, only a few examples of inorganic HTMs are present in the literature due to the limited choice of suitable materials. Moreover, inorganic HTMs are usually used in p-i-n-type PSCs to avoid the degradation of the perovskite layer by the polar solvents. In this part, we will review several inorganic HTMs in PSCs, which are suitable for large-scale fabrication. The summarized data of inorganic HTMs are listed in **Table 7**.

#### 4.4.1. Nickel Oxide (NiO<sub>x</sub>)

NiO<sub>x</sub> has been demonstrated to be a promising inorganic HTM due to its p-type characteristics with a wide bandgap, high optical transmittance, chemical stability, and an appropriate valence band alignment with various photoactive layers.<sup>[238,239]</sup> NiO<sub>x</sub> has been successfully applied in several types of PSCs such as inverted mesoscopic PSCs,<sup>[240–243]</sup> inverted planar PSCs,<sup>[244–254]</sup> and mesoporous carbon electrode based PSCs.<sup>[255–258]</sup> Furthermore, various methods were employed to prepare NiO<sub>x</sub> film, such as spin coating,<sup>[242,245,246,248,250–253]</sup> spray pyrolysis,<sup>[240]</sup> atomic layer deposition,<sup>[254]</sup> sputtering,<sup>[243,244]</sup> pulsed laser deposition,<sup>[241]</sup> and screen printing.<sup>[255,257,258]</sup> In 2015, a NiO based small-area PSCs with PCE of 17.3% was reported by Seok and co-workers.<sup>[241]</sup> The nanostructured NiO film prepared by pulsed laser deposition enhanced the device performance due to the suppressed charge recombination. In 2015, a breakthrough work on NiO-based large-area PSCs was reported by Han and co-workers.<sup>[51]</sup> By using a heavily p-doped Ni<sub>x</sub>Mg<sub>1-x</sub>LiO as the HTL, PSCs with an active area of over 1 cm<sup>2</sup> showed a certified PCE of 15.0%. The conductivity of the doped Ni<sub>x</sub>Mg<sub>1-x</sub>LiO film was 12 times greater than that of the undoped NiO reference. The Ni<sub>x</sub>Mg<sub>1-x</sub>LiO-based HTM showed excellent Ohmic contact with both the FTO and perovskite due to the decrease of the barrier height by the staircase energy-level alignment. Moreover, the p-doping increased the electrical conductivity of NiO films, and reduced the charge transport resistance, thus improving hole extraction. Han's group

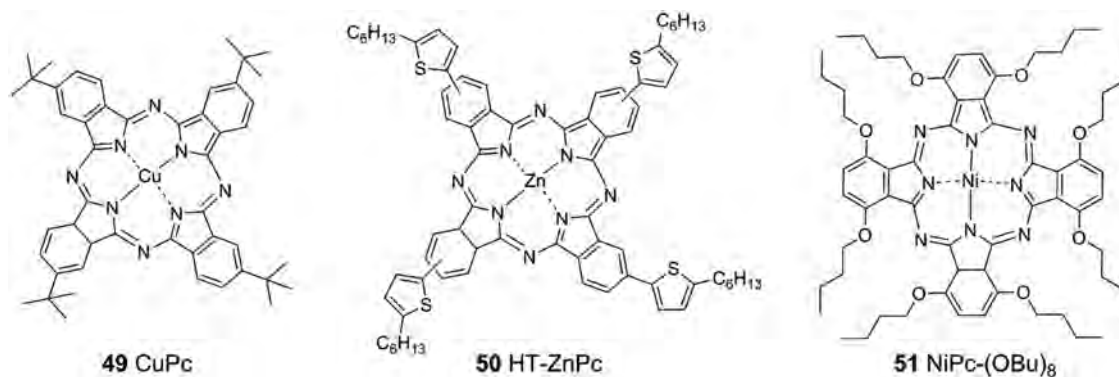


**Figure 28.** High-efficiency organometallic HTMs for PSCs.



**Table 7.** Inorganic HTMs for PSCs.

No.	HTM <sup>a)</sup>	HOMO [eV]	Hole mobility [cm <sup>2</sup> V <sup>-1</sup> s <sup>-1</sup> ]	Conductivity [S cm <sup>-1</sup> ]	Perovskite	Type <sup>b)</sup>	Deposition method	V <sub>oc</sub> [V]	J <sub>sc</sub> [mA cm <sup>-2</sup> ]	FF [%]	PCE [%]	Ref. PCE [%] <sup>c)</sup>	Cost [\$ g <sup>-1</sup> ]	Ref.
52	NiO	-5.2	–	1.66 × 10 <sup>-4</sup>	MAPbI <sub>3</sub>	I	Pulsed laser deposition	1.06	20.2	81.3	17.3	–	10–20	[241]
	Ni <sub>x</sub> Mg <sub>1-x</sub> LiO	-5.25	–	2.32 × 10 <sup>-3</sup>	MAPbI <sub>3</sub>	I/1 cm <sup>2</sup>	Spray printing	1.072	20.21	74.8	16.2	–		[51]
	NiO	-5.2	–	–	MAPbI <sub>3</sub>	M/all print	Screen printing	0.915	21.62	76	15.03	–		[255]
53	CuSCN	-5.3	0.01-0.1	–	MAPbI <sub>3</sub>	M	Doctor blading	1.016	19.7	62.0	12.4	–	3–4	[263]
	CuSCN	-5.3	0.01-0.1	–	(FAPbI <sub>3</sub> ) <sub>0.85</sub> (MAPbBr <sub>3</sub> ) <sub>0.15</sub>	M	Spin coating	1.1	21.8	69	16.6	19.65		[264]
	CuSCN	-5.3	0.01-0.1	–	(FAPbI <sub>3</sub> ) <sub>0.85</sub> (MAPbBr <sub>3</sub> ) <sub>0.15</sub>	M	Spin coating	1.04	23.1	75.3	18.0	18.4		[265]
	CuSCN	-5.3	1.2 × 10 <sup>-3</sup>	–	CsFAMAPbI <sub>3-x</sub> Br <sub>x</sub>	M	Drop casting	1.112	23.24	78.2	20.4	20.8		[266]
54	CuI	–	9.3	–	MAPbI <sub>3</sub>	M	Drop casting	0.55	17.8	62	6	–	1–10	[269]
	CuI	-5.1	9.3	–	MAPbI <sub>3</sub>	I	Spin coating	1.04	21.06	62	13.58	13.28		[270]
	CuI	–	9.3	–	MAPbI <sub>3</sub>	M	Spray deposition	1.03	22.78	75	17.6	–		[271]
	CuI	-5.12	9.3	–	MAPbI <sub>3</sub>	M/1 cm <sup>2</sup>	Thermal evaporation	–	–	47	8.3	–		[272]
55	Cu <sub>2</sub> O	-5.4	100	–	MAPbI <sub>3</sub>	I	Spin coating	1.07	16.52	75.51	13.35	–	10–20	[273]
	Cu <sub>2</sub> O	-5.4	100	–	MAPbI <sub>3</sub>	I	Spin coating	0.99	23.2	74	17.1	–		[275]
56	Co <sub>3</sub> O <sub>4</sub>	-5.3	–	–	MAPbI <sub>3</sub>	M/70 cm <sup>2</sup>	Screen printing	0.88	21.64	60	13.27	–	–	[277]

<sup>a)</sup>The specific data of some NiO-based large-area PSCs are displayed in Tables 1 and 2<sup>[55,58,69,103]</sup>; <sup>b)</sup>M = mesoporous n–i–p configuration and I = inverted p–i–n configuration; <sup>c)</sup>Ref. PCE represents efficiency of reference device.

reported a series of high-efficiency large-area PSCs using the NiO-based HTLs, which were prepared by a spray pyrolysis process. PSCs with 1 cm<sup>2</sup> active-area exhibited remarkable PCEs of 17.6%,<sup>[58]</sup> 18.21%,<sup>[103]</sup> and 19.19%,<sup>[55]</sup> respectively. A larger PSC with an active area of 5 cm<sup>2</sup> achieved a PCE of 15.5%.<sup>[69]</sup> The specific data of these PSCs are displayed in Tables 1 and 2. A fully printed PSC based on the mesoscopic TiO<sub>2</sub>/Al<sub>2</sub>O<sub>3</sub>/NiO/carbon framework was obtained and showed a PCE of up to 15.03%.<sup>[255]</sup> This all-printable strategy contributed to the realization for low cost, large-scale, and high-efficiency PSCs.

#### 4.4.2. Copper Thiocyanate (CuSCN)

CuSCN was another widely used inorganic p-type semiconductor owing to its no absorption in the visible and near infrared region, high hole mobility of 0.01–0.1 cm<sup>2</sup> V<sup>-1</sup> s<sup>-1</sup> and good chemical stability.<sup>[259–262]</sup> More importantly, CuSCN can form films with solution processing method at low temperature, making it suitable for large-scale even flexible substrates. In 2014, an n–i–p-type PSC based on CuSCN was reported by Qin et al., which showed a PCE of 12.4%.<sup>[263]</sup> In combination with mixed-ion perovskites, the PCE of PSCs using CuSCN as the HTM increased to 16.6%.<sup>[264]</sup> The device efficiency quickly reached 18%, and the low-temperature solution-processed CuSCN exhibited a highly stable crystalline structure even at high temperatures.<sup>[265]</sup> In late 2017, Arora et al. reported CuSCN-based PSCs with stabilized PCEs of over 20%.<sup>[266]</sup> The highly conformal and compact CuSCN films were obtained by a rapid solvent removal method, which was helpful to the fast charge extraction and transport. By optimizing the interface of CuSCN/Au, the device retained more than 95% of its initial

PCE after aging at a maximum power point for 1000 h under the light-soaking (1 sun) and thermal (60 °C) dual stress. High PCE values of CuSCN-based PSCs, combined with remarkably operational and thermal stability, offer the potential for large-scale deployment.

#### 4.4.3. Cuprous Iodide (CuI) and Cuprous Oxide (Cu<sub>2</sub>O)

Other low-cost Cu-based inorganic HTMs such as CuI and Cu<sub>2</sub>O are also successfully employed in PSCs owing to their high hole mobility of 9.3 cm<sup>2</sup> V<sup>-1</sup> s<sup>-1</sup> for CuI and 100 cm<sup>2</sup> V<sup>-1</sup> s<sup>-1</sup> for Cu<sub>2</sub>O, respectively.<sup>[267,268]</sup> In late 2013, CuI was first used as the inorganic HTM in PSCs, showing a PCE of 6%.<sup>[269]</sup> In 2015, Chen et al. reported an inverted planar PSC used a solution-processed CuI as HTM, which exhibited a PCE of 13.58%.<sup>[270]</sup> Nevertheless, for n–i–p-type PSCs, the polar solvent to dissolve CuI for the typical spin-coating process can damage the perovskite film. Recently, by using a facile spray deposition method to prepare CuI film, PSCs exhibited a PCE of 17.6% and an outstanding device stability.<sup>[271]</sup> In another work, a novel approach in the simultaneous deposition of CuI and Cu was reported.<sup>[272]</sup> The Cu layer was directly deposited on the perovskite layer prepared by two-step method, and the excessive MAI on the perovskite surface could act as an iodine provider to product the CuI between the Cu metal contact and perovskite layer. A 1 cm<sup>2</sup> area PSC exhibited a PCE of 8.3%. Researchers have also made attempts to make Cu<sub>2</sub>O as an HTM in PSCs.<sup>[268,273–276]</sup> A facile low-temperature method was used to prepare Cu<sub>2</sub>O films via in situ conversion of CuI in aqueous NaOH solution.<sup>[273]</sup> CuO film was made by heating Cu<sub>2</sub>O film in air. The PSCs with CuO and Cu<sub>2</sub>O as HTMs achieved the PCEs of 13.35% and 12.16%,

respectively. In another work, a high-efficiency inverted planar PSCs based on a solution processed  $\text{CuO}_x$  HTL exhibited a PCE of up to 17.1%.<sup>[275]</sup>

#### 4.4.4. Other Inorganic HTMs

Very recently, a screen printed thin layer of p-type inorganic spinel  $\text{Co}_3\text{O}_4$  in carbon-based PSCs was reported.<sup>[277]</sup> The device exhibited a PCE of 13.27% and long-term stability of up to 2500 h under ambient conditions. Furthermore, a monolithic perovskite module was demonstrated with an active area of 70  $\text{cm}^2$  and showed a PCE of more than 11% with almost no hysteresis. The results indicated that  $\text{Co}_3\text{O}_4$  was a promising HTM for efficient and stable large-area PSCs.

## 5. Electron Transport Materials

For high-performance PSCs, electron transport materials are as important as perovskite materials and HTMs, which can effectively help the electron extraction and transport from the perovskite layer to the cathode. A suitable ETM for large-area PSCs must possess the features as below. 1) Compatible conduction band and valence band with perovskites can facilitate electron extraction and block holes to avoid the charge recombination. 2) High electron mobility can ensure the effective and rapid electron transport. 3) Wide bandgap can guarantee high transparency for high light-harvesting by the photoactive layer. 4) Low-temperature processing can simplify the production procedures and reduce the costs, realizing the all-low-temperature mass manufacturing of PSCs.

Generally, ETMs used in PSCs can be divided into inorganic and organic parts. Inorganic ETMs are commonly n-type metal oxides and have been widely investigated, such as  $\text{TiO}_2$ , stannic oxide ( $\text{SnO}_2$ ), zinc oxide ( $\text{ZnO}$ ), and so on. The metal oxide ETMs are usually used in n-i-p-type PSCs with planar or mesoporous structure because the high temperature of sintering process can damage the perovskite layer. Other types of ETMs are n-type organic semiconductors, such as fullerene ( $\text{C}_{60}$ ) and derivatives (i.e., [6,6]-phenyl- $\text{C}_{61}$ -butyric acid methyl ester (PCBM)). These types of ETMs are widely used in inverted p-i-n-type PSCs due to their suitable energy-level alignment, decent electron mobility, and low-temperature solution process. In the part of the review, we introduce the development of ETMs on large-area perovskite solar cells in recent years.

### 5.1. Inorganic ETMs

#### 5.1.1. $\text{TiO}_2$

In terms of material choice,  $\text{TiO}_2$  remains the most popular inorganic ETL in large-area PSCs, resulting from its inherent transparency, tunable electronic properties, matched energy level with perovskite, and low cost. To date, numerous deposition techniques were developed to fabricate a good compact or mesoporous  $\text{TiO}_2$  layers for the high-efficiency devices.

**Compact  $\text{TiO}_2$ :** The compact  $\text{TiO}_2$  layer is essential for both planar and mesoporous PSCs to ensure highly efficient electron extraction and transport, as well as hole blocking. The method employed in c- $\text{TiO}_2$  fabrication could directly impact the morphology, thickness and roughness of the ETM film, thus influencing the device performance.<sup>[278]</sup> The technique commonly used in large-area c- $\text{TiO}_2$  fabrication is spray pyrolysis deposition (SPD).<sup>[30,52,53,59,61,62,65,80,97,102,114,129]</sup> Compare to the traditional spin-coating method, SPD technique can not only form a denser  $\text{TiO}_2$  film, but also reduce the material losses and deposition time, thereby leading to low-cost production. Generally, small-area PSCs and most of PSMs in lab fabrication are implemented by manual spray pyrolysis. The uniformity of the deposited films depends on the inclination angle of the sprayer, the spraying height, the pressure of the carrier gas, the speed of the sprayer, and the time between two spraying sequences. The reliability of this technique is less mentioned on small-area devices, but it is a urgent problem for large-area devices. However, this issue can be solved by using automation technology in mass production of PSCs.

One issue that has to be considered for c- $\text{TiO}_2$  deposited by SPD and spin coating is the high-temperature (400–500 °C) post treatment for nanocrystalline formation, which can be a hindrance in producing the simple and low-cost mass PSCs.<sup>[68]</sup> Therefore, low-temperature processing techniques of electron transport layers are urgently required for manufacturing large-scale PSCs. Magnetron sputtering,<sup>[279,280]</sup> atomic layer deposition (ALD),<sup>[84,281]</sup> and electron beam (e-beam) induced evaporation<sup>[82,88,282]</sup> were developed to deposit c- $\text{TiO}_2$  at relatively low temperature. Yang et al. reported a process to fabricate a very dense amorphous  $\text{TiO}_2$  layer for PSCs by using magnetron sputtering at room temperature.<sup>[280]</sup> The flexible PSC based this  $\text{TiO}_2$  film showed a good electron injection and a PCE of 15.07%. Giacomo et al. fabricated a flexible large-area PSM by using a compact ALD  $\text{TiO}_2$  layer.<sup>[84]</sup> They found that the ALD film exhibited efficient hole-blocking behavior, which was approved by the extremely low reverse current density of 0.004  $\text{mA cm}^{-2}$  at -1 V in dark (**Figure 29A**). Qiu et al. reported a c- $\text{TiO}_2$  ETL deposited by e-beam induced evaporation for flexible PSCs with a PCE of 13.5%.<sup>[282]</sup> They found that the pinholes in e-beam evaporated  $\text{TiO}_2$  layer would induce the incomplete coverage of the subsequently deposited perovskite layer. By optimizing the c- $\text{TiO}_2$  thickness, the pinholes of perovskite layers were reduced and the film coverage was increased, improving overall device performance. Furthermore, the low-temperature process of c- $\text{TiO}_2$  enabled the freedom of substrate choice. Shortly afterward, Qiu et al.<sup>[82]</sup> and Tait et al.<sup>[88]</sup> reported the pinhole-free large-scale PSMs based on e-beam evaporated c- $\text{TiO}_2$  layer, respectively. In Chen's work, 2D layered atomic sheets of titania were demonstrated in PSCs, which were fabricated through the solution-processed self-assembly atomic layer-by-layer deposition technique.<sup>[283]</sup> The atomic stacking  $\text{TiO}_2$  transport layer has significantly inhibited UV-induced degradation of perovskite films compared to the conventional c- $\text{TiO}_2$  ETM due to the unique features of high UV transparency and negligible oxygen vacancies of 2D titania atomic sheets. This discovery opens up a new path to utilize the 2D titania in the fabrication of large-area PSCs with the low-temperature solution process.

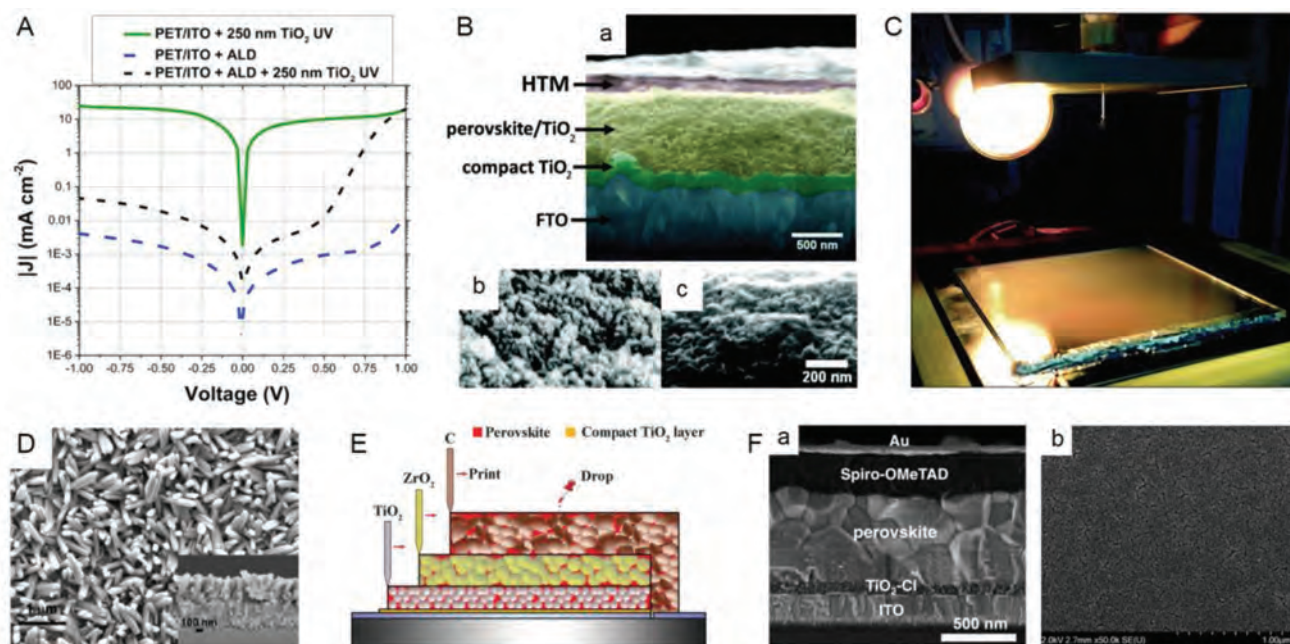


**Figure 29.** A) Tafel plot measured in dark. Green continuous line is for a cell without compact layer, blue dashed line for a cell with ALD compact layer without scaffold, and black dashed-dotted line for a cell with ALD compact layer and UV-irradiated TiO<sub>2</sub>. Reproduced with permission.<sup>[84]</sup> Copyright 2015, Wiley-VCH. B) Cross-sectional FE-SEM images of a) PSM with higher magnification, b) sintered m-TiO<sub>2</sub> made with diluted screen-printed paste, and c) m-TiO<sub>2</sub> covered with perovskite layer. B) Reproduced with permission.<sup>[80]</sup> Copyright 2014, Royal Society of Chemistry. C) Photo of ESD equipment during deposition on a 10 × 10 cm<sup>2</sup> large-area substrate. Reproduced with permission.<sup>[284]</sup> Copyright 2015, Royal Society of Chemistry. D) Top view of as-grown rutile nanorods on the FTO surface. Inset shows a cross section of nanorods. Reproduced with permission.<sup>[81]</sup> Copyright 2015, American Chemical Society. E) Schematic drawing showing the cross section of the fully printed HTM-free PSCs. Reproduced with permission.<sup>[41]</sup> Copyright 2014, American Association for the Advancement of Science. F) Device structure and cross-sectional SEM image of planar PSCs a). b) Top-view SEM image of the TiO<sub>2</sub>-Cl film on an ITO substrate. F) Reproduced with permission.<sup>[110]</sup> Copyright 2017, American Association for the Advancement of Science.

**Mesoporous TiO<sub>2</sub>:** In a double-layer TiO<sub>2</sub>-based ETL, a mesoporous TiO<sub>2</sub> layer as a scaffold is usually deposited on the very thin c-TiO<sub>2</sub> film acting as a hole blocking layer by screen-printing or spin-coating techniques. In large-area PSCs, spin-coating process is the common technique for fabricating m-TiO<sub>2</sub> films due to its accessibility in lab condition, which has been applied to high-performance PSMs.<sup>[30,53,59,62,102]</sup> Compared to spin-coating process, screen printing is more suitable for large-area production of m-TiO<sub>2</sub> based ETLs, resulting from its economization of raw materials and cost saving. In 2014, the first monolithic series-type PSM was reported by Matteocci et al., which achieved a PCE of 5.1%.<sup>[80]</sup> For realizing an efficient upscaling process of ETLs, customized formulation of TiO<sub>2</sub> paste was screen-printed to fabricate the m-TiO<sub>2</sub> layer. SEM showed that the thickness of the c-TiO<sub>2</sub> layer and the screen-printed TiO<sub>2</sub> scaffold was 110 nm and 700 nm, respectively (Figure 29B). Shortly afterward, with the same ETL, the PCE improved to 8.2%, and further was raised to 13% for the MAPbI<sub>3</sub>-based PSMs by the same research group.<sup>[61]</sup> At the end of 2014, Razz et al. reported a large-area (100 cm<sup>2</sup>) PSM with a PCE of 10.4%, and the m-TiO<sub>2</sub> as the ETL in PSMs was also fabricated by screen printing.<sup>[65]</sup> Kim et al. reported an electro-spray deposition (ESD) system to fabricate the m-TiO<sub>2</sub> ETL.<sup>[284]</sup> They found that the electro-sprayed TiO<sub>2</sub> film could be well penetrated by the perovskite due to the more porous structure and the less point defects compared to the spin-coated counterpart. Furthermore, a uniform m-TiO<sub>2</sub> film with an area of

10 × 10 cm<sup>2</sup> was fabricated, verifying the large-area coating capability of the ESD process (Figure 29C).

Although TiO<sub>2</sub> nanoparticles (NP-TiO<sub>2</sub>) are widely used to fabricate the m-TiO<sub>2</sub> scaffold in PSCs, they suffer from obsession of perovskite penetration into the nanopores due to their labyrinthine networks.<sup>[285]</sup> The m-TiO<sub>2</sub> scaffold made from vertical TiO<sub>2</sub> nanorods (NR-TiO<sub>2</sub>) have a more open porous structure, which can improve the infiltration of the perovskite materials and thus help the charge extraction.<sup>[278]</sup> In addition, the 1D morphology of the nanorods offers a directive path for electron transport to the electrode and minimizes the charge transport resistance in the nanorods. Fakharuddin et al. reported a large-area PSM employing vertically aligned NR-TiO<sub>2</sub> (Figure 29D) as the ETL, which showed a good photovoltaic performance and a remarkable stability compared to the control PSM with NP-TiO<sub>2</sub>, affirming the crucial role of the ETL and scaffold on device efficiency and stability.<sup>[81]</sup>

Another important type of PSCs is the HTM-free structure first reported by Han and co-workers (Figure 29E), which used a double layer of m-TiO<sub>2</sub> and m-ZrO<sub>2</sub> as a scaffold infiltrated by perovskites without an HTL.<sup>[40,41]</sup> For a PSM, layers of m-TiO<sub>2</sub> and m-ZrO<sub>2</sub> were screen-printed successively on a c-TiO<sub>2</sub> covered FTO substrate.<sup>[127]</sup> The thickness of each layer could be controlled by varying the mesh of the screen mask and the concentration of the paste. ZrO<sub>2</sub> worked as a spacer to separate the m-TiO<sub>2</sub> layer and the carbon electrode for avoiding short circuit. The 10 × 10 cm<sup>2</sup> module showed a 10.4% PCE



with high stability. Priyadarshi et al.<sup>[126]</sup> and Grancini et al.<sup>[128]</sup> also reported large-area PSMs by using m-TiO<sub>2</sub>/m-ZrO<sub>2</sub> based HTM-free structure, which exhibited high efficiency and high stability.

**Doped TiO<sub>2</sub>:** Although TiO<sub>2</sub> is commonly employed as the ETL for transferring electrons while blocking holes, the pristine TiO<sub>2</sub> still has relatively low electron mobility of 0.1–4 cm<sup>2</sup> V<sup>-1</sup> s<sup>-1</sup>, which can lead to nonessential Ohmic losses or nonideal space charge distribution in PSCs.<sup>[286]</sup> Many research reports have focused on the optimization of the electron transport property in the device by doping the TiO<sub>2</sub> ETL to enhance the performance of large-area PSCs. In Zhou et al.'s work, they increased the conductivity of the ETL by doping yttrium element into TiO<sub>2</sub> (Y-TiO<sub>2</sub>).<sup>[287]</sup> The Y-TiO<sub>2</sub> film showed a high conductivity of 2 × 10<sup>-5</sup> S cm<sup>-1</sup> matched with that of HTM, which balanced the carrier transport and reduced nonideal space charge distribution. Chen et al. reported a Nb doped TiO<sub>x</sub> used as ETL in large-area PSCs.<sup>[51]</sup> The Nb dopant increased the conductivity of the amorphous TiO<sub>x</sub> film from ≈10<sup>-6</sup> S cm<sup>-1</sup> to 10<sup>-5</sup> S cm<sup>-1</sup>, which reduced the electron transfer resistance at the PCBM/ Ti(Nb)O<sub>x</sub>/Ag interface and promoted electron transport, thus increasing the photocurrent. Tan et al. reported a contact passivation strategy of employing chlorine-capped nanotitania (TiO<sub>2</sub>-Cl) as the ETL for high-efficiency large-area PSCs.<sup>[110]</sup> The spin-coated TiO<sub>2</sub>-Cl film was not only smooth and pinhole-free, but also decreased deep trap-states at the TiO<sub>2</sub>-Cl/perovskite interface, hence remarkably inhibiting the interfacial charge recombination. The TiO<sub>2</sub>-Cl-based PSCs showed a better performance than that of the TiO<sub>2</sub> reference for all photovoltaic parameters (Figure 29F). Agresti et al. doped the m-TiO<sub>2</sub> layer with graphene flakes to modulate the charge dynamic.<sup>[70]</sup> In addition, lithium-neutralized graphene oxide flakes was introduced as the interlayer at the m-TiO<sub>2</sub>/perovskite interface with the aim of improving the charge injection from the perovskite to the m-TiO<sub>2</sub>. The large-area PSMs exhibited high efficiency and long term stability owing to the 2D nature of graphene for interface engineering.

### 5.1.2. Other Inorganic ETMs

Despite being widely used as the ETM in PSCs, TiO<sub>2</sub> still has some drawbacks. 1) High-temperature post-treatment increases the cost for scale-up devices. Although several low-temperature technologies, such as magnetron sputtering, ALD and electron beam evaporation, have been developed, these methods usually require high degree of vacuum, which undoubtedly increases the cost and preparation time. 2) Low electron mobility may cause unbalanced charge transport, finally resulting in the degradation of the device performance. 3) The device degradation can rapidly occur when TiO<sub>2</sub>-based PSCs are exposed to UV illumination. Therefore, researchers committed to develop new metal oxide as ETMs to replace TiO<sub>2</sub> in PSCs, such as ZnO,<sup>[288]</sup> SnO<sub>2</sub>,<sup>[289]</sup> tungsten trioxide (WO<sub>3</sub>),<sup>[290]</sup> Niobium pentoxide (Nb<sub>2</sub>O<sub>5</sub>),<sup>[291]</sup> strontium titanate (SrTiO<sub>3</sub>),<sup>[292]</sup> and barium stannate (BaSnO<sub>3</sub>).<sup>[293]</sup> In this part, we mainly introduce ETMs that have been successfully applied in large-area PSCs.

**Zinc Oxide:** ZnO has the similar energy bands to TiO<sub>2</sub>, which is seen as a promising alternative in PSCs owing to

many advantages as below. 1) High electron mobility of nearly 200 cm<sup>2</sup> V<sup>-1</sup> s<sup>-1</sup> is 2 orders of magnitude higher than that of TiO<sub>2</sub>.<sup>[294]</sup> 2) Low-temperature process can form high crystallinity of ZnO without a sintering procedure.<sup>[288]</sup> 3) High transmittance in the visible region can maximize the light harvesting of perovskites. 4) Low cost of the raw materials. There are reviews specifically for the application of ZnO in PSCs.<sup>[288]</sup> To date, the best PCE of ZnO-based small-area PSCs is 17.6%, which is lower than that of TiO<sub>2</sub>-based devices.<sup>[295]</sup> However, ZnO shows potential in preparing large-area PSCs, even in flexible photovoltaic devices. Vak et al. reported a 47.3 cm<sup>2</sup> size PSM using ZnO as the ETL by spin-coating process, and the ETL film was annealed at low temperature of about 140 °C.<sup>[63]</sup> They found that the variation of the ZnO coating conditions has little or no effect on the device performance. A fully printed large-area PSC was fabricated and a slot die-coated ZnO was employed as the ETL.<sup>[64]</sup> It was revealed that the slot die-coated ZnO layers were as good as the spin-coated films. The slot die-coated ETL based on ZnO verifies the possibility of the low-cost mass production of large-area PSCs. However, ZnO still has some drawbacks, for example reducing the stability of PSCs due to its hygroscopicity.

**Stannic Oxide:** SnO<sub>2</sub> is another intrinsic n-type semiconductor that has been applied as ETL in PSCs owing to its natural abundance, nontoxic, low hygroscopicity, good stability and high transparency.<sup>[278]</sup> SnO<sub>2</sub> also has high electron mobility of 250 cm<sup>2</sup> V<sup>-1</sup> s<sup>-1</sup>, which enhances the electron transport ability of the ETL.<sup>[294]</sup> SnO<sub>2</sub>-based PSCs show a good thermal and UV stability. Furthermore, high-temperature annealing is not necessary for most SnO<sub>2</sub> fabrication methods, which means that it can be produced with a low cost and thus be potentially used in large-area PSCs.<sup>[289,296]</sup> To date, numerous research efforts have focused on SnO<sub>2</sub>-based small-scale PSCs.<sup>[278]</sup> However, a few studies on applying SnO<sub>2</sub> in large-scale PSCs have been reported. With compact SnO<sub>2</sub> as the ETL, Bu et al. fabricated a small-area PSCs with a PCE of 20.56% and a large-area PSM with a PCE of 15.76% without hysteresis, which demonstrated the application prospects of the SnO<sub>2</sub>-based ETL for potential upscaling PSCs.<sup>[115]</sup>

### 5.2. Organic ETMs

Fullerene C<sub>60</sub> and its derivatives PCBM are the most commonly used ETMs in inverted p-i-n PSCs.<sup>[297]</sup> Since the first report of fullerene type ETMs used in PSCs,<sup>[38]</sup> the PCE of small-area devices has exceeded 20%.<sup>[39]</sup> For the large-area PSC fabrication, PCBM have won the favor of researchers owing to a lot of advantages, such as the low-temperature process, compatible energy-level alignment with respect to perovskite and good electron extraction property.<sup>[38,298]</sup> More importantly, PCBM can passivate the charge traps on the perovskite grain boundaries.<sup>[299]</sup> According to the statistics, until now most of p-i-n-type large-area PSCs have used PCBM as an ETL.<sup>[34,39,55,56,58,66,69,72,85,87,90,99,100,103,130,197]</sup> In 2015, Heo et al. reported an inverted p-i-n PSCs with PCBM as the ETL, which exhibited a high PCE of 18.1% in small-area devices and 12.9% in large-area modules.<sup>[34]</sup> Wu et al. reported an inverted PSC architecting a perovskite-PCBM graded heterojunction structure.<sup>[103]</sup> In this structure, PCBM was distributed in the perovskite layer with a gradient,

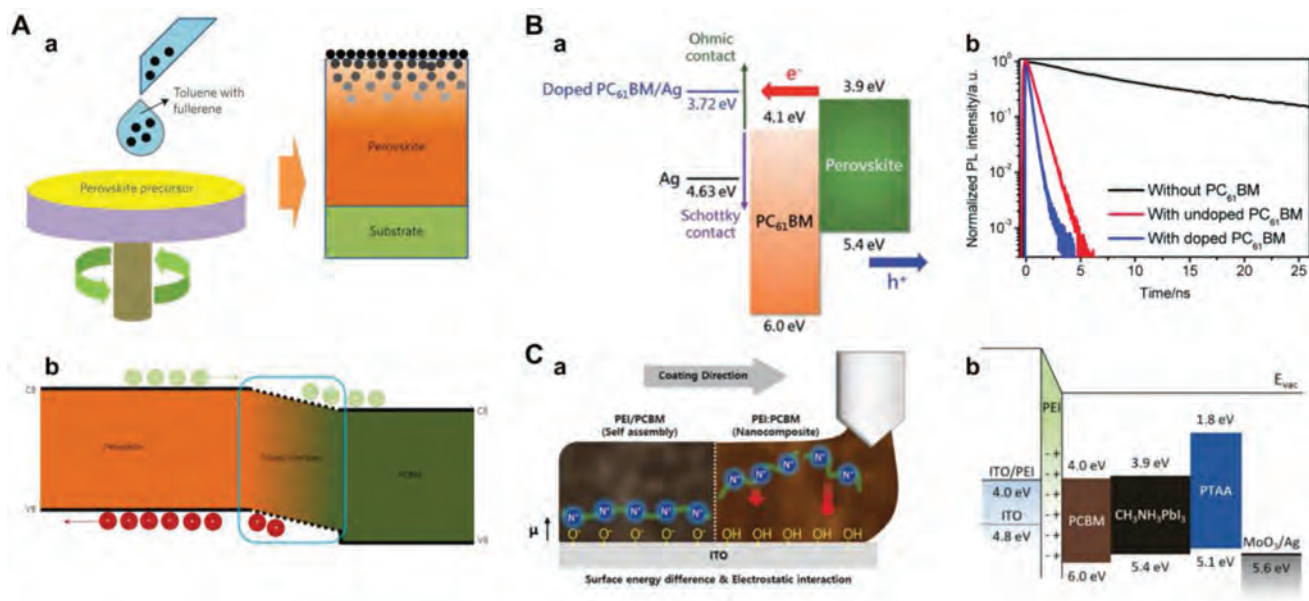


**Figure 30.** A) Schematic diagram of the deposition method. The black dots represent fullerene a). b) Schematic diagram of band shift of perovskite and PCBM in GHJ structure with a mixed and graded interlayer. The negative and positive circles represent electrons and holes, respectively, and the arrows indicate their flowing directions. A) Reproduced with permission.<sup>[103]</sup> Copyright 2016, Nature Publishing Group. B) Energy level diagram at the active layer/cathode interface a). b) Time-resolved PL spectra of perovskite films with and without PC<sub>61</sub>BM layer. B) Reproduced with permission.<sup>[99]</sup> Copyright 2016, Royal Society of Chemistry. C) Proposed scheme for the self-assembly of the PEI in the PEI:PCBM during the printing process a). b) Energy level diagram of the corresponding device. C) Reproduced with permission.<sup>[54]</sup> Copyright 2017, Wiley-VCH.

which could enhance the device efficiency due to the improved photoelectron collection and reduced charge combination (Figure 30A). The conformal fullerene coating via the GHJ deposition achieved a full coverage on the perovskite with reduced layer thickness, thus minimizing the resistance loss in large-size devices. With this strategy, 1 cm<sup>2</sup> area PSCs with a PCE of 18.2% was obtained. Despite several advantages of PCBM as the ETL in PSCs, the mismatch between the high work function of the environmentally stable metal (e.g., Ag or Au) and the LUMO level of PCBM usually compromises the device performance. One strategy to solve the problem is inserting a cathode buffer layer (CBL) to achieve appropriate energy-level matching at the PCBM/cathode interface. Chang and co-workers reported a cetyltrimethylammonium bromide (CTAB)-doped PCBM as both the ETL and CBL.<sup>[99]</sup> The doped interfacial layer modified the WF of Ag electrode, which provided a good energy-level matching with the PCBM layer and formed Ohmic contact for efficient electron extraction (Figure 30B). In addition, the anion-induced electron transfer between the bromide anions (Br<sup>-</sup>) on CTAB and PCBM in the solid state could remarkably increase the electrical conductivity of PCBM by more than 5 orders of magnitude. With the n-doped PCBM layer, a 1.2 cm<sup>2</sup> area PSC with a remarkable PCE of 15.42% was obtained. By the same strategy, the PSCs with an active area of 1.2 cm<sup>2</sup> via doctor-blade coating technique also exhibited a PCE of more than 15%.<sup>[100]</sup> Engineering the interface between the ETL and the electrode was also studied in normal n-i-p-type PSCs. Lee et al. used polyethyleneimine (PEI) as the surface work-function modifier and PCBM as the ETM to form the self-assembled organic-nanocomposite ETL in PSCs (Figure 30Ca).<sup>[54]</sup> This ETL exhibited efficient electron transfer from the perovskite to the

PCBM due to its strong electron affinity. Moreover, the interfacial PEI dipole decreased the work function of the ITO cathode and formed a desirable Ohmic contact between the PCBM and ITO (Figure 30Cb). Based on this method, low-temperature-processed, hysteresis-free, and stable PSCs with a large area up to 1 cm<sup>2</sup> were obtained, which exhibited a stabilized PCE of over 18%. In addition, the organic nanocomposite concept was successfully applied to the printing process, resulting in a PCE of over 17% in PSCs with the printed ETL.

## 6. Electrode Materials

The typical structure of PSCs contains a bottom electrode and a top electrode, which are used to collect the electrons or holes. In this section, we introduce the promising electrodes with the potential of low-cost and facile fabrication in order to replace the conventional counterparts used in large-area PSCs.

### 6.1. Bottom Electrodes

Bottom electrodes of PSCs are typically transparent conductive oxides (TCOs) such as FTO and ITO, which usually deposited on a glass substrate by a vacuum deposition technique. Although FTO and ITO have been widely used in large-scale PSCs as the transparent substrate, TCOs have limits due to their fabrication cost, brittleness and the scarcity of raw materials (especially indium). Scientists are currently searching for alternatives to ITO and FTO. However, it is not easy to develop alternative candidates because of the high transparency and

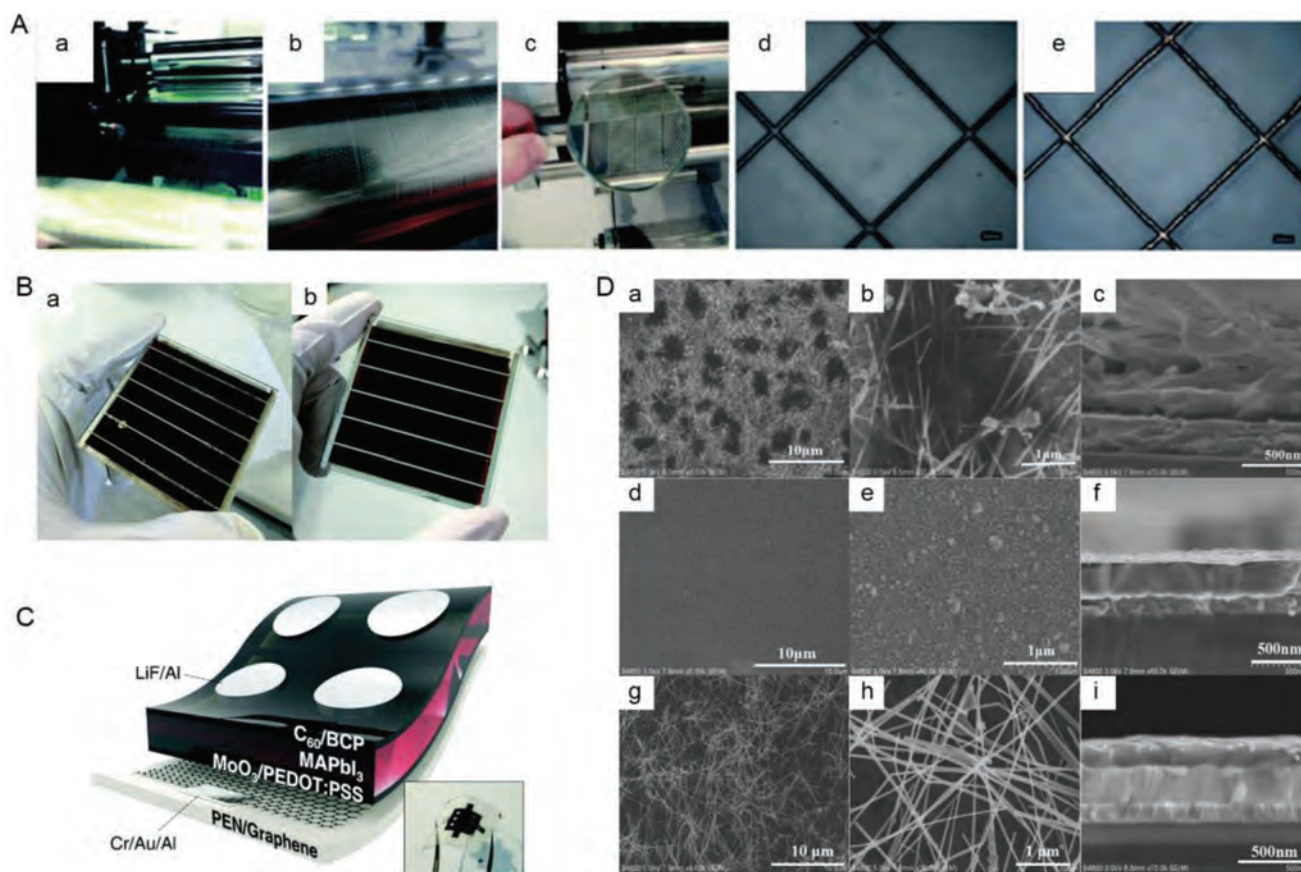


**Figure 31.** A) Thermal imprinting of PET using a nickel master roll a). b) Flexographically printed grid shown as the wet film with the red glow from the infrared drier. c) The inkjet-printed grid shown after hot air drying. d) The thermally imprinted grid prior to silver filling. e) The silver filled grid. A) Reproduced with permission.<sup>[302]</sup> Copyright 2012, Royal Society of Chemistry. B) Photographs of 25 cm<sup>2</sup> PSCs with a) a Ag grid and b) an Al/Al<sub>2</sub>O<sub>3</sub> grid. The degradation of the organohalide perovskite layer after several days can be seen adjacent to the Ag lines a), but not around the Al/Al<sub>2</sub>O<sub>3</sub> lines b). B) Reproduced with permission.<sup>[304]</sup> Copyright 2016, Royal Society of Chemistry. C) Device structure of graphene-based flexible perovskite solar cells (inset image: Photograph of a complete device). Reproduced with permission.<sup>[306]</sup> Copyright 2017, Royal Society of Chemistry. D) Top-view a,b,d,e,g,h) and c,f,i) cross-sectional SEM images of the printed AgNW electrode a–c), the thermal evaporated Ag electrode on perovskite/PC<sub>61</sub>BM surface d–f), and the printed AgNW electrode on perovskite/PC<sub>61</sub>BM/PEI surface g–i). D) Reproduced with permission.<sup>[320]</sup> Copyright 2018, Wiley-VCH.

electrical conductivity of TCOs compared with other conducting materials, such as metallic nanowires, carbon nanotubes (CNT), graphene and conducting polymers. Among the conducting materials, metallic nanowires are considered as the promising candidates for TCOs replacement owing to the solution-based deposition method, structural transparency, and low cost. Compared to the traditional TCOs, metallic nanomaterials such as silver nanowires (AgNWs) shows high transmittance ( $\approx 90\%$  at 550 nm) and comparable sheet resistance (less than  $20 \Omega \square^{-1}$ ) with commercial ITO electrode.<sup>[300]</sup> However, metallic nanowires cannot be directly used as transparent electrodes for photovoltaic devices due to the large-size holes and inhomogeneous resistance distribution throughout the conducting film. To solve the problem, metallic nanowires are generally combined with the conductive polymer PEDOT:PSS for a substitute TCOs. Kim et al. demonstrated the stable AgNW/PEDOT:PSS film by using roll-to-roll slot-die coating, which exhibited the suitable sheet resistance of  $\approx 75 \Omega \square^{-1}$  and good transmittance ( $T > 90\%$  at 550 nm).<sup>[301]</sup> In spite of rare report on applying metallic nanowires as bottom electrodes in PSCs,

the fully printed metal grid electrode can be a feasible alternative for large-scale TCOs.<sup>[302,303]</sup> Yu et al. demonstrated printed bottom electrodes from the aqueous-nanoparticle-based silver ink by several different roll-to-roll techniques, such as thermally imprinted, inkjet, and flexographic printing, as shown in **Figure 31A**.<sup>[302]</sup> Hamsch et al. utilized simple aluminum grid lines to achieve the 25 cm<sup>2</sup> aperture-area PSCs without an interconnected strip design due to increasing the conductivity of the transparent electrode.<sup>[304]</sup> These Al grid were exposed to an UV–ozone plasma to form a thin Al<sub>2</sub>O<sub>3</sub> coating, which remarkably improved the wetting and film-forming of the casting solutions (PEDOT:PSS and perovskite) and thus avoided the leakage current. The monolithic devices based on the Al/Al<sub>2</sub>O<sub>3</sub> grid achieved a maximum PCE of 6.8% and showed a better stability than that of the Ag-grid based PSCs, as shown in **Figure 31B**. Graphene, a single-layer 2D carbon material, is another promising candidate to replace TCOs due to its high transparency ( $T \approx 97\%$  in visible range), flexibility, mechanical strength and stretchability. TCO-free PSCs with graphene anode were first demonstrated by Sung et al.<sup>[305]</sup> The graphene based devices



showed a high PCE of 17.2%. The high transparency and low surface roughness of the graphene electrode compensated its low conductivity compared to the ITO counterpart, resulting in comparable  $J_{sc}$ , high  $V_{oc}$ , and therefore high PCE. In another work from the same group, a single-layer CVD graphene was transferred on a thin polyethylene naphthalate (PEN) substrate by a typical wet transfer process. The flexible PSCs based on the high-transparency graphene electrode exhibited a PCE of 16.8% without hysteresis. Moreover, the graphene-based flexible devices also showed a good bending stability, which maintained more than 85% of their initial PCEs after 5000 bending cycles (Figure 31C).<sup>[306]</sup>

## 6.2. Top Electrodes

Electrodes on the top of the devices are usually vacuum-deposited metals such as Au and Ag. Although Au is the most common electrode material for high efficient PSCs, the expensive price increases the production cost of devices. Ag is a low-cost candidate for large-area PSCs.<sup>[51,52,54,58,69]</sup> The heat-curable silver ink can be printed to fabricate the fully ambient roll-processing PSCs.<sup>[86]</sup> Unfortunately, Ag electrode suffers from corrosion or contamination in PSCs. Snaith et al. reported that Ag became corroded in contact with the perovskite film owing to the silver halide formation.<sup>[307]</sup> Furthermore, the metal electrode are also fabricated with a costly vacuum-assisted deposition process. By now, a variety of electrode candidates with economical solution process have been developed such as metal nanowires,<sup>[308]</sup> PEDOT:PSS,<sup>[309]</sup> carbon nanotubes,<sup>[43]</sup> and graphene.<sup>[310]</sup>

### 6.2.1. Metal Nanowire and Grid Electrodes

Metal nanowire electrodes are also potential top electrode materials for mass fabrication, owing to the facile fabricating methods, such as spin coating,<sup>[311]</sup> spray coating,<sup>[312]</sup> doctor blading,<sup>[313]</sup> and slot-die coating.<sup>[301]</sup> Furthermore, the raw materials of metal nanowires can be Ag,<sup>[308]</sup> Cu,<sup>[314]</sup> Ni,<sup>[315]</sup> or Au.<sup>[316]</sup> Guo et al. reported an efficient PSC using solution-processed silver nanowires as the top electrode with a PCE of 8.49%, where ZnO was used as the interlayer to improve the Ohmic contact between the AgNWs and the PCBM.<sup>[317]</sup> Lee et al. reported a fiber-shaped flexible PSC using silver nanowires as the top electrode, showing a PCE of 3.85%.<sup>[318]</sup> Yang et al. reported an all-solution route to produce semi-transparent PSCs with spray-coating silver nanowires as the top electrode, yielding a PCE of 10.64%.<sup>[319]</sup> Xie et al. reported the preparation of transparent silver nanowire top electrode for PSCs by a inkjet-printing process.<sup>[320]</sup> SEM images (Figure 31D) clearly indicated that chemical corrosion on the AgNW electrode was totally suppressed after the insertion of PEI layer. Furthermore, the thin PEI layer could minimize the charge injection barrier between PCBM and AgNW electrode and thus improve the device performance. A PCE of 14.17% was achieved for the PEI/AgNW cells. Ni and Cu nanowires are also successfully exploited as a transparent conductive electrode of PSCs.<sup>[321,322]</sup> However,

the main drawback for metal-nanowire electrode-based PSCs is that the polar solvent used for dispersing nanowires can degrade the underlying perovskite layers. Many efforts have been done to solve the problem. One way is to employ the nonpolar solvents.<sup>[300,317,319,323]</sup> The other way is to use mechanically transferred metal-nanowire network as a top electrode.<sup>[321,322,324–326]</sup> Although the metal nanowire network electrodes for large-scale PSCs show many advantages, such as low cost and facile large-scale fabrication, the performance of the device and the processing technologies still need to be further developed and optimized.

### 6.2.2. Carbon-Based Electrodes

Carbon-based materials as conducting electrodes in PSCs have attracted wide attention due to their low cost, stability, inertness to ion migration and inherently water repellency, which are advantageous to the improvement of the device stability. Furthermore, the work function of carbon (−5.0 eV) is close to Au (−5.1 eV), which enables it to be an ideal material to replace Au as a top electrode in PSCs.<sup>[40]</sup> Carbon-based PSCs (C-PSCs) have exhibited remarkable stability and become one of the most promising types of PSCs for commercialization. The breakthrough work of PSCs based on a mesoporous carbon electrode was developed by Ku and co-workers.<sup>[40]</sup> The mesocarbon electrode was fabricated from carbon black and spheroidal graphite by screen-printing technique (Figure 32A). PSC-based cheap carbon electrodes can be fully printed for mass production, showing advantages in both material and manufacturing cost. Since then, the carbon-based HTM-free device has gradually become an important structure type of PSCs and shows a great potential for large-area PSCs.<sup>[40,41,126,327,328]</sup> Chen et al. demonstrated a solvent engineering strategy to prepare a high-quality perovskite layer, which enabled the printable carbon electrode to form a much better contact, as shown in Figure 32B.<sup>[62]</sup> The large-size (1 cm<sup>2</sup>) device achieved a PCE of about 10%. Wei et al. designed a hole transporter-free PSC based on a C + epoxy electrode that can serve as both a hole extractor and a water-proof barrier.<sup>[329]</sup> By using a silver paint coating, the PSCs achieved a PCE of 11%, and exhibited a good stability against water. As shown in Figure 32C, the C + epoxy/Ag paint film is solid and hydrophobic compared to the C and C + epoxy films, thus blocking moisture and even water from perovskite. Several promising printed C-PSCs have shown excellent stability under high humidity or high temperature during long time.<sup>[330–332]</sup> Carbon nanotubes have also been applied as electrodes in PSCs owing to their excellent electrical conductivity, chemical stability and unique nanostructure. Furthermore, the flexible and transparent CNT electrodes show great potential in flexible or large-scale PSCs.<sup>[333–336]</sup> Ryu et al. used CNTs to penetrate into both the perovskite film and carbon electrode by solvent dripping method.<sup>[337]</sup> This strategy provided better contact at the perovskite/carbon interface, facilitating fast hole transfer. Luo et al. reported a novel inverted PSC employing a SnO<sub>2</sub>-coated cross-stacked superaligned carbon nanotube (SnO<sub>2</sub>@CSCNT) film as the top cathode and a Al<sub>2</sub>O<sub>3</sub> film as the spacer in both rigid and flexible devices.<sup>[338]</sup> As shown in

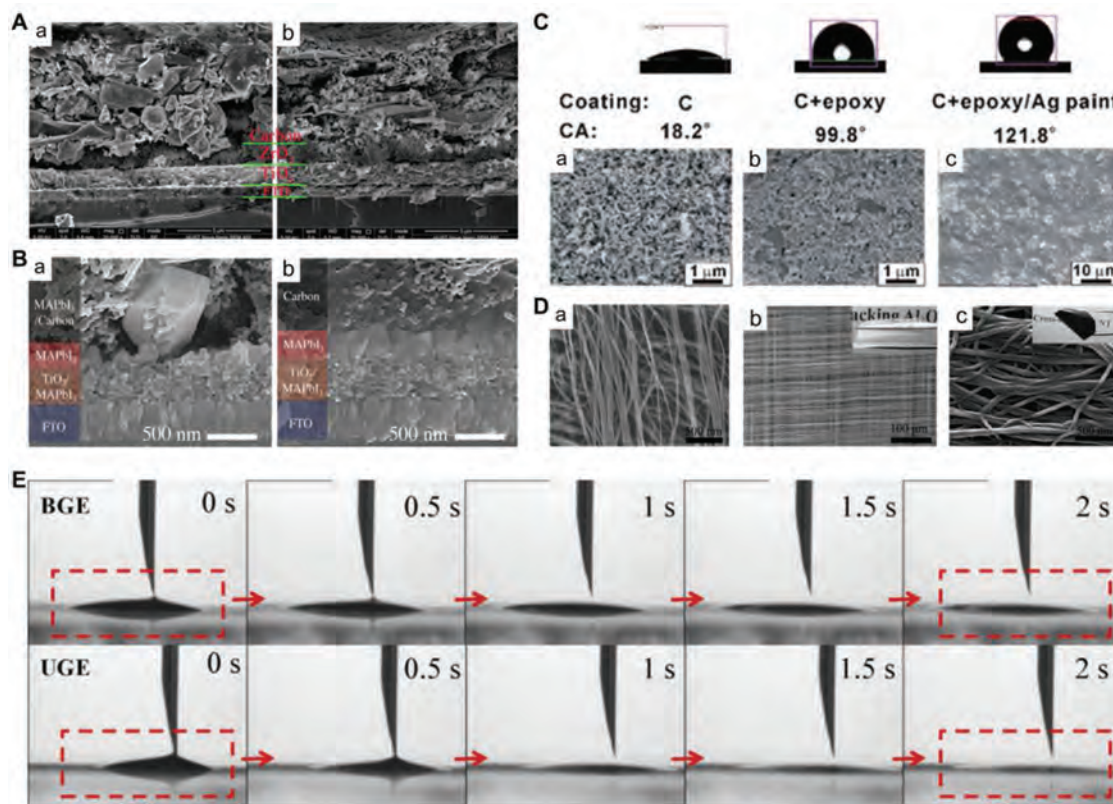


**Figure 32.** A) Cross-sectional structure of the monolithic devices based on a) spheroidal graphite (SG) and b) flaky graphite (FG). A) Reproduced with permission.<sup>[40]</sup> Copyright 2013, Nature Publishing Group. B) Cross-sectional SEM images of the carbon-based PSCs fabricated from a) IPA and b) IPA/cyclohexane solvents. B) Reproduced with permission.<sup>[62]</sup> Copyright 2016, Wiley-VCH. C) Contact-angle photographs and SEM images of the three films: a) C, b) C+ epoxy, and c) C+ epoxy/Ag paint. C) Reproduced with permission.<sup>[329]</sup> Copyright 2015, Royal Society of Chemistry. D) Typical SEM images of a) CSCNT film, b) Al<sub>2</sub>O<sub>3</sub> nanotube film, and c) SnO<sub>2</sub>@CSCNT film. D) Reproduced with permission.<sup>[338]</sup> Copyright 2017, Wiley-VCH. E) Optical images of contact-angle measurement for the PSC device on the bulk graphite/carbon black electrode and ultrathin graphite/carbon black electrode surface. Reproduced with permission.<sup>[339]</sup> Copyright 2017, Elsevier.

Figure 32D, the CSCNT film showed a typical cross-stacking structure, and the Al<sub>2</sub>O<sub>3</sub> film also exhibited the similar and porous features as its CSCNT template, which could help perovskite loading. For the SnO<sub>2</sub>@CSCNT electrode, the SnO<sub>2</sub> nanoparticles were continuously and uniformly coated on the surface of CSCNT, which significantly reduced charge recombination. The maximum efficiency of SnO<sub>2</sub>@CSCNT based devices was 14.3% for rigid substrates and 10.5% for flexible ones, respectively. Furthermore, the PSCs using the SnO<sub>2</sub>@CSCNT electrode exhibited good stability compared to the controlled devices with the Ag electrode, retaining 88% of their original PCEs after 550 h under light-soaking or thermal stress. Graphene is also a potential hole-extracting electrode material for C-PSCs due to the exceptional charge mobility and thermal conductivity. Duan et al. used ultrathin graphite (UG) to substitute bulk graphite (BG) to fabricate carbon electrode in an HTM-free, fully printed PSC, which effectively increased the specific surface area of the carbon electrode without reducing the conductivity.<sup>[339]</sup> Furthermore, the ultrathin graphite/carbon black electrode (UGE) presented more effective contact with the perovskite solution compared to the bulk graphite/carbon black electrode (BGE), accelerating the infiltration of perovskite precursor (Figure 32E).

This could be attributed to the highly interconnected channels of UGE caused by the large specific surface area, resulting in a low charge transfer resistance at the perovskite/carbon-electrode interface. You et al. fabricated a semitransparent PSC based on the stacked multilayer graphene prepared by CVD method as the transparent top electrode.<sup>[340]</sup> By coating a thin layer of PEDOT:PSS to enhance the conductivity of graphene electrode, the PSCs with graphene electrodes exhibited an average PCE of 12.02% or 11.65% for the FTO- or graphene-side illumination, respectively. Moreover, the CVD graphene electrode prepared on flexible plastic substrates could be laminated on perovskite active layers at low temperature of ≈60 °C under pressure, which showed a potential application for flexible PSCs.

## 7. Stability Issues

The poor long-term device stability is one of the major issues of PSCs for further commercial applications. Although numbers of studies have focused on the stability of small-area PSCs, few research on large-area PSCs is reported. However, the larger the PSC size is, the easier the device performance

is to be affected by the unstable sources, such as humidity, thermal, light, and ion migration. In this section, several key researches on the stability of small-area PSCs are reviewed, which are expected to attract more attention of the durability of large-area devices, enhancing the potential for the commercialization of this technology.

### 7.1. Moisture Effect

The effect of water on the performance of PSCs has been a hot spot. Studies have shown that the presence of proper humidity during the film processing can improve the film formation of perovskite. However, for fully formed PSCs, exposure to moisture eventually leads to the device degradation. Therefore, in order to achieve stable perovskite devices, it is very important to fully understand the mechanism of the perovskite degradation caused by water. Frost et al. proposed an acid–base reaction mechanism to explain the pathway of perovskite degradation.<sup>[341]</sup> The hybrid perovskite could react with the trace of water (Lewis base) in a closed device system, which would finally lead to partial decomposition of the perovskite until either H<sub>2</sub>O was saturated by generated HI or the CH<sub>3</sub>NH<sub>2</sub> vapor pressure reached equilibrium. In this case, the process was irreversible and the degradation of device performance was inevitable. One strategy for improving moisture stability is modification of perovskite structure. By inserting the large-size organic cations into the perovskite structure, the multidimensional perovskite materials exhibit superior stability and water resistance, as discussed in Section 3.3.3. The other strategy is to use hydrophobic charge transport layers as a barrier against water. For example, Spiro-OMeTAD is easy to absorb moisture due to the addition of lithium salt, dopant-free HTMs with hydrophobic groups can solve the problem and improve the device stability without losses of the performance. The specific molecular structure of the dopant-free HTMs can be found in Section 4.1.2.

### 7.2. Thermal Instability

Thermally induced degradation of PSCs can occur in the active layer, the charge transport layer, and even in the electrode. For perovskite materials, MAPbI<sub>3</sub> shows poor thermal stability due to the low reversible phase transition temperature. Although FAPbI<sub>3</sub> exhibits better temperature stability than MAPbI<sub>3</sub>, it lacks structural stability at room temperature. This problem can be solved by modification of the perovskite structure to suppress the phase transition, such as using the mixed organic cations (MA/FA), introducing inorganic cations into MA/FA perovskite precursor or using multidimensional perovskites instead of the conventional 3D analogs, as discussed in Section 3. The inorganic ETLs are usually considered thermal stable owing to the natural high-temperature resistance. The organic HTMs should exhibit high glass transition temperature by optimizing the molecular structure in order to improve the stability of the device under operating conditions. For the electrode, Domanski et al. found that gold could migrate through the HTL into

the perovskite materials and cause a dramatic performance loss when PSCs were exposed to a temperature of 70 °C.<sup>[342]</sup> By inserting a Cr metal interlayer between the electrode and HTL, the thermal-induced degradation of the device could be prevented. This research revealed that the thermal degradation is not necessarily from the decomposition of the HTM or perovskite layer, but probably from the metal migration.

### 7.3. Ion Migration

Ion migration from perovskites has been recently identified as a key source of degradation. Theoretical and experimental studies clearly confirm that halide, ammonium, and even proton migration can lead to the performance deterioration of the perovskites. Li et al. demonstrated a real-time observation method for iodide ion migration of perovskite films in an electric field by a wide-field PL imaging microscopy.<sup>[343]</sup> The migration and accumulation of iodide ions under external fields gave rise to the formation of PL inactive domains, and therefore affected the device performance. Guerrero et al. revealed that the reaction of the perovskite with the metal electrode was the major degradation pathway of the device in the absence of water.<sup>[344]</sup> This work highlighted the importance to use the protecting layers to stabilize the transport of iodide ions in the perovskite layer. Carrillo et al. identified two types of reaction sources between the perovskite and the charge transport layers (TiO<sub>2</sub> and Spiro-OMeTAD).<sup>[345]</sup> i) The weak Ti–I–Pb bond boosted interfacial accumulation of iodide ions. Although this produced a highly reversible capacitive current from the TiO<sub>2</sub>/MAPbI<sub>3</sub> interface, the steady-state photovoltaic characteristics did not be changed. ii) The chemical reaction between the Spiro-OMeTAD<sup>+</sup> and I<sup>−</sup> ions was irreversible, which gradually reduced the HTL conductivity and thus degraded the device. Correa-Baena et al. measured the PSCs by a series of methods, such as photovoltage versus light intensity, open-circuit voltage decay, and electrochemical impedance spectroscopy, to study the recombination mechanism of fresh and cycled PSCs.<sup>[346]</sup> The bulk recombination was dominant in the fresh PSCs. When the device was exposed to light or electrical field, migrating ions would build up at the contact interfaces between perovskites and charge transport layers. The charge recombination would mainly occur at the contact interface due to ion migration. Therefore, for further improving the stability of PSCs, it is important to completely understand the mechanism and tuning method of ion migration in the operating PSC device.

## 8. Conclusion and Perspectives

Perovskite solar cells as a promising candidate for the next generation of photovoltaic technologies have recently gained much attention both from the scientific and industrial community. To date, the power conversion efficiency of the small-area PSCs has exceeded 22%, which is close to commercial silicon photovoltaic cells. Even though the performance of PSCs exhibits a dramatic improvement, the difficulty on scaling-up becomes a bottleneck of industrialization. The





**Figure 33.** Vision for the future of large-area commercial perovskite solar cells.

efficiency and stability issues from area enlargement are urgent to be concerned and solved. In this review, we summarized the researches on large-area PSCs in recent years. Approaches for fabricating the larger-area PSCs are described in terms of each functional layer materials, including perovskite materials, hole transport materials, electron transport materials, and electrode materials. To achieve future commercial applications, the efficiency, stability, materials cost, and fabrication techniques involved in PSCs have to be addressed. The commercially oriented large-area PSCs should be efficient, stable, and able to compete with existing technologies on price. This requires scientists and researchers to constantly try and explore the functional materials that are suitable for fabricating large-area PSCs. There are several key research areas and challenges that need to be expanded upon and addressed for enhancing the commercial potential for perovskite photovoltaic technology. 1) Perovskite materials: Novel film-forming procedures should be further developed to obtain large-scale and high quality perovskite films. Although mixed-ion 3D perovskites have shown the better performance than pure perovskite compounds, the ambient stability still remains an obstacle for commercialization. Multidimensional perovskites exhibiting superior stability and water resistance compared to the 3D counterparts are highly promising to achieve both efficient and stabilized device, and therefore should be given great attention. 2) Hole transport materials: In addition to the basic requirements of HTMs, such as high hole mobility, well-aligned energy levels with perovskites, well solubility, high thermal and photochemical stability as well as high hydrophobicity, an ideal HTM candidate to substitute traditional materials for large-scale PSC manufacturing should have several main advantages, such as high-efficiency, nondoped, and low cost. 3) Electron transport materials: The inorganic metal oxide-based ETMs are usually used in n-i-p-type PSCs. Low-temperature processing techniques of ETMs should be further developed for large-area preparation. For inverted p-i-n-type PSCs, the most commonly used ETMs, such as fullerene C<sub>60</sub> and its derivatives PCBM, have the problem of the mismatched work function with the environmentally stable metal electrodes. Developing nonfullerene derivatives is imminent. 4) Electrode materials: Metal nanowire network electrode and carbon-based electrode show promising advantages for fabricating large-scale

PSCs, such as low cost, high stability, facile large-scale fabrication, and so on. However, the device performance and the processing technologies still need to be further developed and optimized. Finally, long-term stability of PSCs is an essential part of further commercial applications. Just as Buckets effect reveals (Figure 33), the capacity of a bucket depends on the shortest board. The ultimate goal of PSC commercialization requires the collaboration of interdisciplinary scientists to find new stable perovskite materials, to select suitable charge transport layers and electrodes, as well as to develop cost-effectively manufacturing processes. Predictably, in the near future, perovskite

solar cells will become one of the most competitive alternatives to silicon solar cells.

## Acknowledgements

This work was supported by the National Key Research and Development Program of China (Grant No. 2017YFB0404500), the National Basic Research Program of China Fundamental Studies of Perovskite Solar Cells (Grant No. 2015CB932200) and the Natural Science Foundation of Jiangsu Province, China (Grant No. BK20150064).

## Conflict of Interest

The authors declare no conflict of interest.

## Keywords

electron transport materials, hole transport materials, large-area solar cells, perovskite solar cells, photovoltaics

Received: May 31, 2018  
Revised: September 2, 2018  
Published online:

- [1] A. Kojima, K. Teshima, Y. Shirai, T. Miyasaka, *J. Am. Chem. Soc.* **2009**, *131*, 6050.
- [2] J. P. Correa Baena, L. Steier, W. Tress, M. Saliba, S. Neutzner, T. Matsui, F. Giordano, T. J. Jacobsson, A. R. Srimath Kandada, S. M. Zakeeruddin, A. Petrozza, A. Abate, M. K. Nazeeruddin, M. Grätzel, A. Hagfeldt, *Energy Environ. Sci.* **2015**, *8*, 2928.
- [3] T. Jesper Jacobsson, J.-P. Correa-Baena, M. Pazoki, M. Saliba, K. Schenk, M. Grätzel, A. Hagfeldt, *Energy Environ. Sci.* **2016**, *9*, 1706.
- [4] D. Bi, W. Tress, M. I. Dar, P. Gao, J. Luo, C. Renevier, K. Schenk, A. Abate, F. Giordano, J.-P. Correa Baena, J.-D. Decoppet, S. M. Zakeeruddin, M. K. Nazeeruddin, M. Grätzel, A. Hagfeldt, *Sci. Adv.* **2016**, *2*, e1501170.
- [5] M. Saliba, T. Matsui, J. Y. Seo, K. Domanski, J.-P. Correa-Baena, M. K. Nazeeruddin, S. M. Zakeeruddin, W. Tress, A. Abate, A. Hagfeldt, M. Grätzel, *Energy Environ. Sci.* **2016**, *9*, 1989.
- [6] W. S. Yang, J. H. Noh, N. J. Jeon, Y. C. Kim, S. Ryu, J. Seo, S. I. Seok, *Science* **2015**, *348*, 1234.

- [7] D. Bi, C. Yi, J. Luo, J.-D. Décoppet, F. Zhang, S. M. Zakeeruddin, X. Li, A. Hagfeldt, M. Grätzel, *Nat. Energy* **2016**, *1*, 16142.
- [8] M. Saliba, S. Orlandi, T. Matsui, S. Aghazada, M. Cavazzini, J.-P. Correa-Baena, P. Gao, R. Scopelliti, E. Mosconi, K.-H. Dahmen, F. De Angelis, A. Abate, A. Hagfeldt, G. Pozzi, M. Graetzel, M. K. Nazeeruddin, *Nat. Energy* **2016**, *1*, 15017.
- [9] M. Hadadian, J.-P. Correa-Baena, E. K. Goharshadi, A. Ummadisingu, J.-Y. Seo, J. Luo, S. Gholipour, S. M. Zakeeruddin, M. Saliba, A. Abate, M. Grätzel, A. Hagfeldt, *Adv. Mater.* **2016**, *28*, 8681.
- [10] NREL, *Best Research-Cell Efficiencies chart*; [www.nrel.gov/pv/assets/images/efficiency-chart-20180716.jpg](http://www.nrel.gov/pv/assets/images/efficiency-chart-20180716.jpg).
- [11] J.-H. Im, I.-H. Jang, N. Pellet, M. Grätzel, N.-G. Park, *Nat. Nanotechnol.* **2014**, *9*, 927.
- [12] S. Sun, T. Salim, N. Mathews, M. Duchamp, C. Boothroyd, G. Xing, T. C. Sum, Y. M. Lam, *Energy Environ. Sci.* **2014**, *7*, 399.
- [13] C. S. Ponseca Jr., T. J. Savenije, M. Abdellah, K. Zheng, A. Yartsev, T. Pascher, T. Harlang, P. Chabera, T. Pullerits, A. Stepanov, J.-P. Wolf, V. Sundström, *J. Am. Chem. Soc.* **2014**, *136*, 5189.
- [14] K.-G. Lim, S. Ahn, Y.-H. Kim, Y. Qi, T.-W. Lee, *Energy Environ. Sci.* **2016**, *9*, 932.
- [15] Q. Dong, Y. Fang, Y. Shao, P. Mulligan, J. Qiu, L. Cao, J. Huang, *Science* **2015**, *347*, 967.
- [16] D. Shi, V. Adinolfi, R. Comin, M. J. Yuan, E. Alarousu, A. Buin, Y. Chen, S. Hoogland, A. Rothenberger, K. Katsiev, Y. Losovyj, X. Zhang, P. A. Dowben, O. F. Mohammed, E. H. Sargent, O. M. Bakr, *Science* **2015**, *347*, 519.
- [17] S. D. Stranks, G. E. Eperon, G. Grancini, C. Menelaou, M. J. P. Alcocer, T. Leijtens, L. M. Herz, A. Petrozza, H. J. Snaith, *Science* **2013**, *342*, 341.
- [18] G. Xing, N. Mathews, S. Sun, S. S. Lim, Y. M. Lam, M. Grätzel, S. Mhaisalkar, T. C. Sum, *Science* **2013**, *342*, 344.
- [19] V. D'Innocenzo, G. Grancini, M. J. P. Alcocer, A. R. S. Kandada, S. D. Stranks, M. M. Lee, G. Lanzani, H. J. Snaith, A. Petrozza, *Nat. Commun.* **2014**, *5*, 3586.
- [20] J.-H. Im, C.-R. Lee, J.-W. Lee, S.-W. Park, N.-G. Park, *Nanoscale* **2011**, *3*, 4088.
- [21] H.-S. Kim, C.-R. Lee, J.-H. Im, K.-B. Lee, T. Moehl, A. Marchioro, S.-J. Moon, R. Humphry-Baker, J.-H. Yum, J. E. Moser, M. Grätzel, N.-G. Park, *Sci. Rep.* **2012**, *2*, 591.
- [22] J. Burschka, N. Pellet, S.-J. Moon, R. Humphry-Baker, P. Gao, M. K. Nazeeruddin, M. Grätzel, *Nature* **2013**, *499*, 316.
- [23] M. Liu, M. B. Johnston, H. J. Snaith, *Nature* **2013**, *501*, 395.
- [24] N. J. Jeon, J. H. Noh, Y. C. Kim, W. S. Yang, S. Ryu, S. I. Seok, *Nat. Mater.* **2014**, *13*, 897.
- [25] N. J. Jeon, J. H. Noh, W. S. Yang, Y. C. Kim, S. Ryu, J. Seo, S. I. Seok, *Nature* **2015**, *517*, 476.
- [26] E. H. Anaraki, A. Kermanpur, L. Steier, K. Domanski, T. Matsui, W. Tress, M. Saliba, A. Abate, M. Grätzel, A. Hagfeldt, J.-P. Correa-Baena, *Energy Environ. Sci.* **2016**, *9*, 3128.
- [27] J.-Y. Seo, T. Matsui, J. S. Luo, J.-P. Correa-Baena, F. Giordano, M. Saliba, K. Schenk, A. Ummadisingu, K. Domanski, M. Hadadian, A. Hagfeldt, S. M. Zakeeruddin, U. Steiner, M. Grätzel, A. Abate, *Adv. Energy Mater.* **2016**, *6*, 1600767.
- [28] D. Yang, X. Zhou, R. Yang, Z. Yang, W. Yu, X. Wang, C. Li, S. Liu, R. P. H. Chang, *Energy Environ. Sci.* **2016**, *9*, 3071.
- [29] Z. Zhu, Y. Bai, X. Liu, C.-C. Chueh, S. Yang, A.-K. Jen, *Adv. Mater.* **2016**, *28*, 6478.
- [30] W. S. Yang, B.-W. Park, E. H. Jung, N. J. Jeon, Y. C. Kim, D. U. Lee, S. S. Shin, J. Seo, E. K. Kim, J. H. Noh, S. I. Seok, *Science* **2017**, *356*, 1376.
- [31] Y. Bai, X. Meng, S. Yang, *Adv. Energy Mater.* **2018**, *8*, 1701883.
- [32] Z. Li, T. R. Klein, D. H. Kim, M. J. Yang, J. J. Berry, M. F. A. M. van Hest, K. Zhu, *Nat. Rev. Mater.* **2018**, *3*, 18017.
- [33] J. Seo, S. Park, Y. C. Kim, N. J. Jeon, J. H. Noh, S. C. Yoon, S. I. Sang, *Energy Environ. Sci.* **2014**, *7*, 2642.
- [34] J. H. Heo, H. J. Han, D. Kim, T. K. Ahn, S. H. Im, *Energy Environ. Sci.* **2015**, *8*, 1602.
- [35] A. B. Djurišić, F. Z. Liu, H. W. Tam, M. K. Wong, A. Ng, C. Surya, W. Chen, Z. B. He, *Prog. Quantum Electron.* **2017**, *53*, 1.
- [36] P. Cheng, X. Zhan, *Chem. Soc. Rev.* **2016**, *45*, 2544.
- [37] M. M. Lee, J. Teuscher, T. Miyasaka, T. N. Murakami, H. J. Snaith, *Science* **2012**, *338*, 643.
- [38] J.-Y. Jeng, Y.-F. Chiang, M.-H. Lee, S.-R. Peng, T.-F. Guo, P. Chen, T.-C. Wen, *Adv. Mater.* **2013**, *25*, 3727.
- [39] C.-H. Chiang, M. K. Nazeeruddin, M. Grätzel, C.-G. Wu, *Energy Environ. Sci.* **2017**, *10*, 808.
- [40] Z. Ku, Y. Rong, M. Xu, T. Liu, H. Han, *Sci. Rep.* **2013**, *3*, 3132.
- [41] A. Mei, X. Li, L. Liu, Z. Ku, T. Liu, Y. Rong, M. Xu, M. Hu, J. Chen, Y. Yang, M. Grätzel, H. Han, *Science* **2014**, *345*, 295.
- [42] Y. Hu, Z. Zhang, A. Mei, Y. Jiang, X. Hou, Q. Wang, K. Du, Y. Rong, Y. Zhou, G. Xu, H. Han, *Adv. Mater.* **2018**, *30*, 1705786.
- [43] H. Chen, S. Yang, *Adv. Mater.* **2017**, *29*, 1603994.
- [44] S. Maniarasu, T. B. Korukonda, V. Manjunath, E. Ramasamy, M. Ramesh, G. Veerappan, *Renewable Sustainable Energy Rev.* **2018**, *82*, 845.
- [45] A. Fakharuddin, R. Jose, T. M. Brown, F. Fabregat-Santiago, J. Bisquert, *Energy Environ. Sci.* **2014**, *7*, 3952.
- [46] Y. Zhang, Y. Liu, Z. Yang, S. Liu, *J. Energy Chem.* **2018**, *27*, 722.
- [47] T. J. Savenije, C. S. Ponseca Jr., L. Kunneman, M. Abdellah, K. Zheng, Y. Tian, Q. Zhu, S. E. Canton, I. G. Scheblykin, T. Pullerits, A. Yartsev, V. Sundström, *J. Phys. Chem. Lett.* **2014**, *5*, 2189.
- [48] J.-H. Im, H.-S. Kim, N.-G. Park, *APL Mater.* **2014**, *2*, 081510.
- [49] Q. Chen, H. Zhou, Z. Hong, S. Luo, H.-S. Duan, H.-H. Wang, Y. Liu, G. Li, Y. Yang, *J. Am. Chem. Soc.* **2014**, *136*, 622.
- [50] J.-W. Lee, H.-S. Kim, N.-G. Park, *Acc. Chem. Res.* **2016**, *49*, 311.
- [51] W. Chen, Y. Wu, Y. Yue, J. Liu, W. Zhang, X. Yang, H. Chen, E. Bi, I. Ashraf, M. Grätzel, L. Han, *Science* **2015**, *350*, 944.
- [52] M. Yang, Y. Zhou, Y. Zeng, C.-S. Jiang, N. P. Padture, K. Zhu, *Adv. Mater.* **2015**, *27*, 6363.
- [53] M. R. Leyden, Y. Jiang, Y. Qi, *J. Mater. Chem. A* **2016**, *4*, 13125.
- [54] J. Lee, J. Kim, C.-L. Lee, G. Kim, T. K. Kim, H. Back, S. Jung, K. Yu, S. Hong, S. Lee, S. Kim, S. Jeong, H. Kang, K. Lee, *Adv. Energy Mater.* **2017**, *7*, 1700226.
- [55] Y. Wu, F. Xie, H. Chen, X. Yang, H. Su, M. Cai, Z. Zhou, T. Noda, L. Han, *Adv. Mater.* **2017**, *29*, 1701073.
- [56] Y. Deng, E. Peng, Y. Shao, Z. Xiao, Q. Dong, J. Huang, *Energy Environ. Sci.* **2015**, *8*, 1544.
- [57] Y. Deng, X. Zheng, Y. Bai, Q. Wang, J. Zhao, J. Huang, *Nat. Energy* **2018**, *3*, 560.
- [58] F. Ye, H. Chen, F. Xie, W. Tang, M. Yin, J. He, E. Bi, Y. Wang, X. Yang, L. Han, *Energy Environ. Sci.* **2016**, *9*, 2295.
- [59] H. Chen, F. Ye, W. Tang, J. He, M. Yin, Y. Wang, F. Xie, E. Bi, X. Yang, M. Grätzel, L. Han, *Nature* **2017**, *550*, 92.
- [60] M. A. Green, K. Emery, Y. Hishikawa, W. Warta, E. D. Dunlop, D. H. Levi, A. W. Y. Ho-Baillie, *Prog. Photovoltaics* **2017**, *25*, 3.
- [61] F. Matteocci, L. Cinà, F. Di Giacomo, S. Razza, A. L. Palma, A. Guidobaldi, A. D'Epifanio, S. Licocchia, T. M. Brown, A. Reale, A. Di Carlo, *Prog. Photovoltaics* **2016**, *24*, 436.
- [62] H. Chen, Z. Wei, H. He, X. Zheng, K. Wong, S. Yang, *Adv. Energy Mater.* **2016**, *6*, 1502087.
- [63] D. Vak, K. Hwang, A. Faulks, Y.-S. Jung, N. Clark, D.-Y. Kim, G. J. Wilson, S. E. Watkins, *Adv. Energy Mater.* **2015**, *5*, 1401539.
- [64] K. Hwang, Y.-S. Jung, Y.-J. Heo, F. H. Scholes, S. E. Watkins, J. Subbiah, D. J. Jones, D.-Y. Kim, D. Vak, *Adv. Mater.* **2015**, *27*, 1241.
- [65] S. Razza, F. Di Giacomo, F. Matteocci, L. Cinà, A. L. Palma, S. Casaluci, P. Cameron, A. D'Epifanio, S. Licocchia, A. Reale, T. M. Brown, A. Di Carlo, *J. Power Sources* **2015**, *277*, 286.

- [66] Q. Guo, C. Li, W. Qiao, S. Ma, F. Wang, B. Zhang, L. Hu, S. Dai, Z. Tan, *Energy Environ. Sci.* **2016**, 9, 1486.
- [67] X. Chen, H. Cao, H. Yu, H. Zhu, H. Zhou, L. Yang, S. Yin, *J. Mater. Chem. A* **2016**, 4, 9124.
- [68] H. Huang, J. Shi, L. Zhu, D. Li, Y. Luo, Q. Meng, *Nano Energy* **2016**, 27, 352.
- [69] F. Ye, W. Tang, F. Xie, M. Yin, J. He, Y. Wang, H. Chen, Y. Qiang, X. Yang, L. Han, *Adv. Mater.* **2017**, 29, 1701440.
- [70] A. Agresti, S. Pescetelli, A. L. Palma, A. E. Del Rio Castillo, D. Konios, G. Kakavelakis, S. Razza, L. Cinà, E. Kymakis, F. Bonaccorso, A. Di Carlo, *ACS Energy Lett.* **2017**, 2, 279.
- [71] J. H. Heo, D. H. Song, S. H. Im, *Adv. Mater.* **2014**, 26, 8179.
- [72] G. Fu, L. Hou, Y. Wang, X. Liu, J. Wang, H. Li, Y. Cui, D. Liu, X. Li, S. Yang, *Solar Energy Mater. Solar Cells* **2017**, 165, 36.
- [73] J. Chen, Y. Rong, A. Mei, Y. Xiong, T. Liu, Y. Sheng, P. Jiang, L. Hong, Y. Guan, X. Zhu, X. Hou, M. Duan, J. Zhao, X. Li, H. Han, *Adv. Energy Mater.* **2016**, 6, 1502009.
- [74] H. Dong, Z. Wu, J. Xi, X. Xu, L. Zuo, T. Lei, X. Zhao, L. Zhang, X. Hou, A. K.-Y. Jen, *Adv. Funct. Mater.* **2018**, 28, 1704836.
- [75] E. Mosconi, A. Amat, M. K. Nazeeruddin, M. Grätzel, F. De Angelis, *J. Phys. Chem. C* **2013**, 117, 13902.
- [76] L. Etgar, P. Gao, Z. Xue, Q. Peng, A. K. Chandiran, B. Liu, M. K. Nazeeruddin, M. Grätzel, *J. Am. Chem. Soc.* **2012**, 134, 17396.
- [77] J. You, Z. Hong, Y. Yang, Q. Chen, M. Cai, T.-B. Song, C.-C. Chen, S. Lu, Y. Liu, H. Zhou, Y. Yang, *ACS Nano* **2014**, 8, 1674.
- [78] J. H. Noh, S. H. Im, J. H. Heo, T. N. Mandal, S. I. Seok, *Nano Lett.* **2013**, 13, 1764.
- [79] S. Ryu, J. H. Noh, N. J. Jeon, Y. C. Kim, W. S. Yang, J. Seo, S. I. Seok, *Energy Environ. Sci.* **2014**, 7, 2614.
- [80] F. Matteocci, S. Razza, F. Di Giacomo, S. Casaluci, G. Mincuzzi, T. M. Brown, A. D'Epifanio, S. Licocchia, A. Di Carlo, *Phys. Chem. Chem. Phys.* **2014**, 16, 3918.
- [81] A. Fakhruddin, F. Di Giacomo, A. L. Palma, F. Matteocci, I. Ahmed, S. Razza, A. D'Epifanio, S. Licocchia, J. Ismail, A. Di Carlo, T. M. Brown, R. Jose, *ACS Nano* **2015**, 9, 8420.
- [82] W. Qiu, T. Merckx, M. Jaysankar, C. M. de la Huerta, L. Rakocevic, W. Zhang, U. W. Paetzold, R. Gehlhaar, L. Froyen, J. Poortmans, D. Cheyns, H. J. Snaith, P. Heremans, *Energy Environ. Sci.* **2016**, 9, 484.
- [83] M. Yang, Z. Li, M. O. Reese, O. G. Reid, D. H. Kim, S. Siol, T. R. Klein, Y. Yan, J. J. Berry, M. F. A. M. van Hest, K. Zhu, *Nat. Energy* **2017**, 2, 17038.
- [84] F. Di Giacomo, V. Zardetto, A. D'Epifanio, S. Pescetelli, F. Matteocci, S. Razza, A. Di Carlo, S. Licocchia, W. M. M. Kessels, M. Creatore, T. M. Brown, *Adv. Energy Mater.* **2015**, 5, 1401808.
- [85] Z. Yang, C.-C. Chueh, F. Zuo, J. H. Kim, P.-W. Liang, A. K.-Y. Jen, *Adv. Energy Mater.* **2015**, 5, 1500328.
- [86] T. M. Schmidt, T. T. Larsen-Olsen, J. E. Carlé, D. Angmo, F. C. Krebs, *Adv. Energy Mater.* **2015**, 5, 1500569.
- [87] H. Back, J. Kim, G. Kim, T. K. Kim, H. Kang, J. Kong, S. H. Lee, K. Lee, *Solar Energy Mater. Solar Cells* **2016**, 144, 309.
- [88] J. G. Tait, S. Manghooli, W. Qiu, L. Rakocevic, L. Kootstra, M. Jaysankar, C. A. M. de la Huerta, U. W. Paetzold, R. Gehlhaar, D. Cheyns, P. Heremans, J. Poortmans, *J. Mater. Chem. A* **2016**, 4, 3792.
- [89] W. Nie, H. Tsai, R. Asadpour, J.-C. Blancon, A. J. Neukirch, G. Gupta, J. J. Crochet, M. Chhowalla, S. Tretiak, M. A. Alam, H.-L. Wang, A. D. Mohite, *Science* **2015**, 347, 522.
- [90] C.-H. Chiang, J.-W. Lin, C.-G. Wu, *J. Mater. Chem. A* **2016**, 4, 13525.
- [91] C. C. Stoumpos, C. D. Malliakas, M. G. Kanatzidis, *Inorg. Chem.* **2013**, 52, 9019.
- [92] B. Conings, J. Drijkoningen, N. Gauquelin, A. Babayigit, J. D'Haen, L. D'Olieslaeger, A. Ethirajan, J. Verbeeck, J. Manca, E. Mosconi, F. De Angelis, H.-G. Boyen, *Adv. Energy Mater.* **2015**, 5, 1500477.
- [93] R. K. Misra, S. Aharon, B. Li, D. Mogilyansky, I. Visoly-Fisher, L. Etgar, E. A. Katz, *J. Phys. Chem. Lett.* **2015**, 6, 326.
- [94] E. T. Hoke, D. J. Slotcavage, E. R. Dohner, A. R. Bowring, H. I. Karunadasa, M. D. McGehee, *Chem. Sci.* **2015**, 6, 613.
- [95] A. Binek, F. C. Hanusch, P. Docampo, T. Bein, *J. Phys. Chem. Lett.* **2015**, 6, 1249.
- [96] G. E. Eperon, S. D. Stranks, C. Menelaou, M. B. Johnston, L. M. Herz, H. J. Snaith, *Energy Environ. Sci.* **2014**, 7, 982.
- [97] M. R. Leyden, M. V. Lee, S. R. Raga, Y. Qi, *J. Mater. Chem. A* **2015**, 3, 16097.
- [98] J. Borchert, R. L. Milot, J. B. Patel, C. L. Davies, A. D. Wright, L. M. Maestro, H. J. Snaith, L. M. Herz, M. B. Johnston, *ACS Energy Lett.* **2017**, 2, 2799.
- [99] C.-Y. Chang, W.-K. Huang, Y.-C. Chang, K.-T. Lee, C.-T. Chen, *J. Mater. Chem. A* **2016**, 4, 640.
- [100] C.-Y. Chang, B.-C. Tsai, Y.-C. Hsiao, Y.-C. Huang, C.-S. Tsao, *Phys. Chem. Chem. Phys.* **2016**, 18, 31836.
- [101] J.-W. Lee, D.-J. Seol, A.-N. Cho, N.-G. Park, *Adv. Mater.* **2014**, 26, 4991.
- [102] X. Li, D. Bi, C. Yi, J.-D. Decoppet, J. Luo, S. M. Zakeeruddin, A. Hagfeldt, M. Grätzel, *Science* **2016**, 353, 58.
- [103] Y. Wu, X. Yang, W. Chen, Y. Yue, M. Cai, F. Xie, E. Bi, A. Islam, L. Han, *Nat. Energy* **2016**, 1, 16148.
- [104] M. Xiao, F. Huang, W. Huang, Y. Dkhissi, Y. Zhu, J. Etheridge, A. Gray-Weale, U. Bach, Y.-B. Cheng, L. Spiccia, *Angew. Chem., Int. Ed.* **2014**, 53, 9898.
- [105] S. Mostafa Nowee, A. Abbas, J. A. Romagnoli, *Chem. Eng. Sci.* **2008**, 63, 5457.
- [106] Z. Xiao, Q. Dong, C. Bi, Y. Shao, Y. Yuan, J. Huang, *Adv. Mater.* **2014**, 26, 6503.
- [107] Y. Yu, S. Yang, L. Lei, Q. Cao, J. Shao, S. Zhang, Y. Liu, *ACS Appl. Mater. Interfaces* **2017**, 9, 3667.
- [108] J. Kim, J. S. Yun, Y. Cho, D. S. Lee, B. Wilkinson, A. M. Soufiani, X. Deng, J. Zheng, A. Shi, S. Lim, S. Chen, Z. Hameiri, M. Zhang, C. F. J. Lau, S. Huang, M. A. Green, A. W. Y. Ho-Baillie, *ACS Energy Lett.* **2017**, 2, 1978.
- [109] N. Pellet, P. Gao, G. Gregori, T.-Y. Yang, M. K. Nazeeruddin, J. Maier, M. Grätzel, *Angew. Chem., Int. Ed.* **2014**, 53, 3151.
- [110] H. Tan, A. Jain, O. Voznyy, X. Lan, F. P. García de Arquer, J. Z. Fan, R. Quintero-Bermudez, M. Yuan, B. Zhang, Y. Zhao, F. Fan, P. Li, L. N. Quan, Y. Zhao, Z.-H. Lu, Z. Yang, S. Hoogland, E. H. Sargent, *Science* **2017**, 355, 722.
- [111] J. Lu, X. Lin, X. Jiao, T. Gengenbach, A. D. Scully, L. Jiang, B. Tan, J. Sun, B. Li, N. K. Pai, U. Bach, A. N. Simonov, Y.-B. Cheng, *Energy Environ. Sci.* **2018**, 11, 1880.
- [112] W. Qiu, A. Ray, M. Jaysankar, T. Merckx, J. P. Bastos, D. Cheyns, R. Gehlhaar, J. Poortmans, P. Heremans, *Adv. Funct. Mater.* **2017**, 27, 1700920.
- [113] J. Huang, P. Xu, J. Liu, X.-Z. You, *Small* **2017**, 13, 1603225.
- [114] Y. Jiang, M. R. Leyden, L. Qiu, S. Wang, L. K. Ono, Z. Wu, E. J. Juarez-Perez, Y. Qi, *Adv. Funct. Mater.* **2018**, 28, 1703835.
- [115] T. Bu, X. Liu, Y. Zhou, J. Yi, X. Huang, L. Luo, J. Xiao, Z. Ku, Y. Peng, F. Huang, Y.-B. Cheng, J. Zhong, *Energy Environ. Sci.* **2017**, 10, 2509.
- [116] P. Docampo, T. Bein, *Acc. Chem. Res.* **2016**, 49, 339.
- [117] R. Yang, L. Zhang, Y. Cao, Y. Miao, Y. Ke, Y. Wei, Q. Guo, Y. Wang, Z. Rong, N. Wang, R. Li, J. Wang, W. Huang, F. Gao, *Appl. Phys. Lett.* **2017**, 111, 073302.
- [118] R. Li, C. Yi, R. Ge, W. Zou, L. Cheng, N. Wang, J. Wang, W. Huang, *Appl. Phys. Lett.* **2016**, 109, 151101.
- [119] A. Yangui, D. Garrot, J. S. Lauret, A. Lusson, G. Bouchez, E. Deleporte, S. Pillet, E. E. Bendeif, M. Castro, S. Triki, Y. Abid, K. Boukheddaden, *J. Phys. Chem. C* **2015**, 119, 23638.
- [120] Y. Wei, M. Li, R. Li, L. Zhang, R. Yang, W. Zou, Y. Cao, M. Xu, C. Yi, N. Wang, J. Wang, W. Huang, *Appl. Phys. Lett.* **2018**, 113, 041103.



- [121] I. C. Smith, E. T. Hoke, D. Solis-Ibarra, M. D. McGehee, H. I. Karunadasa, *Angew. Chem., Int. Ed.* **2014**, *53*, 11232.
- [122] D. H. Cao, C. C. Stoumpos, O. K. Farha, J. T. Hupp, M. G. Kanatzidis, *J. Am. Chem. Soc.* **2015**, *137*, 7843.
- [123] H. Tsai, W. Nie, J.-C. Blancon, C. C. Stoumpos, R. Asadpour, B. Harutyunyan, A. J. Neukirch, R. Verduzco, J. J. Crochet, S. Tretiak, L. Pedesseau, J. Even, M. A. Alam, G. Gupta, J. Lou, P. M. Ajayan, M. J. Bedzyk, M. G. Kanatzidis, A. D. Mohite, *Nature* **2016**, *536*, 312.
- [124] L. N. Quan, M. Yuan, R. Comin, O. Voznyy, E. M. Beauregard, S. Hoogland, A. Buin, A. R. Kirmani, K. Zhao, A. Amassian, D. H. Kim, E. H. Sargent, *J. Am. Chem. Soc.* **2016**, *138*, 2649.
- [125] X. Li, M. I. Dar, C. Yi, J. Luo, M. Tschumi, S. M. Zakeeruddin, M. K. Nazeeruddin, H. Han, M. Grätzel, *Nat. Chem.* **2015**, *7*, 703.
- [126] A. Priyadarshi, L. J. Haur, P. Murray, D. Fu, S. Kulkarni, G. Xing, T. C. Sum, N. Mathews, S. G. Mhaisalkar, *Energy Environ. Sci.* **2016**, *9*, 3687.
- [127] Y. Hu, S. Si, A. Mei, Y. Rong, H. Liu, X. Li, H. Han, *Sol. RRL* **2017**, *1*, 1600019.
- [128] G. Grancini, C. Roldán-Carmona, I. Zimmermann, E. Mosconi, X. Lee, D. Martineau, S. Narbey, F. Oswald, F. De Angelis, M. Graetzel, M. K. Nazeeruddin, *Nat. Commun.* **2017**, *8*, 15684.
- [129] J. Lu, L. Jiang, W. Li, F. Li, N. K. Pai, A. D. Scully, C.-M. Tsai, U. Bach, A. N. Simonov, Y.-B. Cheng, L. Spiccia, *Adv. Energy Mater.* **2017**, *7*, 1700444.
- [130] K. Yao, X. Wang, Y.-X. Xu, F. Li, L. Zhou, *Chem. Mater.* **2016**, *28*, 3131.
- [131] N. K. Elumalai, A. Uddin, *Energy Environ. Sci.* **2016**, *9*, 391.
- [132] S. Chen, Y. Hou, H. Chen, M. Richter, F. Guo, S. Kahmann, X. Tang, T. Stubhan, H. Zhang, N. Li, N. Gasparini, C. O. R. Quiroz, L. S. Khanzada, G. J. Matt, A. Osvet, C. J. Brabec, *Adv. Energy Mater.* **2016**, *6*, 1600132.
- [133] Y. Shao, Y. Yuan, J. Huang, *Nat. Energy* **2016**, *1*, 15001.
- [134] L. Zhu, J. Xiao, J. Shi, J. Wang, S. Lv, Y. Xu, Y. Luo, Y. Xiao, S. Wang, Q. Meng, X. Li, D. Li, *Nano Res.* **2015**, *8*, 1116.
- [135] U. Bach, D. Lupo, P. Comte, J. E. Moser, F. Weissortel, J. Salbeck, H. Spreitzer, M. Grätzel, *Nature* **1998**, *395*, 583.
- [136] D. Bi, G. Boschloo, A. Hagfeldt, *Nano* **2014**, *09*, 1440001.
- [137] B. Xu, J. Zhang, Y. Hua, P. Liu, L. Wang, C. Ruan, Y. Li, G. Boschloo, E. M. J. Johansson, L. Kloo, A. Hagfeldt, A. K.-Y. Jen, L. Sun, *Chem* **2017**, *2*, 676.
- [138] J. Zhang, B. Xu, L. Yang, C. Ruan, L. Wang, P. Liu, W. Zhang, N. Vlachopoulos, L. Kloo, G. Boschloo, L. Sun, A. Hagfeldt, E. M. J. Johansson, *Adv. Energy Mater.* **2018**, *8*, 1701209.
- [139] F. Zhang, Z. Wang, H. Zhu, N. Pellet, J. Luo, C. Yi, X. Liu, H. Liu, S. Wang, X. Li, Y. Xiao, S. M. Zakeeruddin, D. Bi, M. Grätzel, *Nano Energy* **2017**, *41*, 469.
- [140] A. Molina-Ontoria, I. Zimmermann, I. Garcia-Benito, P. Gratia, C. Roldán-Carmona, S. Aghazada, M. Graetzel, M. K. Nazeeruddin, N. Martín, *Angew. Chem., Int. Ed.* **2016**, *55*, 6270.
- [141] I. Garcia-Benito, I. Zimmermann, J. Urieta-Mora, J. Aragón, A. Molina-Ontoria, E. Ortí, N. Martín, M. K. Nazeeruddin, *J. Mater. Chem. A* **2017**, *5*, 8317.
- [142] I. Zimmermann, J. Urieta-Mora, P. Gratia, J. Aragón, G. Grancini, A. Molina-Ontoria, E. Ortí, N. Martín, M. K. Nazeeruddin, *Adv. Energy Mater.* **2017**, *7*, 1601674.
- [143] K. Rakstys, A. Abate, M. I. Dar, P. Gao, V. Jankauskas, G. Jacopin, E. Kamarauskas, S. Kazim, S. Ahmad, M. Grätzel, M. K. Nazeeruddin, *J. Am. Chem. Soc.* **2015**, *137*, 16172.
- [144] C. Huang, W. Fu, C.-Z. Li, Z. Zhang, W. Qiu, M. Shi, P. Heremans, A. K.-Y. Jen, H. Chen, *J. Am. Chem. Soc.* **2016**, *138*, 2528.
- [145] K. Rakstys, S. Paek, P. Gao, P. Gratia, T. Marszalek, G. Grancini, K. T. Cho, K. Genevicius, V. Jankauskas, W. Pisula, M. K. Nazeeruddin, *J. Mater. Chem. A* **2017**, *5*, 7811.
- [146] Y. Wang, Z. Zhu, C.-C. Chueh, A. K.-Y. Jen, Y. Chi, *Adv. Energy Mater.* **2017**, *7*, 1700823.
- [147] F. Wu, Y. Shan, J. Qiao, C. Zhong, R. Wang, Q. Song, L. Zhu, *ChemSusChem* **2017**, *10*, 3833.
- [148] I. Cho, N. J. Jeon, O. K. Kwon, D. W. Kim, E. H. Jung, J. H. Noh, J. Seo, S. I. Seok, S. Y. Park, *Chem. Sci.* **2017**, *8*, 734.
- [149] S. Park, J. H. Heo, J. H. Yun, T. S. Jung, K. Kwak, M. J. Ko, C. H. Cheon, J. Y. Kim, S. H. Im, H. J. Son, *Chem. Sci.* **2016**, *7*, 5517.
- [150] D. Bi, B. Xu, P. Gao, L. Sun, M. Grätzel, A. Hagfeldt, *Nano Energy* **2016**, *23*, 138.
- [151] B. Xu, D. Bi, Y. Hua, P. Liu, M. Cheng, M. Grätzel, L. Kloo, A. Hagfeldt, L. Sun, *Energy Environ. Sci.* **2016**, *9*, 873.
- [152] B. Xu, Z. Zhu, J. Zhang, H. Liu, C.-C. Chueh, X. Li, A. K.-Y. Jen, *Adv. Energy Mater.* **2017**, *7*, 1700683.
- [153] K. Rakstys, M. Saliba, P. Gao, P. Gratia, E. Kamarauskas, S. Paek, V. Jankauskas, M. K. Nazeeruddin, *Angew. Chem., Int. Ed.* **2016**, *55*, 7464.
- [154] T. Qin, W. Huang, J.-E. Kim, D. Vak, C. Forsyth, C. R. McNeill, Y.-B. Cheng, *Nano Energy* **2017**, *31*, 210.
- [155] K. Rakstys, S. Paek, G. Grancini, P. Gao, V. Jankauskas, A. M. Asiri, M. K. Nazeeruddin, *ChemSusChem* **2017**, *10*, 3825.
- [156] J. Zhang, Y. Hua, B. Xu, L. Yang, P. Liu, M. B. Johansson, N. Vlachopoulos, L. Kloo, G. Boschloo, E. M. J. Johansson, L. Sun, A. Hagfeldt, *Adv. Energy Mater.* **2016**, *6*, 1601062.
- [157] N. J. Jeon, H. Na, E. H. Jung, T.-Y. Yang, Y. G. Lee, G. Kim, H.-W. Shin, S. Il Seok, J. Lee, J. Seo, *Nat. Energy* **2018**, *3*, 682.
- [158] A.-N. Cho, N. Chakravarthi, K. Kranthiraja, S. S. Reddy, H.-S. Kim, S.-H. Jin, N.-G. Park, *J. Mater. Chem. A* **2017**, *5*, 7603.
- [159] R. Grisorio, B. Roose, S. Colella, A. Listorti, G. P. Suranna, A. Abate, *ACS Energy Lett.* **2017**, *2*, 1029.
- [160] K. Rakstys, S. Paek, M. Sohail, P. Gao, K. T. Cho, P. Gratia, Y. Lee, K. H. Dahmen, M. K. Nazeeruddin, *J. Mater. Chem. A* **2016**, *4*, 18259.
- [161] H. D. Pham, Z. Wu, L. K. Ono, S. Manzhos, K. Feron, N. Motta, Y. Qi, P. Sonar, *Adv. Electron. Mater.* **2017**, *3*, 1700139.
- [162] Y. Hua, J. B. Zhang, B. Xu, P. Liu, M. Cheng, L. Kloo, E. M. J. Johansson, K. Sveinbjörnsson, K. Aitola, G. Boschloo, L. C. Sun, *Nano Energy* **2016**, *26*, 108.
- [163] R. Tiazkis, S. Paek, M. Daskeviciene, T. Malinauskas, M. Saliba, J. Nekrasovas, V. Jankauskas, S. Ahmad, V. Getautis, M. Khaja Nazeeruddin, *Sci. Rep.* **2017**, *7*, 150.
- [164] T. Malinauskas, M. Saliba, T. Matsui, M. Daskeviciene, S. Urnikaite, P. Gratia, R. Send, H. Wonneberger, I. Bruder, M. Graetzel, V. Getautis, M. K. Nazeeruddin, *Energy Environ. Sci.* **2016**, *9*, 1681.
- [165] P. Gratia, A. Magomedov, T. Malinauskas, M. Daskeviciene, A. Abate, S. Ahmad, M. Grätzel, V. Getautis, M. K. Nazeeruddin, *Angew. Chem., Int. Ed.* **2015**, *54*, 11409.
- [166] M. Daskeviciene, S. Paek, Z. P. Wang, T. Malinauskas, G. Jokubauskaite, K. Rakstys, K. T. Cho, A. Magomedov, V. Jankauskas, S. Ahmad, H. J. Snaith, V. Getautis, M. K. Nazeeruddin, *Nano Energy* **2017**, *32*, 551.
- [167] X. Li, M. Cai, Z. Zhou, K. Yun, F. Xie, Z. Lan, J. Hua, L. Han, *J. Mater. Chem. A* **2017**, *5*, 10480.
- [168] C. Y. Lu, I. T. Choi, J. Kim, H. K. Kim, *J. Mater. Chem. A* **2017**, *5*, 20263.
- [169] E. Gabriëlsson, H. Ellis, S. Feldt, H. N. Tian, G. Boschloo, A. Hagfeldt, L. C. Sun, *Adv. Energy Mater.* **2013**, *3*, 1647.
- [170] M. S. Kang, S. D. Sung, I. T. Choi, H. Kim, M. Hong, J. Kim, W. I. Lee, H. K. Kim, *ACS Appl. Mater. Interfaces* **2015**, *7*, 22213.
- [171] T. Leijtens, T. Giovenzana, S. N. Habisreutinger, J. S. Tinkham, N. K. Noel, B. A. Kamino, G. Sadoughi, A. Sellinger, H. J. Snaith, *ACS Appl. Mater. Interfaces* **2016**, *8*, 5981.

- [172] S. D. Sung, M. S. Kang, I. T. Choi, H. M. Kim, H. Kim, M. Hong, H. K. Kim, W. I. Lee, *Chem. Commun.* **2014**, 50, 14161.
- [173] H. Wang, A. D. Sheikh, Q. Feng, F. Li, Y. Chen, W. Yu, E. Alarousu, C. Ma, M. A. Haque, D. Shi, Z.-S. Wang, O. F. Mohammed, O. M. Bakr, T. Wu, *ACS Photonics* **2015**, 2, 849.
- [174] J. Wang, Y. Chen, F. Li, X. Zong, J. Guo, Z. Sun, S. Xue, *Electrochim. Acta* **2016**, 210, 673.
- [175] B. Xu, E. Sheibani, P. Liu, J. Zhang, H. Tian, N. Vlachopoulos, G. Boschloo, L. Kloo, A. Hagfeldt, L. Sun, *Adv. Mater.* **2014**, 26, 6629.
- [176] M.-D. Zhang, B.-H. Zheng, Q.-F. Zhuang, C.-Y. Huang, H. Cao, M.-D. Chen, B. Wang, *Dyes Pigm.* **2017**, 146, 589.
- [177] L. Zhu, Y. Shan, R. Wang, D. Liu, C. Zhong, Q. Song, F. Wu, *Chem. – Eur. J.* **2017**, 23, 4373.
- [178] J.-M. Kim, S.-J. Yoo, C.-K. Moon, B. Sim, J.-H. Lee, H. Lim, J. W. Kim, J.-J. Kim, *J. Phys. Chem. C* **2016**, 120, 9475.
- [179] I. Salzmann, G. Heimel, M. Oehzelt, S. Winkler, N. Koch, *Acc. Chem. Res.* **2016**, 49, 370.
- [180] M. A. Mahmud, N. K. Elumalai, M. B. Upama, D. Wang, V. R. Goncales, M. Wright, C. Xu, F. Haque, A. Uddin, *Phys. Chem. Chem. Phys.* **2017**, 19, 21033.
- [181] Y. Liu, Z. Hong, Q. Chen, H. Chen, W.-H. Chang, Y. M. Yang, T.-B. Song, Y. Yang, *Adv. Mater.* **2016**, 28, 440.
- [182] J. H. Heo, S. Park, S. H. Im, H. J. Son, *ACS Appl. Mater. Interfaces* **2017**, 9, 39511.
- [183] Z. Li, Z. Zhu, C.-C. Chueh, S. B. Jo, J. Luo, S.-H. Jang, A. K.-Y. Jen, *J. Am. Chem. Soc.* **2016**, 138, 11833.
- [184] X. Sun, Q. Xue, Z. Zhu, Q. Xiao, K. Jiang, H.-L. Yip, H. Yan, Z. Li, *Chem. Sci.* **2018**, 9, 2698.
- [185] S. Paek, P. Qin, Y. Lee, K. T. Cho, P. Gao, G. Grancini, E. Oveisi, P. Gratia, K. Rakstys, S. A. Al-Muhtaseb, C. Ludwig, J. Ko, M. K. Nazeeruddin, *Adv. Mater.* **2017**, 29, 1606555.
- [186] J. Zhang, L. J. Xu, P. Huang, Y. Zhou, Y. Y. Zhu, N. Y. Yuan, J. N. Ding, Z. G. Zhang, Y. F. Li, *J. Mater. Chem. C* **2017**, 5, 12752.
- [187] S. J. Park, S. Jeon, I. K. Lee, J. Zhang, H. Jeong, J.-Y. Park, J. Bang, T. K. Ahn, H.-W. Shin, B.-G. Kim, H. J. Park, *J. Mater. Chem. A* **2017**, 5, 13220.
- [188] X. Liu, X. Zheng, Y. Wang, Z. Chen, F. Yao, Q. Zhang, G. Fang, Z.-K. Chen, W. Huang, Z.-X. Xu, *ChemSusChem* **2017**, 10, 2833.
- [189] R. Azmi, S. Y. Nam, S. Sinaga, Z. A. Akbar, C.-L. Lee, S. C. Yoon, I. H. Jung, S.-Y. Jang, *Nano Energy* **2018**, 44, 191.
- [190] F. Zhang, X. Liu, C. Yi, D. Bi, J. Luo, S. Wang, X. Li, Y. Xiao, S. M. Zakeeruddin, M. Grätzel, *ChemSusChem* **2016**, 9, 2578.
- [191] F. Zhang, C. Yi, P. Wei, X. Bi, J. Luo, G. Jacopin, S. Wang, X. Li, Y. Xiao, S. M. Zakeeruddin, M. Grätzel, *Adv. Energy Mater.* **2016**, 6, 1600401.
- [192] Y. Xue, Y. Wu, Y. Li, *J. Power Sources* **2017**, 344, 160.
- [193] H. Chen, W. Fu, C. Huang, Z. Zhang, S. Li, F. Ding, M. Shi, C.-Z. Li, A. K.-Y. Jen, H. Chen, *Adv. Energy Mater.* **2017**, 7, 1700012.
- [194] C. Yin, J. Lu, Y. Xu, Y. Yun, K. Wang, J. Li, L. Jiang, J. Sun, A. D. Scully, F. Huang, J. Zhong, J. Wang, Y.-B. Cheng, T. Qin, W. Huang, *Adv. Energy Mater.* **2018**, 1800538.
- [195] J. H. Heo, S. H. Im, J. H. Noh, T. N. Mandal, C.-S. Lim, J. A. Chang, Y. H. Lee, H.-J. Kim, A. Sarkar, M. K. Nazeeruddin, M. Grätzel, S. I. Seok, *Nat. Photonics* **2013**, 7, 486.
- [196] T.-W. Lee, O. Kwon, M.-G. Kim, S. H. Park, J. Chung, S. Y. Kim, Y. Chung, J.-Y. Park, E. Han, D. H. Huh, J.-J. Park, L. Pu, *Appl. Phys. Lett.* **2005**, 87, 231106.
- [197] X. Hu, Z. Huang, X. Zhou, P. Li, Y. Wang, Z. Huang, M. Su, W. Ren, F. Li, M. Li, Y. Chen, Y. Song, *Adv. Mater.* **2017**, 29, 1703236.
- [198] M. T. Dang, L. Hirsch, G. Wantz, *Adv. Mater.* **2011**, 23, 3597.
- [199] H. Sirringhaus, N. Tessler, R. H. Friend, *Science* **1998**, 280, 1741.
- [200] Y. Guo, C. Liu, K. Inoue, K. Harano, H. Tanaka, E. Nakamura, *J. Mater. Chem. A* **2014**, 2, 13827.
- [201] M. Park, J.-S. Park, I. K. Han, J. Y. Oh, *J. Mater. Chem. A* **2016**, 4, 11307.
- [202] N. Y. Nia, F. Matteocci, L. Cina, A. Di Carlo, *ChemSusChem* **2017**, 10, 3854.
- [203] A. Dubey, N. Adhikari, S. Venkatesan, S. Gu, D. Khatiwada, Q. Wang, L. Mohammad, M. Kumar, Q. Qiao, *Solar Energy Mater. Solar Cells* **2016**, 145, 193.
- [204] E. A. Gaml, A. Dubey, K. M. Reza, M. N. Hasan, N. Adhikari, H. Elbohy, B. Bahrami, H. Zeyada, S. Yang, Q. Qiao, *Solar Energy Mater. Solar Cells* **2017**, 168, 8.
- [205] P. Qin, N. Tetreault, M. I. Dar, P. Gao, K. L. McCall, S. R. Rutter, S. D. Ogier, N. D. Forrest, J. S. Bissett, M. J. Simms, A. J. Page, R. Fisher, M. Grätzel, M. K. Nazeeruddin, *Adv. Energy Mater.* **2015**, 5, 1400980.
- [206] M. Wong-Stringer, J. E. Bishop, J. A. Smith, D. K. Mohamad, A. J. Parnell, V. Kumar, C. Rodenburg, D. G. Lidzey, *J. Mater. Chem. A* **2017**, 5, 15714.
- [207] Z. Yu, Y. Zhang, X. Jiang, X. Li, J. Lai, M. Hu, M. Elawad, G. G. Gurzadyan, X. Yang, L. Sun, *RSC Adv.* **2017**, 7, 27189.
- [208] B. Conings, L. Baeten, C. De Dobbelaere, J. D'Haen, J. Manca, H.-G. Boyen, *Adv. Mater.* **2014**, 26, 2041.
- [209] J. Kim, G. Kim, T. K. Kim, S. Kwon, H. Back, J. Lee, S. H. Lee, H. Kang, K. Lee, *J. Mater. Chem. A* **2014**, 2, 17291.
- [210] H.-C. Liao, T. L. D. Tam, P. Guo, Y. Wu, E. F. Manley, W. Huang, N. Zhou, C. M. M. Soe, B. Wang, M. R. Wasielewski, L. X. Chen, M. G. Kanatzidis, A. Facchetti, R. P. H. Chang, T. J. Marks, *Adv. Energy Mater.* **2016**, 6, 1600502.
- [211] J. Liu, Q. Ge, W. Zhang, J. Ma, J. Ding, G. Yu, J. Hu, *Nano Res.* **2018**, 11, 185.
- [212] W. Yan, Y. Li, Y. Li, S. Ye, Z. Liu, S. Wang, Z. Bian, C. Huang, *Nano Energy* **2015**, 16, 428.
- [213] Z. Zhou, Y. Zhao, C. Zhang, D. Zou, Y. Chen, Z. Lin, H. Zhen, Q. Ling, *J. Mater. Chem. A* **2017**, 5, 6613.
- [214] B. Cai, Y. Xing, Z. Yang, W.-H. Zhang, J. Qiu, *Energy Environ. Sci.* **2013**, 6, 1480.
- [215] W. Chen, X. Bao, Q. Zhu, D. Zhu, M. Qiu, M. Sun, R. Yang, *J. Mater. Chem. C* **2015**, 3, 10070.
- [216] J. M. Marin-Beloqui, J. P. Hernández, E. Palomares, *Chem. Commun.* **2014**, 50, 14566.
- [217] P. Nagarjuna, K. Narayanaswamy, T. Swetha, G. H. Rao, S. P. Singh, G. D. Sharma, *Electrochim. Acta* **2015**, 151, 21.
- [218] Y. Xiao, G. Han, Y. Chang, H. Zhou, M. Li, Y. Li, *J. Power Sources* **2014**, 267, 1.
- [219] Z. Zhu, Y. Bai, H. K. H. Lee, C. Mu, T. Zhang, L. Zhang, J. Wang, H. Yan, S. K. So, S. Yang, *Adv. Funct. Mater.* **2014**, 24, 7357.
- [220] Y. S. Kwon, J. Lim, H.-J. Yun, Y.-H. Kim, T. Park, *Energy Environ. Sci.* **2014**, 7, 1454.
- [221] G.-W. Kim, G. Kang, J. Kim, G.-Y. Lee, H. I. Kim, L. Pyeon, J. Lee, T. Park, *Energy Environ. Sci.* **2016**, 9, 2326.
- [222] J. Lee, M. Malekshahi Byranvand, G. Kang, S. Y. Son, S. Song, G.-W. Kim, T. Park, *J. Am. Chem. Soc.* **2017**, 139, 12175.
- [223] G.-W. Kim, J. Lee, G. Kang, T. Kim, T. Park, *Adv. Energy Mater.* **2018**, 8, 1701935.
- [224] F. Cai, J. Cai, L. Yang, W. Li, R. S. Gurney, H. Yi, A. Iraqi, D. Liu, T. Wang, *Nano Energy* **2018**, 45, 28.
- [225] Y. Hou, X. Du, S. Scheiner, D. P. McMeekin, Z. Wang, N. Li, M. S. Killian, H. Chen, M. Richter, I. Levchuk, N. Schrenker, E. Spiecker, T. Stubhan, N. A. Luechinger, A. Hirsch, P. Schmuki, H.-P. Steinrück, R. H. Fink, M. Halik, H. J. Snaith, C. J. Brabec, *Science* **2017**, 358, 1192.
- [226] A. Guerrero, A. Bou, G. Matt, O. Almora, T. Heumüller, G. Garcia-Belmonte, J. Bisquert, Y. Hou, C. Brabec, *Adv. Energy Mater.* **2018**, 8, 1703376.
- [227] Y. Xu, T. Bu, M. Li, T. Qin, C. Yin, N. Wang, R. Li, J. Zhong, H. Li, Y. Peng, J. Wang, L. Xie, W. Huang, *ChemSusChem* **2017**, 10, 2578.
- [228] P.-L. Qin, G. Yang, Z.-W. Ren, S. H. Cheung, S. K. So, L. Chen, J. Hao, J. Hou, G. Li, *Adv. Mater.* **2018**, 30, 1706126.

- [229] J. Jiang, Q. Wang, Z. Jin, X. Zhang, J. Lei, H. Bin, Z.-G. Zhang, Y. Li, S. Liu, *Adv. Energy Mater.* **2018**, *8*, 1701757.
- [230] J. Lee, H. Kang, G. Kim, H. Back, J. Kim, S. Hong, B. Park, E. Lee, K. Lee, *Adv. Mater.* **2017**, *29*, 1606363.
- [231] A. R. Murphy, J. M. J. Fréchet, *Chem. Rev.* **2007**, *107*, 1066.
- [232] J. Zaumseil, H. Sirringhaus, *Chem. Rev.* **2007**, *107*, 1296.
- [233] C. V. Kumar, G. Sfyrri, D. Raptis, E. Stathatos, P. Lianos, *RSC Adv.* **2015**, *5*, 3786.
- [234] F. Zhang, X. Yang, M. Cheng, W. Wang, L. Sun, *Nano Energy* **2016**, *20*, 108.
- [235] Y. C. Kim, T.-Y. Yang, N. J. Jeon, J. Im, S. Jang, T. J. Shin, H.-W. Shin, S. Kim, E. Lee, S. Kim, J. H. Noh, S. I. Seok, J. Seo, *Energy Environ. Sci.* **2017**, *10*, 2109.
- [236] K. T. Cho, O. Trukhina, C. Roldán-Carmona, M. Ince, P. Gratia, G. Grancini, P. Gao, T. Marszalek, W. Pisula, P. Y. Reddy, T. Torres, M. K. Nazeeruddin, *Adv. Energy Mater.* **2017**, *7*, 1601733.
- [237] M. Cheng, Y. Li, M. Safdari, C. Chen, P. Liu, L. Kloo, L. Sun, *Adv. Energy Mater.* **2017**, *7*, 1602556.
- [238] Z. H. Bakr, Q. Wali, A. Fakharuddin, L. Schmidt-Mende, T. M. Brown, R. Jose, *Nano Energy* **2017**, *34*, 271.
- [239] P. Vivo, J. K. Salunke, A. Priimagi, *Materials* **2017**, *10*, 1087.
- [240] W. Chen, Y. Wu, J. Liu, C. Qin, X. Yang, A. Islam, Y.-B. Cheng, L. Han, *Energy Environ. Sci.* **2015**, *8*, 629.
- [241] J. H. Park, J. Seo, S. Park, S. S. Shin, Y. C. Kim, N. J. Jeon, H.-W. Shin, T. K. Ahn, J. H. Noh, S. C. Yoon, C. S. Hwang, S. I. Seok, *Adv. Mater.* **2015**, *27*, 4013.
- [242] K.-C. Wang, J.-Y. Jeng, P.-S. Shen, Y.-C. Chang, E. W.-G. Diau, C.-H. Tsai, T.-Y. Chao, H.-C. Hsu, P.-Y. Lin, P. Chen, T.-F. Guo, T.-C. Wen, *Sci. Rep.* **2015**, *4*, 4756.
- [243] K.-C. Wang, P.-S. Shen, M.-H. Li, S. Chen, M.-W. Lin, P. Chen, T.-F. Guo, *ACS Appl. Mater. Interfaces* **2014**, *6*, 11851.
- [244] J. Cui, F. Meng, H. Zhang, K. Cao, H. Yuan, Y. Cheng, F. Huang, M. Wang, *ACS Appl. Mater. Interfaces* **2014**, *6*, 22862.
- [245] X. Yin, P. Chen, M. Que, Y. Xing, W. Que, C. Niu, J. Shao, *ACS Nano* **2016**, *10*, 3630.
- [246] J. H. Kim, P.-W. Liang, S. T. Williams, N. Cho, C.-C. Chueh, M. S. Glaz, D. S. Ginger, A. K.-Y. Jen, *Adv. Mater.* **2015**, *27*, 695.
- [247] Z. Zhu, Y. Bai, T. Zhang, Z. Liu, X. Long, Z. Wei, Z. Wang, L. Zhang, J. Wang, F. Yan, S. Yang, *Angew. Chem., Int. Ed.* **2014**, *53*, 12571.
- [248] J. You, L. Meng, T.-B. Song, T.-F. Guo, Y. M. Yang, W.-H. Chang, Z. Hong, H. Chen, H. Zhou, Q. Chen, Y. Liu, N. De Marco, Y. Yang, *Nat. Nanotechnol.* **2016**, *11*, 75.
- [249] J. W. Jung, C.-C. Chueh, A. K.-Y. Jen, *Adv. Mater.* **2015**, *27*, 7874.
- [250] J.-Y. Jeng, K.-C. Chen, T.-Y. Chiang, P.-Y. Lin, T.-D. Tsai, Y.-C. Chang, T.-F. Guo, P. Chen, T.-C. Wen, Y.-J. Hsu, *Adv. Mater.* **2014**, *26*, 4107.
- [251] H. Zhang, J. Cheng, F. Lin, H. He, J. Mao, K. S. Wong, A. K.-Y. Jen, W. C. H. Choy, *ACS Nano* **2016**, *10*, 1503.
- [252] F. Jiang, W. C. H. Choy, X. Li, D. Zhang, J. Cheng, *Adv. Mater.* **2015**, *27*, 2930.
- [253] L. Hu, J. Peng, W. Wang, Z. Xia, J. Yuan, J. Lu, X. Huang, W. Ma, H. Song, W. Chen, Y.-B. Cheng, J. Tang, *ACS Photonics* **2014**, *1*, 547.
- [254] S. Seo, I. J. Park, M. Kim, S. Lee, C. Bae, H. S. Jung, N.-G. Park, J. Y. Kim, H. Shin, *Nanoscale* **2016**, *8*, 11403.
- [255] K. Cao, Z. Zuo, J. Cui, Y. Shen, T. Moehl, S. M. Zakeeruddin, M. Grätzel, M. Wang, *Nano Energy* **2015**, *17*, 171.
- [256] X. Xu, Z. Liu, Z. Zuo, M. Zhang, Z. Zhao, Y. Shen, H. Zhou, Q. Chen, Y. Yang, M. Wang, *Nano Lett.* **2015**, *15*, 2402.
- [257] Z. Liu, M. Zhang, X. Xu, F. Cai, H. Yuan, L. Bu, W. Li, A. Zhu, Z. Zhao, M. Wang, Y.-B. Cheng, H. He, *J. Mater. Chem. A* **2015**, *3*, 24121.
- [258] Z. Liu, M. Zhang, X. Xu, L. Bu, W. Zhang, W. Li, Z. Zhao, M. Wang, Y.-B. Cheng, H. He, *Dalton Trans.* **2015**, *44*, 3967.
- [259] P. Pattanasattayavong, G. O. N. Ndjawa, K. Zhao, K. W. Chou, N. Yaacobi-Gross, B. C. O'Regan, A. Amassian, T. D. Anthopoulos, *Chem. Commun.* **2013**, *49*, 4154.
- [260] B. O'Regan, D. T. Schwartz, S. M. Zakeeruddin, M. Grätzel, *Adv. Mater.* **2000**, *12*, 1263.
- [261] P. Pattanasattayavong, N. Yaacobi-Gross, K. Zhao, G. O. Ndjawa, J. Li, F. Yan, B. C. O'Regan, A. Amassian, T. D. Anthopoulos, *Adv. Mater.* **2013**, *25*, 1504.
- [262] K. Tsujimoto, D. C. Nguyen, S. Ito, H. Nishino, H. Matsuyoshi, A. Konno, G. R. A. Kumara, K. Tennakone, *J. Phys. Chem. C* **2012**, *116*, 13465.
- [263] P. Qin, S. Tanaka, S. Ito, N. Tetreault, K. Manabe, H. Nishino, M. K. Nazeeruddin, M. Grätzel, *Nat. Commun.* **2014**, *5*, 3834.
- [264] V. E. Madhavan, I. Zimmermann, C. Roldán-Carmona, G. Grancini, M. Buffiere, A. Belaidi, M. K. Nazeeruddin, *ACS Energy Lett.* **2016**, *1*, 1112.
- [265] M. Jung, Y. C. Kim, N. J. Jeon, W. S. Yang, J. Seo, J. H. Noh, S. Il Seok, *ChemSusChem* **2016**, *9*, 2592.
- [266] N. Arora, M. I. Dar, A. Hinderhofer, N. Pellet, F. Schreiber, S. M. Zakeeruddin, M. Grätzel, *Science* **2017**, *358*, 768.
- [267] S. Gharibzadeh, B. A. Nejand, A. Moshaii, N. Mohammadian, A. H. Alizadeh, R. Mohammadpour, V. Ahmadi, A. Alizadeh, *ChemSusChem* **2016**, *9*, 1929.
- [268] A. O. Musa, T. Akomolafe, M. J. Carter, *Solar Energy Mater. Solar Cells* **1998**, *51*, 305.
- [269] J. A. Christians, R. C. Fung, P. V. Kamat, *J. Am. Chem. Soc.* **2014**, *136*, 758.
- [270] W.-Y. Chen, L.-L. Deng, S.-M. Dai, X. Wang, C.-B. Tian, X.-X. Zhan, S.-Y. Xie, R.-B. Huang, L.-S. Zheng, *J. Mater. Chem. A* **2015**, *3*, 19353.
- [271] X. Li, J. Yang, Q. Jiang, W. Chu, D. Zhang, Z. Zhou, J. Xin, *ACS Appl. Mater. Interfaces* **2017**, *9*, 41354.
- [272] P. Nazari, F. Ansari, B. Abdollahi Nejand, V. Ahmadi, M. Payandeh, M. Salavati-Niasari, *J. Phys. Chem. C* **2017**, *121*, 21935.
- [273] C. Zuo, L. Ding, *Small* **2015**, *11*, 5528.
- [274] Y. Guo, H. Lei, L. Xiong, B. Li, Z. Chen, J. Wen, G. Yang, L. Gang, G. Fang, *J. Mater. Chem. A* **2017**, *5*, 11055.
- [275] W. Sun, Y. Li, S. Ye, H. Rao, W. Yan, H. Peng, Y. Li, Z. Liu, S. Wang, Z. Chen, L. Xiao, Z. Bian, C. Huang, *Nanoscale* **2016**, *8*, 10806.
- [276] M.-K. Son, L. Steier, M. Schreier, M. T. Mayer, J. Luo, M. Grätzel, *Energy Environ. Sci.* **2017**, *10*, 912.
- [277] A. Bashir, S. Shukla, J. H. Lew, S. Shukla, A. Bruno, D. Gupta, T. Baikie, R. Patidar, Z. Akhter, A. Priyadarshi, N. Mathews, S. G. Mhaisalkar, *Nanoscale* **2018**, *10*, 2341.
- [278] M. F. M. Noh, C. H. Teh, R. Daik, E. L. Lim, C. C. Yap, M. A. Ibrahim, N. A. Ludin, A. B. Yusoff, J. Jang, M. A. M. Terid, *J. Mater. Chem. C* **2018**, *6*, 6038.
- [279] F. Ansari, P. Nazari, M. Payandeh, F. M. Asl, B. Abdollahi-Nejand, V. Ahmadi, J. Taghilo, M. Salavati-Niasari, *Nanotechnology* **2018**, *29*, 075404.
- [280] D. Yang, R. Yang, J. Zhang, Z. Yang, S. Liu, C. Li, *Energy Environ. Sci.* **2015**, *8*, 3208.
- [281] H. Lu, W. Tian, B. Gu, Y. Zhu, L. Li, *Small* **2017**, *13*, 1701535.
- [282] W. Qiu, U. W. Paetzold, R. Gehlhaar, V. Smirnov, H.-G. Boyen, J. G. Tait, B. Conings, W. Zhang, C. B. Nielsen, I. McCulloch, L. Froyen, P. Heremans, D. Cheyns, *J. Mater. Chem. A* **2015**, *3*, 22824.
- [283] T.-P. Chen, C.-W. Lin, S.-S. Li, Y.-H. Tsai, C.-Y. Wen, W. J. Lin, F.-M. Hsiao, Y.-P. Chiu, K. Tsukagoshi, M. Osada, T. Sasaki, C.-W. Chen, *Adv. Energy Mater.* **2018**, *8*, 1701722.
- [284] M.-C. Kim, B. J. Kim, J. Yoon, J.-W. Lee, D. Suh, N.-G. Park, M. Choi, H. S. Jung, *Nanoscale* **2015**, *7*, 20725.
- [285] H. J. Snaith, R. Humphry-Baker, P. Chen, I. Cesar, S. M. Zakeeruddin, M. Grätzel, *Nanotechnology* **2008**, *19*, 424003.
- [286] T. Leijtens, J. Lim, J. Teuscher, T. Park, H. J. Snaith, *Adv. Mater.* **2013**, *25*, 3227.
- [287] H. Zhou, Q. Chen, G. Li, S. Luo, T.-B. Song, H.-S. Duan, Z. Hong, J. You, Y. Liu, Y. Yang, *Science* **2014**, *345*, 542.



- [288] P. Zhang, J. Wu, T. Zhang, Y. Wang, D. Liu, H. Chen, L. Ji, C. Liu, W. Ahmad, Z. D. Chen, S. Li, *Adv. Mater.* **2018**, *30*, 1703737.
- [289] J. Song, E. Zheng, J. Bian, X.-F. Wang, W. Tian, Y. Sanehira, T. Miyasaka, *J. Mater. Chem. A* **2015**, *3*, 10837.
- [290] K. Mahmood, B. S. Swain, A. R. Kirmani, A. Amassian, *J. Mater. Chem. A* **2015**, *3*, 9051.
- [291] J. Feng, Z. Yang, D. Yang, X. Ren, X. Zhu, Z. Jin, W. Zi, Q. Wei, S. Liu, *Nano Energy* **2017**, *36*, 1.
- [292] A. Bera, K. W. Wu, A. Sheikh, E. Alarousu, O. F. Mohammed, T. Wu, *J. Phys. Chem. C* **2014**, *118*, 28494.
- [293] L. Zhu, Z. Shao, J. Ye, X. Zhang, X. Pan, S. Dai, *Chem. Commun.* **2016**, *52*, 970.
- [294] P. Tiwana, P. Docampo, M. B. Johnston, H. J. Snaith, L. M. Herz, *ACS Nano* **2011**, *5*, 5158.
- [295] Z.-L. Tseng, C.-H. Chiang, S.-H. Chang, C.-G. Wu, *Nano Energy* **2016**, *28*, 311.
- [296] W. Ke, G. Fang, Q. Liu, L. Xiong, P. Qin, H. Tao, J. Wang, H. Lei, B. Li, J. Wan, G. Yang, Y. Yan, *J. Am. Chem. Soc.* **2015**, *137*, 6730.
- [297] E. Castro, J. Murillo, O. Fernandez-Delgado, L. Echegoyen, *J. Mater. Chem. C* **2018**, *6*, 2635.
- [298] P. Docampo, J. M. Ball, M. Darwich, G. E. Eperon, H. J. Snaith, *Nat. Commun.* **2013**, *4*, 2761.
- [299] Y. Shao, Z. Xiao, C. Bi, Y. Yuan, J. Huang, *Nat. Commun.* **2014**, *5*, 5784.
- [300] D.-S. Leem, A. Edwards, M. Faist, J. Nelson, D. D. Bradley, J. C. de Mello, *Adv. Mater.* **2011**, *23*, 4371.
- [301] S. Kim, S. Y. Kim, M. H. Chung, J. Kim, J. H. Kim, *J. Mater. Chem. C* **2015**, *3*, 5859.
- [302] J. S. Yu, I. Kim, J. S. Kim, J. Jo, T. T. Larsen-Olsen, R. R. Sondergaard, M. Hosel, D. Angmo, M. Jorgensen, F. C. Krebs, *Nanoscale* **2012**, *4*, 6032.
- [303] Y.-C. Huang, F.-H. Hsu, H.-C. Cha, C.-M. Chuang, C.-S. Tsao, C.-Y. Chen, *Org. Electron.* **2013**, *14*, 2809.
- [304] M. Hamsch, Q. Lin, A. Armin, P. L. Burn, P. Meredith, *J. Mater. Chem. A* **2016**, *4*, 13830.
- [305] H. Sung, N. Ahn, M. S. Jang, J.-K. Lee, H. Yoon, N.-G. Park, M. Choi, *Adv. Energy Mater.* **2016**, *6*, 1501873.
- [306] J. Yoon, H. Sung, G. Lee, W. Cho, N. Ahn, H. S. Jung, M. Choi, *Energy Environ. Sci.* **2017**, *10*, 337.
- [307] T. Leijtens, G. E. Eperon, S. Pathak, A. Abate, M. M. Lee, H. J. Snaith, *Nat. Commun.* **2013**, *4*, 2885.
- [308] D. Langley, G. Giusti, C. Mayousse, C. Celle, D. Bellet, J. P. Simonato, *Nanotechnology* **2013**, *24*, 452001.
- [309] L. Bu, Z. Liu, M. Zhang, W. Li, A. Zhu, F. Cai, Z. Zhao, Y. Zhou, *ACS Appl. Mater. Interfaces* **2015**, *7*, 17776.
- [310] T.-H. Han, H. Kim, S.-J. Kwon, T.-W. Lee, *Mater. Sci. Eng., R* **2017**, *118*, 1.
- [311] C.-H. Chung, T.-B. Song, B. Bob, R. Zhu, H.-S. Duan, Y. Yang, *Adv. Mater.* **2012**, *24*, 5499.
- [312] L. Hu, H. S. Kim, J.-Y. Lee, P. Peumans, Y. Cui, *ACS Nano* **2010**, *4*, 2955.
- [313] F. Guo, P. Kubis, T. Przybilla, E. Spiecker, A. Hollmann, S. Langner, K. Forberich, C. J. Brabec, *Adv. Energy Mater.* **2015**, *5*, 1401779.
- [314] S. Han, S. Hong, J. Ham, J. Yeo, J. Lee, B. Kang, P. Lee, J. Kwon, S. S. Lee, M.-Y. Yang, S. H. Ko, *Adv. Mater.* **2014**, *26*, 5808.
- [315] J. Kim, W. J. da Silva, A. R. Yusoff, J. Jang, *Sci. Rep.* **2016**, *6*, 19813.
- [316] K. Critchley, B. P. Khanal, M. Ł. Górzny, L. Vigderman, S. D. Evans, E. R. Zubarev, N. A. Kotov, *Adv. Mater.* **2010**, *22*, 2338.
- [317] F. Guo, H. Azimi, Y. Hou, T. Przybilla, M. Hu, C. Bronnbauer, S. Langner, E. Spiecker, K. Forberich, C. J. Brabec, *Nanoscale* **2015**, *7*, 1642.
- [318] M. Lee, Y. Ko, Y. Jun, *J. Mater. Chem. A* **2015**, *3*, 19310.
- [319] K. Yang, F. Li, J. Zhang, C. P. Veeramalai, T. Guo, *Nanotechnology* **2016**, *27*, 095202.
- [320] M. Xie, H. Lu, L. Zhang, J. Wang, Q. Luo, J. Lin, L. Ba, H. Liu, W. Shen, L. Shi, C.-Q. Ma, *Sol. RRL* **2018**, *2*, 1700184.
- [321] D. Bryant, P. Greenwood, J. Troughton, M. Wijdekop, M. Carnie, M. Davies, K. Wojciechowski, H. J. Snaith, T. Watson, D. Worsley, *Adv. Mater.* **2014**, *26*, 7499.
- [322] H. Hwang, A. Kim, Z. Zhong, H.-C. Kwon, S. Jeong, J. Moon, *Adv. Funct. Mater.* **2016**, *26*, 6545.
- [323] J. Zhang, F. Li, K. Yang, C. P. Veeramalai, T. Guo, *Appl. Surf. Sci.* **2016**, *369*, 308.
- [324] G. E. Eperon, D. Bryant, J. Troughton, S. D. Stranks, M. B. Johnston, T. Watson, D. A. Worsley, H. J. Snaith, *J. Phys. Chem. Lett.* **2015**, *6*, 129.
- [325] G. D. Spyropoulos, C. O. R. Quiroz, M. Salvador, Y. Hou, N. Gasparini, P. Schweizer, J. Adams, P. Kubis, N. Li, E. Spiecker, T. Ameri, H.-J. Egelhaaf, C. J. Brabec, *Energy Environ. Sci.* **2016**, *9*, 2302.
- [326] J. Ahn, H. Hwang, S. Jeong, J. Moon, *Adv. Energy Mater.* **2017**, *7*, 1602751.
- [327] L. Zhang, T. Liu, L. Liu, M. Hu, Y. Yang, A. Mei, H. Han, *J. Mater. Chem. A* **2015**, *3*, 9165.
- [328] J. Zhang, Z. Meng, D. Guo, H. Zou, J. Yu, K. Fan, *Appl. Surf. Sci.* **2018**, *430*, 531.
- [329] Z. Wei, X. Zheng, H. Chen, X. Long, Z. Wang, S. Yang, *J. Mater. Chem. A* **2015**, *3*, 16430.
- [330] Z. Yu, B. Chen, P. Liu, C. Wang, C. Bu, N. Cheng, S. Bai, Y. Yan, X. Zhao, *Adv. Funct. Mater.* **2016**, *26*, 4866.
- [331] H. Zhou, Y. Shi, Q. Dong, H. Zhang, Y. Xing, K. Wang, Y. Du, T. Ma, *J. Phys. Chem. Lett.* **2014**, *5*, 3241.
- [332] F. Zhang, X. Yang, H. Wang, M. Cheng, J. Zhao, L. Sun, *ACS Appl. Mater. Interfaces* **2014**, *6*, 16140.
- [333] Z. Li, P. P. Boix, G. Xing, K. Fu, S. A. Kulkarni, S. K. Batabyal, W. Xu, A. Cao, T. C. Sum, N. Mathews, L. H. Wong, *Nanoscale* **2016**, *8*, 6352.
- [334] X. Wang, Z. Li, W. Xu, S. A. Kulkarni, S. K. Batabyal, S. Zhang, A. Cao, L. H. Wong, *Nano Energy* **2015**, *11*, 728.
- [335] Z. Wei, H. Chen, K. Yan, X. Zheng, S. Yang, *J. Mater. Chem. A* **2015**, *3*, 24226.
- [336] Z. Li, S. A. Kulkarni, P. P. Boix, E. Shi, A. Cao, K. Fu, S. K. Batabyal, J. Zhang, Q. Xiong, L. H. Wong, N. Mathews, S. G. Mhaisalkar, *ACS Nano* **2014**, *8*, 6797.
- [337] J. Ryu, K. Lee, J. Yun, H. Yu, J. Lee, J. Jang, *Small* **2017**, *13*, 1701225.
- [338] Q. Luo, H. Ma, F. Hao, Q. Hou, J. Ren, L. Wu, Z. Yao, Y. Zhou, N. Wang, K. Jiang, H. Lin, Z. Guo, *Adv. Funct. Mater.* **2017**, *27*, 1703068.
- [339] M. Duan, Y. Rong, A. Mei, Y. Hu, Y. Sheng, Y. Guan, H. Han, *Carbon* **2017**, *120*, 71.
- [340] P. You, Z. Liu, Q. Tai, S. Liu, F. Yan, *Adv. Mater.* **2015**, *27*, 3632.
- [341] J. M. Frost, K. T. Butler, F. Brivio, C. H. Hendon, M. van Schilfgarde, A. Walsh, *Nano Lett.* **2014**, *14*, 2584.
- [342] K. Domanski, J.-P. Correa-Baena, N. Mine, M. K. Nazeeruddin, A. Abate, M. Saliba, W. Tress, A. Hagfeldt, M. Grätzel, *ACS Nano* **2016**, *10*, 6306.
- [343] C. Li, A. Guerrero, Y. Zhong, A. Gräser, C. A. M. Luna, J. Köhler, J. Bisquert, R. Hildner, S. Huettner, *Small* **2017**, *13*, 1701711.
- [344] A. Guerrero, J. You, C. Aranda, Y. S. Kang, G. Garcia-Belmonte, H. Zhou, J. Bisquert, Y. Yang, *ACS Nano* **2016**, *10*, 218.
- [345] J. Carrillo, A. Guerrero, S. Rahimnejad, O. Almora, I. Zarazua, E. Mas-Marza, J. Bisquert, G. Garcia-Belmonte, *Adv. Energy Mater.* **2016**, *6*, 1502246.
- [346] J.-P. Correa-Baena, S.-H. Turren-Cruz, W. Tress, A. Hagfeldt, C. Aranda, L. Shoostari, J. Bisquert, A. Guerrero, *ACS Energy Lett.* **2017**, *2*, 681.